

Assessment of different health monitoring techniques for damage characterization in a spar cap- shear web thick adhesive joint of a wind turbine blade

Khoshmanesh, S.

DOI

[10.4233/uuid:596eb25a-cf4f-4885-837f-ded6c1957f13](https://doi.org/10.4233/uuid:596eb25a-cf4f-4885-837f-ded6c1957f13)

Publication date

2024

Document Version

Final published version

Citation (APA)

Khoshmanesh, S. (2024). *Assessment of different health monitoring techniques for damage characterization in a spar cap- shear web thick adhesive joint of a wind turbine blade*. [Dissertation (TU Delft), Delft University of Technology]. <https://doi.org/10.4233/uuid:596eb25a-cf4f-4885-837f-ded6c1957f13>

Important note

To cite this publication, please use the final published version (if applicable).
Please check the document version above.

Copyright

Other than for strictly personal use, it is not permitted to download, forward or distribute the text or part of it, without the consent of the author(s) and/or copyright holder(s), unless the work is under an open content license such as Creative Commons.

Takedown policy

Please contact us and provide details if you believe this document breaches copyrights.
We will remove access to the work immediately and investigate your claim.

**Assessment of different health monitoring
techniques for damage characterization in a
spar cap- shear web thick adhesive joint of a
wind turbine blade**

Assessment of different health monitoring techniques for damage characterization in a spar cap- shear web thick adhesive joint of a wind turbine blade

Proefschrift

ter verkrijging van de graad van doctor
aan de Technische Universiteit Delft,
op gezag van de Rector Magnificus Prof. Dr. ir. T.H.J.J. van der Hagen,
voorzitter van het College voor Promoties,
in het openbaar te verdedigen op dinsdag 16 april 2024 om 15:00 uur

door

Seyedsharif KHOSHMANESH

Master of Science in Mechanical Engineering,
Sharif University of Technology, Tehran, Iran,
geboren te Khormoj Iran.

Dit proefschrift is goedgekeurd door de

Promotor: Prof. Dr. S.J. Watson

Promotor: Dr. D. Zarouchas

Samenstelling promotiecommissie:

Rector Magnificus, voorzitter

Prof. Dr. S.J. Watson, Technische Universiteit Delft, Promotor

Dr. D. Zarouchas, Technische Universiteit Delft, Promotor

Onafhankelijke leden:

Prof. Dr. ir. J.W. van Wingerden

Technische Universiteit Delft, Nederland

Dr. J.J.E. Teuwen, Technische Universiteit Delft, Nederland

Prof. Dr. A.R. Nejad Norwegian University of Science and Technology, Norway

Prof. Dr. A. Kolios Danmarks Tekniske Universitet, Denmark

Keywords: Acoustic emission, Vibration analysis, Infrared thermography,
Adhesive joint

Printed by: IPSKAMP

Front & Back: The cover illustrates an offshore wind turbine equipped with sensors on its blades to transmit health monitoring data. Co-designed with Katarina Naskovski.

Copyright © 2024 by S. Khoshmanesh

ISBN 978-94-6384-565-6

An electronic version of this dissertation is available at

<https://repository.tudelft.nl/>.

CONTENTS

Acknowledgements	ix
Summary	xi
Samenvatting	xiii
1 Introduction	1
1.1 Health monitoring, a brief historical overview	2
1.2 Application of structural health monitoring to a Wind turbine	2
1.3 Motivation and purpose of the thesis	6
1.3.1 Problem description	6
1.3.2 Research questions	7
1.3.3 Objectives	7
1.4 Thesis structure	8
2 Application of different sensors for SHM of a wind turbine blade	11
2.1 Introduction	12
2.1.1 Chapter overview	12
2.2 A vibration-based SHM system for a wind turbine blade	12
2.2.1 Conventional vibration sensors	13
2.2.2 MEMS vibration sensors	16
2.2.3 Fiber optic sensors	18
2.3 Acoustic-based SHM of a wind turbine blade	21
2.3.1 Conventional AE sensors	22
2.3.2 Acoustic MEMS sensors	22
2.3.3 Fused tapered coupler sensors	23
2.3.4 Fiber Bragg grating sensor	23
2.3.5 Interferometry based sensors	24
2.3.6 Back scattering based sensors	26
2.4 The potential for a thermographic SHM system for a wind turbine blade	28
2.4.1 Thermographic analysis using an infrared camera	29
2.4.2 Thermographic analysis using fiber optic sensors	30
3 Vibration analysis	31
3.1 Introduction	32
3.1.1 Measurements	32
3.1.2 Modal analysis	32
3.1.3 Damage identification methods	33
3.1.4 Chapter overview	34

3.2	Literature review	35
3.2.1	Historical overview	35
3.2.2	Identification and localization of damage by damping	36
3.3	Wind turbine blade structure	38
3.4	Test specimen	40
3.4.1	Test specimen properties	40
3.5	Part A: Damage propagation and identification	41
3.5.1	Methodology	41
3.5.2	Experimental set up	43
3.5.3	Results and discussion	44
3.6	Part B: damage localization	49
3.6.1	Finite element viscous-elastic damping model	49
3.6.2	Damage modelling of a spar cap-shear web thick adhesive joint	52
3.6.3	Damage identification and localization	54
3.6.4	Calculation of complex eigenvalues and eigenvectors	57
3.6.5	Results	60
3.6.6	Discussion	69
3.6.7	Conclusion	70
4	Acoustic analysis	73
4.1	Introduction	74
4.2	Literature review	76
4.2.1	Historical overview	76
4.2.2	Acoustic emission in a composite materials	78
4.3	Methodology	81
4.4	Experimental set up	82
4.4.1	Test specimen	82
4.4.2	Impact cases	83
4.4.3	Acoustic measurement	85
4.5	Results and discussion	86
4.5.1	Fatigue damage accumulation process based on high-resolution photos	86
4.5.2	Early detection of impact damage	89
4.5.3	Monitoring of the fatigue damage accumulation process by using the spatial distribution of AE events	92
4.6	Conclusion	102
5	Infrared thermography analysis	103
5.1	Introduction	104
5.1.1	Chapter overview	105
5.2	Literature review	105
5.2.1	Historical overview	105
5.2.2	Infrared Thermography analysis applied to composite materials	109
5.3	Methodology	111
5.4	Experimental set up	113

5.5	Results and Discussion	114
5.5.1	No impact	115
5.5.2	Low level of energy impact	120
5.5.3	Medium level of energy impact	124
5.5.4	High level of energy impact	128
5.6	Conclusion	132
6	Conclusion	133
6.1	Main thesis findings	134
6.1.1	Damage propagation	134
6.1.2	Damage characterization	135
6.2	Outlook and future research	137
6.2.1	Estimation of damping in an operational wind turbine blade	137
6.2.2	Quantification of damage using acoustic emission data	138
6.2.3	Recommendation	138
6.3	Final remarks	138
	Curriculum Vitæ	159
	Education	159
	List of Publications	161

ACKNOWLEDGEMENTS

PhD is a long and challenging journey with a lot of highs and lows. Sometimes you struggle for weeks or even months to find a solution for your research questions. It can be incredibly stressful. You shouldn't forget that the challenge is only one aspect of the journey. Any achievement that makes you happy motivates you and makes the journey enjoyable! Moreover, it's important to recognize that you're not alone in this journey. You're part of a collaborative and supportive environment, surrounded by individuals who are eager to assist and support you.

I would like to take this opportunity to acknowledge the individuals who supported me throughout this journey. Without their assistance, completing my Ph.D. would have been significantly more challenging.

Firstly I should express gratitude and thank Prof. Simon.J. Watson who was my promotor and supervisor throughout my PhD period. He consistently made time to discuss my research and to find a way to overcome the challenges. Without his advice and support, completing this journey would have been exceedingly difficult. Additionally, He helped me tremendously with my writing, and his contribution to improving my writing skills was undeniable. I am also indebted to my co-promotor, Dr. Dimitrios Zarouchas, for his technical advice and innovative ideas. His guidance played a crucial role in paving the way for my research success. Without his support and technical advice, traversing this path would have been exceedingly difficult. I would like to extend my gratitude to Dr. Michiel Zayer, who supported and guided me in the early stages of my Ph.D. and was always open to providing valuable consultancy whenever needed. I would like to thank Sylvia our secretary who was always supportive and trustworthy. She always had the right answer to your question.

I am thankful to my Ph.D. colleagues including Chihoon, Delphine, Ashim, Tom, Yanan, Livia, Bedasa, Ming, Sebastian, Danial, and others who I may forget their names for building a friendly atmosphere. Still, when I flash back to that time I miss the wonderful times we had together. Chihoon was the first person in the office with whom I formed a close friendship. We had a lot in common and we spent a lot of time together from having dinner to making Kimchi! Chihoon became like family to me, and I will always cherish the memories we created together. Delphine with her exceptional personality and intellect was always ready to support me. She supported me from debugging my Matlab code to solving my general problems. Without the help of Delphine my PhD life in the Netherlands was not easy. Thank you Delphine for all your support! Yanan, with a smile on his face and a positive attitude, was always supportive and helpful. Livia was very friendly and always ready to help. I would like also to thank my friends Camila, Michiel, and Oswin whom I met during my Ph.D. and then became close friends. We had

a great time together and I never forget the time we spent together especially having dinner on the weekend and playing basketball!.

Finally, I am deeply grateful to my family for their support and encouragement throughout this journey. I am grateful to my son, Shahriar, who stood by me throughout every moment of this journey. His presence brought me comfort and was a source of motivation. Without his company, I couldn't have completed my Ph.D. I would like to express my gratitude to my wife for being with me during the initial years of my Ph.D. Although she couldn't accompany me throughout the entire journey, we shared many good memories together. I would also like to extend my thanks to my sisters, my mother, and my father, who provided unwavering support and encouragement during the most challenging times of my Ph.D. journey. Without their support, navigating this journey would have been exceedingly difficult.

SUMMARY

Developing an effective blade structural health monitoring (SHM) system is important for the wind energy industry. This has challenged the scientific communities for years, and still, the problem has not been solved. This research aims to find a solution to this problem and provide a basis for further research in this field.

The failure rate and the downtime associated with wind turbine blades are relatively high. Within the framework of preventive maintenance, it is necessary to inspect wind turbine blades periodically. Blade inspection needs special tools, skilled manpower, vessels, and lifting equipment; therefore, it is costly. This is the main reason that the wind energy industry would like to minimize the number of periodic blade inspections by using a reliable SHM system.

An issue that complicates the SHM of wind turbine blades is the complexity of blade geometry. Different parts of a wind turbine blade are connected using adhesive. These adhesive joints, e.g., leading edge, trailing edge, and spar cap-shear web adhesive joints, are important parts of the blade structure and play an essential role in the integrity of the blade. These joints are very vulnerable to fatigue damage.

Manufacturing flaws and impact can instigate and accelerate fatigue damage in a wind turbine blade. Impacts may happen during the transportation or installation of the blades, especially for offshore wind turbines. In this study, vibration, acoustic, and infrared thermography are used to characterize fatigue damage in test specimens representative of the spar cap-shear web adhesive joint of a wind turbine blade.

To create different levels of damage, the test specimens were subjected to fatigue tension tests. To study the effect of impact on damage propagation, the test specimens were subjected to different levels of impact using a Gas Canon machine before being subjected to fatigue tests. During the fatigue tests, a Polytech laser vibrometer, Vallen acoustic system, and FLIR infrared thermographic system were used for vibration, acoustic and thermographic analysis.

Damage propagation

Understanding fatigue damage propagation in a spar cap-shear web adhesive joint is the first step in characterizing the damage. Transverse cracks initiated in the adhesive part of the test specimens are the main driving mechanism for the propagation of damage. In the test specimens subjected to medium and high levels of energy impact, they are initiated in the impact zone. In the test specimens subjected to a low level of energy impact, they can initiate in the impact zone, but it is not always the case. After initiation of transverse cracks, they increase in

length transversely and longitudinally, and de-bond the adhesive from the laminate. In the non-impact test specimens, transverse cracks and de-bonding of adhesive from laminate are the dominant types of damage. In the test specimens subjected to impact, in addition to transverse cracks and de-bonding of adhesive from laminate, delamination of laminate plies are also a major source of damage. Delamination occurs in the impact zone and grows during the fatigue tests.

Vibration and thermography analysis

The change in material damping properties was used to characterize damage by using vibration and infrared thermographic analysis. Using vibration analysis, damping is estimated from a visco-elastic model of damping in a composite material. In the case of the thermographic analysis, damping is calculated using a heat transfer model of the test specimens subject to the fatigue tests. The damping calculated by infrared thermographic analysis is more consistent with visible damage propagation observed in the test specimens. Damping increases when the first sign of transverse cracks appears in the test specimens. In the non-impact test specimens, after initiation of transverse cracks, damping increases at a constant rate until the specimens are saturated with transverse cracks. After this phase, the rate of increase in damping declines and tends to flatten off. In the test specimens subjected to medium and high levels of energy impact, damping does not flatten off after the transverse crack saturation phase. This is due to delamination in the impact zone, which keeps growing after the saturation phase.

Acoustic analysis

Acoustic analysis was used to monitor damage propagation in the test specimens subjected to impact. The effect of different levels of energy impact on the propagation of fatigue damage was studied. The rate of acoustic emission (AE) events and the spatial density of AE events were used to monitor damage propagation. For the test specimens exposed to the lowest energy impact, the fatigue damage accumulation process was not really influenced by the size and location of the impact damage. For test specimens exposed to medium and high energy impacts, the fatigue damage accumulation process was clearly influenced by the size and location of the impact damage.

SAMENVATTING

Het ontwikkelen van een effectief systeem voor structurele gezondheidscontrole (SGC) van een windturbinewiek is belangrijk voor de windenergie-industrie. Dit is al jaren een uitdaging voor de wetenschappelijke gemeenschap, en nog steeds is het probleem niet opgelost. Dit onderzoek beoogt om een oplossing voor dit probleem te vinden en een basis te bieden voor verdere studies in dit onderzoeksveld.

Het uitvalpercentage en de stilstandtijd van windturbinewieken zijn relatief hoog. In het kader van preventief onderhoud is het noodzakelijk windturbinewieken periodiek te inspecteren. Wiekinspectie vereist speciaal gereedschap, bekwaame mankracht, vaartuigen en hijsapparatuur; wat dit onderhoud erg kostbaar maakt. Dit is de belangrijkste reden dat de windenergie-industrie gebruik wil maken van een betrouwbaar SGC-systeem, om zo het aantal periodieke wiekinspecties te minimaliseren. Echter bemoeilijkt de complexiteit in de wiekgeometrie de SGC van windturbinewieken. Verschillende onderdelen van een windturbinewiek worden met lijm aan elkaar verbonden. Deze lijmverbindingen, bijv. aan de voorkant, achterkant en de verbinding tussen spar caps en shearwebs, zijn belangrijke onderdelen van de wiekstructuur en spelen een essentiële rol in de integriteit van het geheel. Deze verbindingen zijn erg kwetsbaar voor vermoeiing.

Fabricagefouten en impact kunnen de oorzaak zijn van vermoeiing, als ook het proces versnellen. Impact kan ontstaan tijdens het transporteren of installeren van de wieken, vooral voor voor-de-kust-liggende windturbines. In deze studie, zal gebruik gemaakt worden van trillingen, akoestische- en infraroodthermografie om vermoeiingsschade te karakteriseren in testmonsters die representatief zijn voor de lijmverbinding tussen de spar cap en shear web van een windturbinewiek.

De testmonsters werden, voordat de vermoeiingstesten werden uitgevoerd, aan verschillende impactniveaus onderworpen door gebruik te maken van een gaskanonmachine, om zo het effect van impact op schadeverspreiding te bestuderen. Tijdens de vermoeiingstesten werden een Poly-tech laser vibrometer, een Vallen akoestisch systeem en een FLIR infrarood thermografiesysteem gebruikt voor trillings-, akoestische en thermografische analyse.

Verspreiding van schade

Het begrijpen van de verspreiding van vermoeiingsschade in een spar cap en shear web lijmverbinding is de eerste stap in het karakteriseren van de schade. Dwarsscheuren in het verlijmde deel van de testmonsters zijn als het belangrijkste drijfmechanisme voor de verspreiding van schade geïdentificeerd. In de test-

monsters die zijn onderworpen aan middelhoge en hoge energie-impact, wordt de schade geïnitieerd in de impactzone. Voortestmonsters die zijn onderworpen aan lage energie-impact, is dit echter niet altijd het geval. Na het ontstaan van dwarsscheuren nemen ze in lengterichting en dwarsrichting toe, waardoor de lijm loskomt van het laminaat. In de niet-impact proefmonsters zijn dwarsscheuren en het loslaten van de lijm van laminaat de dominante schadevormen. Bij de proefstukken die aan impact zijn blootgesteld, zijn naast dwarsscheuren en het loslaten van lijm van laminaat ook delaminatie van de laminaatlagen een belangrijke schadebron. Delaminatie treedt op in de impactzone en groeit tijdens de vermoeiingstesten.

Trillings- en thermografische analyse

Om de schade te karakteriseren werd de verandering in de dempingseigenschappen van een materiaal gebruikt. Dit is bepaald door een analyse van de trillingen en een infrarood thermografische analyse. Met behulp van trillingsanalyse, wordt de demping geschat op basis van een visco-elastisch model van een composiet materiaal. Bij de thermografische analyse wordt de demping berekend met een warmteoverdrachtsmodel van de proefstukken die aan de vermoeiingstesten worden onderworpen. De demping, berekend door infrarood thermografische analyse, blijkt meer overeen te komen met zichtbare schadeverspreiding. De demping van de testmonsters neemt toe wanneer de eerste tekenen van dwarsscheuren verschijnen. In de testmonsters die niet aan impact zijn onderworpen, neemt na het ontstaan van dwarsscheuren, de demping toe met een constante snelheid totdat de monsters verzadigd zijn met dwarsscheuren. Na deze fase neemt de mate van toename van de demping af en neigt deze af te vlakken. In de testmonsters onderworpen aan gemiddelde en hoge niveaus van energie-impact vlakkt de demping niet af dwarsscheurverzadiging. Dit is te wijten aan delaminatie in de impactzone, die blijft groeien na de verzadigingsfase.

Akoestische analyse

Akoestische analyses werden gebruikt om de verspreiding van schade in de proefstukken te monitoren. Het effect van verschillende impactniveaus werd bestudeerd. De snelheid van akoestische emissiegebeurtenissen en de ruimtelijke dichtheid van akoestische emissiegebeurtenissen werden gebruikt om de verspreiding van schade te monitoren. Voor de testmonsters die blootgesteld zijn aan de laagste energie-impact, werd het accumulatieproces van vermoeiingsschade niet echt beïnvloed door de grootte en locatie van de impactschade. Voor testmonsters die blootgesteld zijn aan de gemiddelde en hoge energie-impact, werd het vermoeiingsaccumulatieproces duidelijk beïnvloed door de grootte en locatie van de botsings schade.

1

INTRODUCTION

Structural health monitoring (SHM) systems can be an effective solution for monitoring the integrity of wind turbine blades. With the growing size of wind turbine blades and the increasing prevalence of offshore wind turbines, SHM can play an important role in reducing the risk of failure and avoiding unnecessary blade inspections. This potentially reduces the maintenance cost and makes wind energy more economic. This chapter gives a brief historical overview of structural health monitoring systems and its application to wind turbines. Moreover, the motivation behind this research, research objectives, and the approach to fulfilling these objectives are presented.

1.1. HEALTH MONITORING, A BRIEF HISTORICAL OVERVIEW

With the growth and evolution of human society and the development of roads, bridges, and transport systems, the performance and safety of these systems became a primary issue. In order to ensure their safety and reliability, engineers developed ways to identify their useful remaining life. However, the processes which give rise to the loading of such systems during operation are highly stochastic. Moreover, the material behavior of these structures under operational loads is not wholly predictable. So the engineers could only provide an estimation of the useful remaining life of these structures.

To preserve the safety of the system, periodic monitoring of these structures was seen as the most viable option. Later on, it was discovered even with such a monitoring procedure, the safety of a structure could not be guaranteed because the monitoring and inspection of the system took place at specific intervals, and between these intervals, the state of the structure was not clear. Furthermore, for some structures, the monitoring of inaccessible areas and internal parts was not feasible.

These concerns led to the advent of the structural health monitoring (SHM) concept. Although the concept of SHM may date back to the origins of structural engineering, this field did not really become established as a research field until the 1980s [1].

Developments in sensor technology, especially the strain gauge, which entered the market in a large quantities in 1953, and further development of thin film technology in 1970, played an important role in the establishment of the structural health monitoring [2].

The purpose of SHM was to identify the evolution of damage over time in a structure. Reduction in maintenance costs by employing robust SHM encouraged stakeholders to invest more in developing the technique further.

1.2. APPLICATION OF STRUCTURAL HEALTH MONITORING TO A WIND TURBINE

To make wind energy more competitive, it is necessary to reduce its Levelized Cost of Energy (LCoE). The operation and maintenance of wind turbines is a major cost contributor to LCoE (Levelized cost of energy) especially where turbines have been installed offshore.

Offshore maintenance requires more coordination between different parties, employing large vessels, transferring crews and equipment, docking, and lifting operations. [3].

Operation and maintenance costs of offshore wind turbines may easily make up 25-30 % of the total LCoE averaged over the turbine lifetime. If the turbine is fairly new, the share may only be 20-25 %, but this might increase to at least 30-35 % by the end of a turbine's lifetime [4].

A cost analysis of wind energy performed by NREL (National Renewable Energy Laboratory of the U.S. Department of Energy) in 2019, [5], showed that operation

and maintenance costs amounted to 31.4% and 34.3% of LCoE for land-based and offshore based wind projects respectively, figure 1.1.

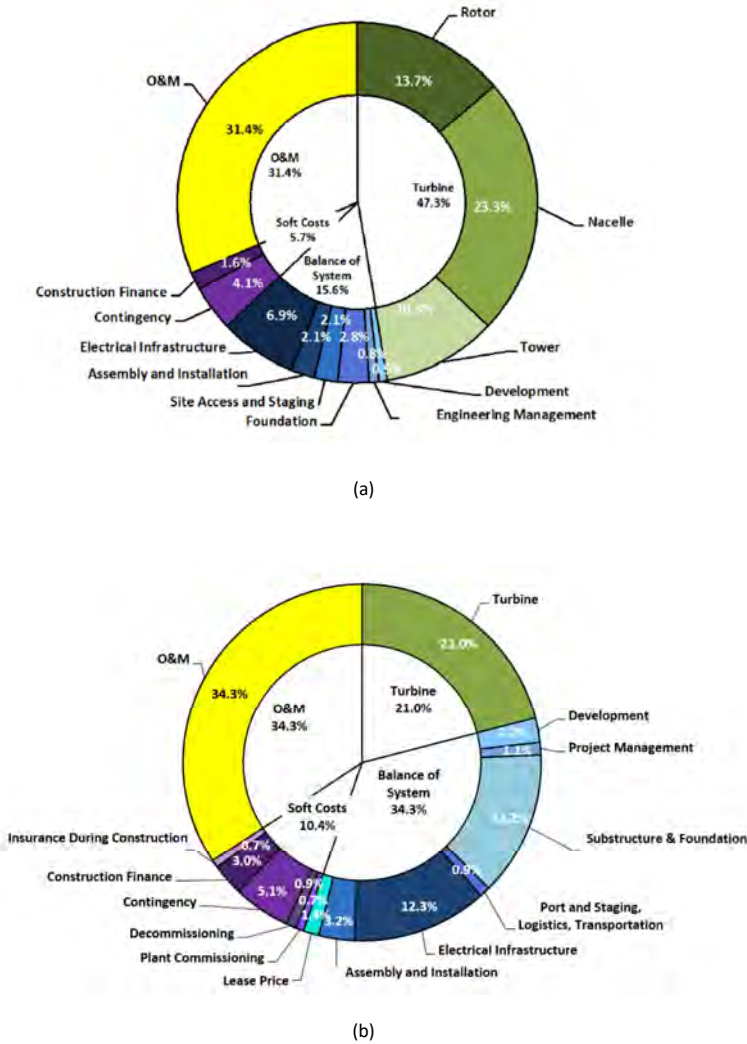


Figure 1.1: (a) Component-level LCoE contribution for a 2019 land-based wind reference project operating for 25 years (b) as (a) but for an offshore project [5]

One approach to reducing the maintenance cost of wind turbines is to optimize the maintenance strategy. A maintenance strategy has three main elements:

preventive, predictive, and corrective maintenance. Preventive maintenance is periodically based-inspection of the components in the wind turbine to guarantee that they are operating in a healthy state. Predictive maintenance is the online monitoring of the components in the wind turbine by using a condition or health monitoring system. By using predictive maintenance, the condition of the components is monitored by sensors without having a visual (in person) inspection. Corrective maintenance is the repair of components after the occurrence of a failure.

To reduce operation and maintenance costs for a wind turbine, preventive maintenance activities should be reduced and replaced by predictive maintenance solutions. This means that fewer components should be planned for periodic inspection.

Blade inspection for offshore turbines is costly, requiring special tools, skilled manpower, vessels, and ship-based lifting equipment. For this reason, there is much effort to avoid the need for onsite inspections by using effective SHM tools.

One significant contributor to the cost of operation and maintenance of the wind farm is the number of turbines in the farm as they each require individual monitoring, visits and maintenance activities. This becomes even more significant if the turbines are located offshore. One approach to reducing this cost per unit of energy generated is to increase the size of the wind turbines, thus reducing their number for the same installed capacity. In Figure 1.2, the past and future evolution in rotor size is shown. This growth has been partly driven by the need to reduce the per kWh cost of turbine maintenance.

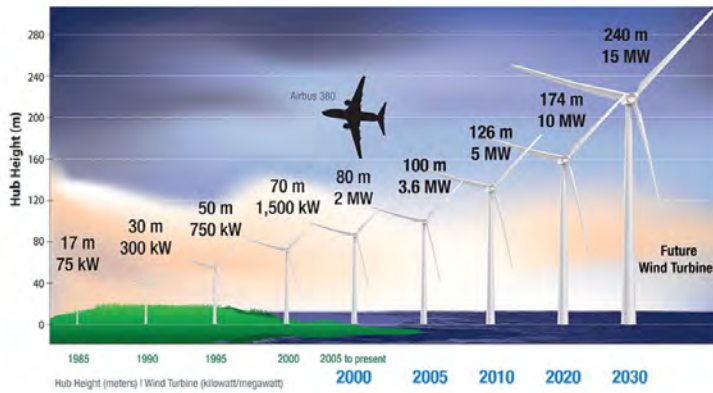


Figure 1.2: Evolution in rotor size since 1985, Photos from, "The Leading Edge: April 2020 Wind Energy Newsletter, NREL.

One of the significant challenges that arises as wind turbine blade size increases is that of its reliability. Wind turbine blades experience a fatigue load, and they are exposed to environmental conditions, e.g., rain, hail, ice, dust, and lightning. These lead to both internal damage such as cracks, delamination, and

de-bonding and external damage such as wear, corrosion, and erosion.

The failure rate and downtime of the main components of a wind turbine collected from 18 publicly databases, including over 18000 wind turbines, are shown in Figure 1.3 and 1.4,[6]. The blade (including hub) failure rate for an onshore wind turbine is 8.3% which is of the same order as other components except for the pitch and the generator system, which have higher failure rates. The equivalent failure rate for an offshore wind turbine is 15% which is quite high in comparison with other components. The downtime of the blade for an offshore and onshore wind turbine are 22.2% and 18.2%, respectively .

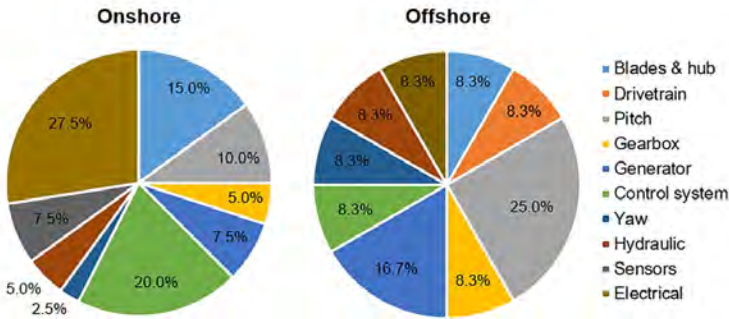


Figure 1.3: Failure rates of the main components of a wind turbine,[6].

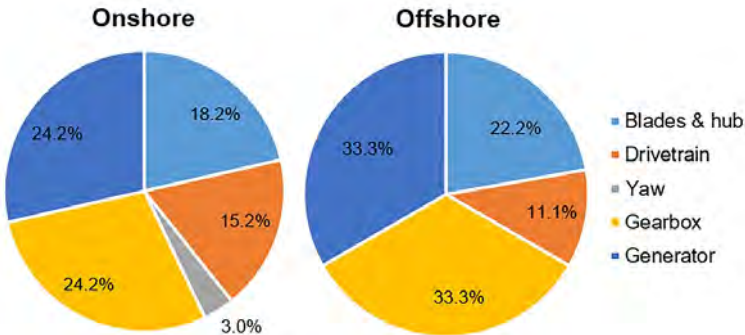


Figure 1.4: Downtime of the main components of a wind turbine, [6].

Although the failure rate of the blade may be less than other components, its downtime is much higher compared with other components. The failure of the blade may cause the collapse of the whole turbine structure. This not only leads to the loss of the revenue but also endangers the life of people who may be in the vicinity.

To increase the reliability of wind turbine blades, SHM tools can be used. SHM tools monitor the condition of the blade and, using this information, can help to

prevent blade failure. This increases reliability and avoids unnecessary inspection, which is very costly for offshore wind farms.

Several health monitoring techniques, including those using vibration, strain gauges, acoustic, ultrasonic, thermography, and blade deflection measurements, can be used to monitor the state of the blade [7].

Health monitoring systems for wind turbine blades are still in an early phase of development and need more work to be deployed effectively. The main difficulty is the lack of appropriate methods to monitor the condition of the blade reliably. There are a few health monitoring systems available in the market which mostly use strain gauges to monitor the load on some critical areas of the blade, such as the root. However, these monitoring systems are not reliable, and visual inspection is still necessary [7].

1.3. MOTIVATION AND PURPOSE OF THE THESIS

A wind turbine blade consists of different parts, as shown in Figure 1.5. Many of these parts are connected together by means of adhesive. With the increasing size of wind turbine blades, the thickness of blade components is also increasing requiring thicker layers of adhesive for bonding.

Increasing the thickness of the adhesive joint makes them more vulnerable to fatigue damage. To increase the reliability of the wind turbine blade, the establishment of an SHM technique to monitor the condition of these thick adhesive joints is essential.

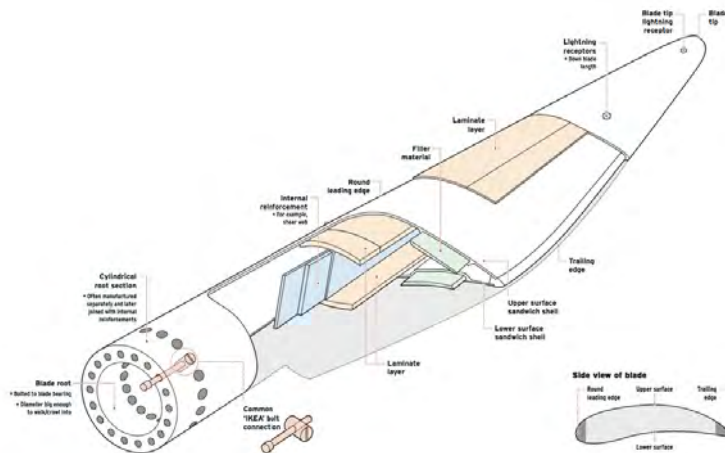


Figure 1.5: Schematic illustration of the different parts of a wind turbine blade.

1.3.1. PROBLEM DESCRIPTION

The spar cap to shear web adhesively-bonded connection in a modern wind turbine blade is a key element that contributes to its structural integrity. This con-

nection suffers from damage at the bond-line, which can propagate through the structure and compromise its structural integrity [8, 9]. With the ever-increasing size of wind turbine blades, particularly for offshore machines with lower accessibility, deploying a health monitoring technique to detect damage in these areas and take appropriate maintenance actions will become essential [10],[11].

Due to the turbulent characteristics of the wind, wind turbine blades experience a stochastic load. But wind shear, rotation of the blades, and tower shadow add cyclic components to this load. This causes a blade in operation to experience a higher fatigue load in comparison with a blade which is stationary. When the blades rotate, they interact with different eddy sizes around the swept area of the rotor. This leads to the phenomenon called rotational sampling and induces different load frequencies at integer multiples of the blade rotational speed. This causes a fatigue load which is one of the main sources of cracks, delamination, and de-bonding in the spar cap to shear web adhesively-bonded connection. Damage occurs especially in areas where manufacturing flaws are present.

During the installation of a blade, especially for an offshore wind turbine, the blade may hit the hub or tower. The impact area can also be a potential source of cracks which can grow in the presence of a fatigue load. It is necessary to consider the risk of impact damage and its effect on damage propagation particularly in bonded connections such as the spar cap to shear web. This is a novel subject which has seen little research to date. One rare theoretical study investigated the distribution of impact energy after a lifted blade had its leading edge impacted by the tower[12]. The results showed that 7–20% of the impact energy was absorbed as damage in the blade. There has been no other work to the author's knowledge and especially no experimental work to show the propagation of damage after impact to a spar cap-shear web adhesively-bonded connection of a wind turbine blade.

1.3.2. RESEARCH QUESTIONS

In this study, the following research questions are addressed:

- How does fatigue damage resulting from a tension load propagate in a test specimen representative of the spar cap to shear web adhesively-bonded connection of a wind turbine blade?
- What is the effect of different levels of energy impact on the fatigue damage propagation resulting from a tension load in a test specimen representative of this type of connection?
- What are the advantages and disadvantages of using different structural health monitoring techniques to investigate damage propagation in this type of connection?

1.3.3. OBJECTIVES

The objectives of this research can be divided into two parts:

- To investigate the propagation of damage in a spar cap to shear web adhesively-bonded connection in the presence of a fatigue load with and without initial impact damage.
- To assess different structural health monitoring techniques, including vibration, acoustic emission, and infrared thermography, to characterize fatigue damage in such a joint.

1.4. THESIS STRUCTURE

The thesis has been divided into six chapters. The main elements of each chapter have been explained as following:

chapter 1:

In this chapter, a short introduction to the history of structural health monitoring and its application to the wind turbine have been given. Then the motivation behind this research and the main objectives of the thesis, and the methodology to fulfill the research objectives have been described.

chapter 2:

In this chapter, the applications of different sensors used in vibration, acoustic, and infrared thermographic monitoring systems of wind turbine blades are discussed. This chapter covers the following topics:

- Introduction to different sensor technologies used in vibration, acoustic, and thermographic monitoring systems.
- Investigation of the ease of installation and level of accuracy of such technologies.
- Discussion concerning practical solutions for using vibration, acoustic, and thermographic monitoring systems in a wind turbine blade.

chapter 3:

In this chapter, the vibration analysis of the test specimen to characterize damage is presented. This chapter covers the following topics:

- Introduction to vibration technique and the different methods used in this technique.
- State of the art of the vibration analysis
- Test specimen properties and its manufacturing process.
- Experimental setup and data measurements.
- Viscous-elastic damping model of vibration in 1D and 3D space.
- Finite element modeling of the test specimen.

- A new localization approach based on the change in the phase of mode shape components.
- Results, discussion, and conclusions.

chapter 4:

In this chapter, the acoustic analysis of the test specimen to characterize damage is presented. This chapter covers the following topics:

- Introduction to the acoustic technique.
- State of the art of the acoustic analysis
- Creation of different impact levels on the test specimens.
- Experimental setup and data measurements.
- Methodology used to characterize fatigue impact damage.
- Results, discussion, and conclusions.

chapter 5:

In this chapter, the infrared thermographic analysis of the test specimen to characterize damage is presented. This chapter covers the following topics:

- Introduction to infrared thermographic analysis.
- State of the art of infrared thermography
- Experimental setup and data measurements.
- Methodology to characterize damage in the test specimens.
- Results, discussion, and conclusions.

chapter 6:

In this chapter, the finding of the thesis, the challenges, and future studies are presented.

2

APPLICATION OF DIFFERENT SENSORS FOR SHM OF A WIND TURBINE BLADE

Although widespread structure health monitoring of blades in operation is still mostly restricted to visual inspection, there is significant potential for the use of additional techniques to provide insight into internal damage. In this chapter, applications of different sensors that could be used in vibration, acoustic, and thermographic health monitoring systems of wind turbine blades are investigated. The ease of installation and accuracy of these sensors for the establishment of vibration, acoustic, and thermographic health monitoring systems in an operational wind turbine is discussed.

2.1. INTRODUCTION

The application of vibration, acoustic, and infrared thermographic techniques for wind turbine blade monitoring has been studied in the laboratory using conventional sensors. Using such sensors on a large operational wind turbine blade with a lifetime of 20-25 years may not be so straightforward, especially since conventional vibration and acoustic sensors cannot be easily attached to a wind turbine blade.

Micro-electromechanical systems (MEMS) and fiber optic sensors are devices that can be used in a vibration and acoustic monitoring system for a wind turbine blade. These sensors are thin and small, so they can easily be attached to or embedded into the wind turbine blade. MEMS technology has been improved over the years, and MEMS sensors can give an effective measurement of vibration. However, they do not sufficient sensitivity to capture low-energy acoustic (elastic) signals which result from such as cracks in a solid structure.

Fiber optic technology has also seen significant development, and is suitable for measuring both vibration and acoustic signals at specific points along a cable.

2.1.1. CHAPTER OVERVIEW

This chapter tries to address the challenges and possible solutions for the deployment of SHM in an operational wind turbine blade. This chapter covers the following topics:

- Sensors used in vibration-based SHM and possible solutions for the deployment of vibration monitoring systems in a wind turbine blade.
- Sensors used in acoustic-based SHM and possible solutions for the deployment of acoustic monitoring systems in a wind turbine blade.
- Sensors used in thermographic-based SHM and possible solutions for the deployment of thermographic monitoring systems in a wind turbine blade.

2.2. A VIBRATION-BASED SHM SYSTEM FOR A WIND TURBINE BLADE

Vibration-based SHM can be conducted using conventional piezo- electric, MEMS accelerometers, fiber optic sensors, and laser vibrometers.

Conventional piezoelectric sensors are difficult to use in a vibration-based SHM system for a wind turbine blade. Conventional piezoelectric sensors have been installed on wind turbine blades[13]. However, as well as adding cost, these sensors are vulnerable to damage during the 20-25 year lifetime of a wind turbine.

MEMS accelerometers and fiber optic sensors are potentially more suitable for blade monitoring as they can relatively easily be attached to or embedded in the composite material during the manufacturing of the blade.

A laser vibrometer can also be used for vibration measurements of a wind turbine blade. It can measure the displacement of a wind turbine blade from a

100-meter distance, but requires a measurement platform to set up the camera, which is potentially costly.

2.2.1. CONVENTIONAL VIBRATION SENSORS

Conventional piezoelectric sensors are a mature technology. They are very accurate and sensitive to the vibrational response of the structure. In these sensors, a moving mass exerts pressure on a piece of piezoelectric material leading to the generation of an electrical signal. The force exerted on the piezoelectric material due to the movement of mass depends on the acceleration of the structure. Figure 2.1 shows a schematic illustration of the different parts of a conventional piezoelectric accelerometer. They are relatively bulky and are not straightforward to install on a blade in the numbers required for effective monitoring.

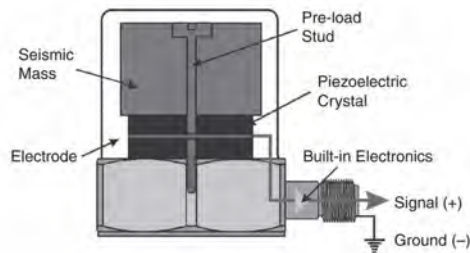


Figure 2.1: Schematic illustration of a compression type accelerometer and its different parts [14]

ACTUAL USE CASE OF CONVENTIONAL VIBRATION SENSORS FOR SHM OF A WIND TURBINE BLADE

The vibration of a wind turbine blade can be measured in an active or passive mode. In an active mode, an actuator is used to excite the blade, and acceleration sensors are used to measure the response of the blade. In a passive mode, the wind acts as the source of excitation.

Tcherniak et al. (2017) used an active mode system to carry out vibration-based structural health monitoring of an operational Vestas V27 wind turbine blade, [13]. The Vestas V27 is an old turbine type that has a rated power of 225 kW and a rotor diameter of 27 m. The blade was instrumented with 12 monoaxial piezoelectric accelerometers (Bruel and Kjar type 4507-B). The nominal sensitivity of the accelerometers was $10 \frac{mV}{m/s^2}$ (Type 4507-B-004), except for the accelerometer located near the actuator which had a nominal sensitivity of $1 \frac{mV}{m/s^2}$ (Type 4507-B-001). The actuator used to excite the blade consisted of a coil mounted on a steel base driven by an electrical pulse. The coil was used to drive a plunger in contact with the blade restored to its initial position after each pulse by means of a spring. Figure 2.2(a) shows the position of the accelerometers and their corre-

sponding cables and Figure 2.2(b) shows a schematic illustration of the actuator, the actual installed actuator, and its position on the blade (b).

To mount the accelerometers, the plastic mounting clips were glued directly to the blade. No special alignment was performed and the accelerometers' measurement direction was normal to the blade surface. The accelerometers were covered by silicon, and helicopter tape was applied on top to give the silicon a smooth shape. The accelerometers and cables were attached to the downwind side of the blade.

The cables ran from the accelerometers toward the trailing edge and then from the trailing edge toward the blade root. The cables were glued to the blade with silicon and covered with helicopter tape. The accelerometers were connected to a data acquisition system (Brüel and Kjær Type 3660-C with two LAN-XI modules, a 12-channel input module Type 3053-B-120 and a 4-channel input/output module Type 3160-A-042). The actuator was controlled by a signal generator which generated a rectangular pulse causing a 100 mF capacitor to discharge across the actuator coil. For each impulse, the capacitor was charged using a 48 V potential from a DC/DC converter.

The data acquisition system and the electronics were placed in a waterproof box mounted to the inner surface of the spinner (2.3). The equipment was energized using a 24 V potential from the nacelle via a slip ring. The measured data (in total, 16 signals were sampled with 16,384 Hz frequency) were wirelessly transmitted from the rotating part to the nacelle via two Cisco wireless access points, one located inside the waterproof box and another installed in the nacelle.

Two pairs of antennas, two omnidirectional antennas attached to the hub and two directional antennas mounted inside the nacelle for holding an uninterrupted wireless connection, were employed. The Brüel and Kjær PULSE LabShop software controlled the data acquisition system. It was programmed to start data acquisition 10 seconds before an actuator hit and another 20 seconds after. Then the acquisition was stopped and the system waited for four and a half minutes before repeating. Thus every hour, 12 actuator hits and corresponding data sets were produced.

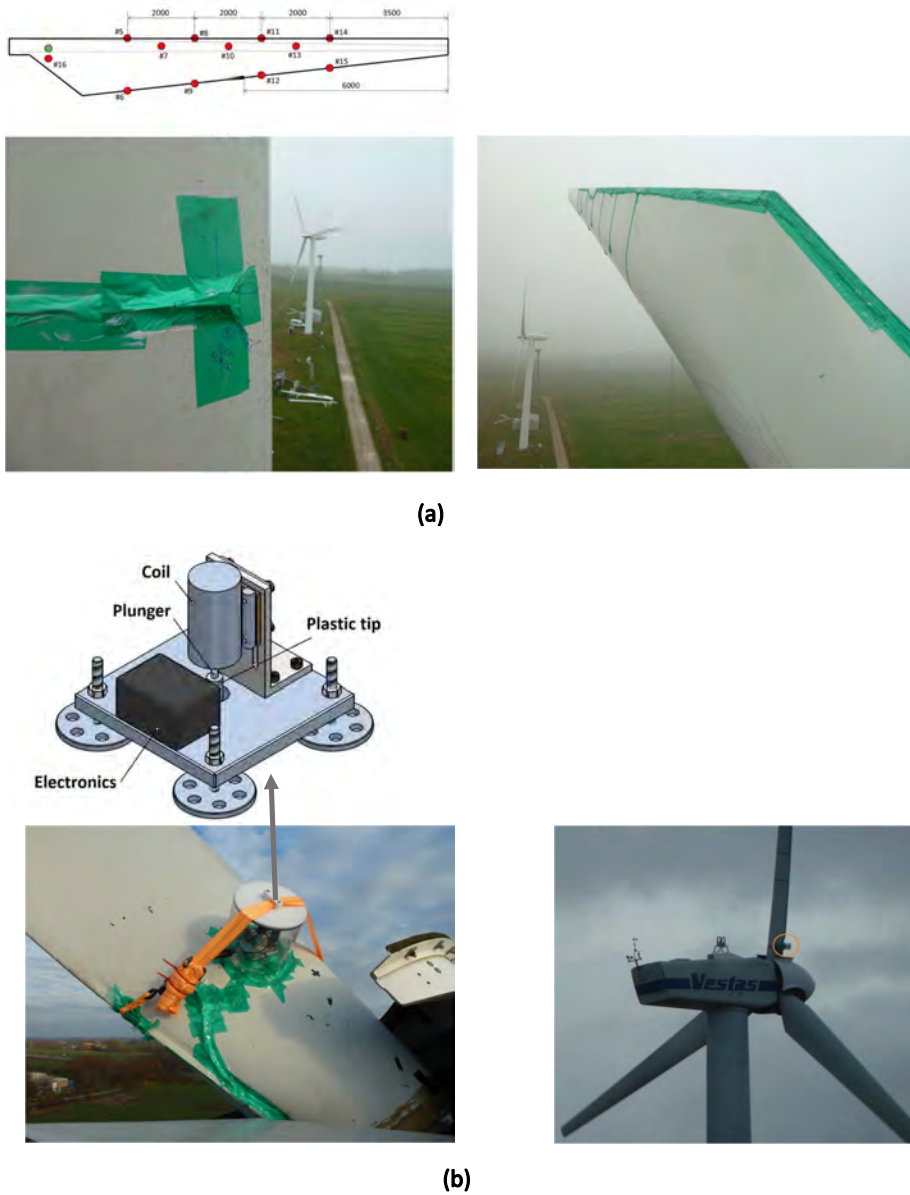


Figure 2.2: (a) The top figure shows a schematic illustration of the positions of the accelerometers and the bottom figures show the installed accelerometers and cable arrangements (b) the top figure shows a schematic illustration of the actuator and bottom figures shows the actual installed actuator and its position on the blade [13].



Figure 2.3: Data acquisition system: (a) the waterproof box with LAN-XI system and (b) the waterproof box mounted inside the spinner with the cables yet to be connected [13].

From this study it seems that the use of conventional vibration sensors is not practical for an operational wind turbine, however, it could be used in a small-scale experiment for research purposes.

2.2.2. MEMS VIBRATION SENSORS

MEMS sensors can be divided into four types, capacitive, piezoresistive, piezoelectric, and thermal accelerometers. The main element of a MEMS sensor is a movable mass that due to its inertia, reacts to the acceleration of a system. The effect of this mass on the sensing element of MEMS architect defines the type of MEMS accelerometers. In a common type of MEMS sensor, the capacitive accelerometer type, the moving mass changes the distance between a fixed and moving plate, leading to a change in the capacitance, Figure 2.4. Current research on the use of MEMS sensors for SHM has shown that the performance of these sensors is comparable with conventional piezoelectric vibration sensors. Villacorta et al. investigate the modal analysis of a structure by using a conventional and MEMS accelerometer [15]. It was concluded that although the performance of conventional accelerometers is better overall, both MEMS sensors and conventional systems are equivalent for use in modal monitoring of a structure.

Bedon et al. used MEMS sensors to perform modal analysis of a cable-stayed bridge in Pietratagliata (Italy) [16]. They assessed the capability and potential of using MEMS for experimental modal analysis by comparing the results with previous measurements and finite element modeling. It was concluded that MEMS sensors can deliver reliable data for the estimation of dynamic features of a structure using experimental modal analysis.

DiNuzzo et.al. and Girolami2017, et.al. also assessed the performance of MEMS sensors in comparison with conventional piezoelectric accelerometers [17, 18]. The two studies undertook a modal analysis of a steel building and a tower, re-

spectively, located on the engineering campus at the University of Bologna using MEMS sensors. Both studies confirmed the efficacy of MEMS sensors for modal analysis of building structures.

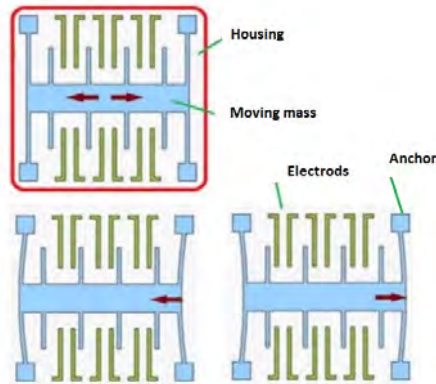


Figure 2.4: Schematic illustration of a capacitive accelerometer type MEMS sensor and its different elements [19]

ACTUAL USE CASE OF MEMS FOR SHM OF A WIND TURBINE BLADE

MEMS and sensors based on this technology are highly integrated, thin, and easy to deploy. They can even be mounted on a wind turbine blade during construction. Loss et al. (2020) used these sensors to measure the vibration of a 63 meter and 70 meter wind turbine blade [20]. The sensors were equipped with solar energy harvesting mini panels and rechargeable energy storage, to eliminate the need for cabling when the sensors are mounted on the outer side of a blade. In addition, they were equipped with wireless communication to transfer the measured data to a base station in the tower or nacelle of the turbine. An example of a mounted sensor and the sensor autonomous power system is shown in Figure 2.5.



Figure 2.5: (Left) A sensor mounted on the outside of a blade during the installation of a wind turbine. (Right) A sensor shown with autonomous power system[20]

Several sensors were used to cover various locations on the pressure side and suction side of the blades. The sensors consisted of a wireless prototype with triaxial MEMS accelerometers with a measurement range of 0.16 g and a sensitivity lower than 0.49 mg. Acceleration was measured at a sampling rate of 400 Hz (Prototype 1) and 833 Hz (Prototype 2), respectively, for a duration of 10 seconds. From this study it can be concluded that MEMS sensors could be mounted on an operational wind turbine to measure vibration data over a short period. The robustness of these sensors to adverse weather conditions is not clear as measurements were made for a limited three-month test period and the condition of the sensors after the test period was not reported.

2.2.3. FIBER OPTIC SENSORS

An optical fiber consists of a core with a high refractive index surrounded by a cladding with a lower refraction index. Additional layers, the buffer and outer jacket, both act as protective polymer layers. The core of fiber optic sensors, usually glass fibers, should be sufficiently small in size. This enables these sensors to be embedded into fiber-reinforced polymer composite materials. The embedding process protects these sensors against environmental effects and prolongs their operational lifetime. In addition, the immunity of fiber optic sensors to electromagnetic interference makes this type of sensor even more attractive for health monitoring of a structure, [21].

In comparison to conventional acoustic sensors, the costs of installation and maintenance of fiber optic sensors are less, and they have a long-term monitoring capability. Fiber optic sensors can be divided into point sensing and distributed sensing. In point sensing, specific parts of the fiber cable act as sensors, and in these particular areas the measurements are made. In distributed sensing, the whole cable acts as the sensor making these sensors very useful for spatial monitoring of structures [22, 23]. The classification and different types of sensors in each category are shown in Figure 2.9

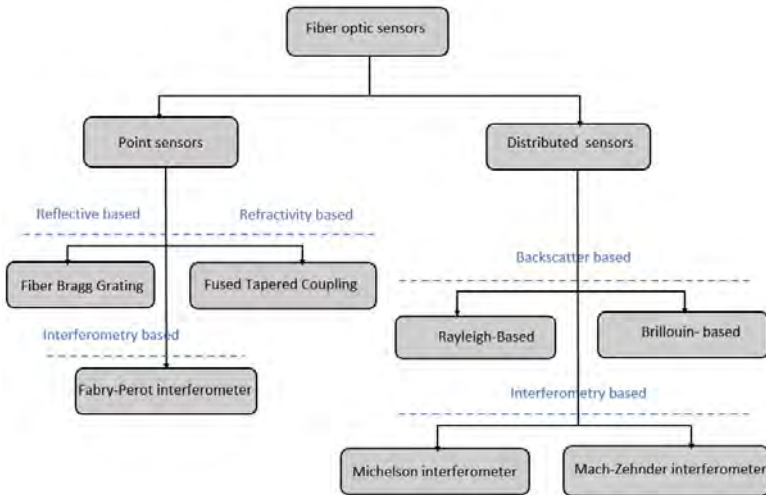


Figure 2.6: Fiber optic sensor classification used for measurements of acoustic emission elastic waves

Fiber optic vibration and acoustic sensors are light and very thin (on the scale of millimeters). This allows the sensors to be embedded inside the blade during manufacturing. In addition, they are very flexible and can easily cover the whole length of a blade. Moreover, optical fibers are immune to external electromagnetic fields, require a low power supply, and can transmit information at high speeds and for long distances in multiplexing on the same fiber [21, 24–26].

Fiber optic sensors detect changes in optical characteristics caused by bending or stretching of an optical fiber. When damage or cracking occur in a blade, energy released can distort a fiber optic cable situated close by (mounted either on the surface or embedded within) changing the reflection or refraction of light passing through it as the blade is flexed. Different types of fiber optic sensors and their working principles were discussed in Section 2.3.

Modal analysis of a structure can be performed using strain measured by fiber optic sensors. The studies of Anastasopoulos et al. showed that fiber optic sensors are sensitive and accurate enough to measure strain in different locations of a structure leading to accurate estimation of natural frequencies [27]. Casona et al. (2006) compared the modal analysis results of aircraft components using an embedded fiber-optic sensing system based on fiber Bragg gratings (FBGs) with conventional accelerometer sensors, [28]. It was concluded that there was good agreement between the natural frequencies determined using the accelerometers and those determined using the FBGs. From this study it seems that MEMS sensors can be installed on an operational wind turbine blade and vibration data can be measured within the entire blade span.

ACTUAL USE CASE OF FIBER OPTIC SENSORS FOR VIBRATION-BASED SHM OF A WIND TURBINE BLADE

2

FBGs detect a shift in wavelength due to changes in local strain. FBGs are placed at discrete intervals along a fiber optic cable and therefore can only measure vibrations at these locations. In contrast, Optical Backscatter Reflectometry (OBR) sensors measure changes in the Rayleigh or Mie scattering of light from nanoparticles in an optical fiber which allows the detection of strain at any point along the fiber in principle.

Cazzulani et al. (2021) monitored vibration of scale model wind turbine blades with FBGs and OBR sensors [26] installed along the whole length of a blade. The blades were part of a 1:75 scale model turbine with a total length of 11 m from the root to the tip, made of a 3 mm thick carbon fiber layer, Figure 2.7. Results were compared with conventional piezo-electric vibration sensors and it was concluded that the FBGs fiber optic sensors could measure the vibration of wind turbine blades as efficiently as the conventional vibration sensors. The performance of FBG sensors is better than OBR sensors as they provide vibration measurements which better match those of conventional piezo-electric vibration sensors. The FBGs provided fewer measurement points but more with more precise information, and their signal quality was high. The OBR sensors, on the other hand, could make measurements at many point (providing virtually continuous measurements along the fiber) but with lower signal quality.



Figure 2.7: Scale model wind turbine with fiber optic sensors installed on the blades.

In an attempt to develop and validate a condition monitoring system for wind turbine blades, five companies, including TWI, Renewable Advice, EWT, Halliburton, and ASSIST, came together in the EU Horizon 2020 BladeSave project to combine their expertise in structural health monitoring (SHM) using fiber optic sensing technology [29]. The BladeSave project aimed to develop a system that offers multi-sensing capabilities, including acoustic emission (AE), vibration, and strain, achieved with FBG sensors. The system was successfully established on a wind turbine of the project partner EWT for three months. During this period, SHM data including AE, vibration and strain were recorded. Moreover, the BladeSave system was tested for the detection of ice accretion on blade surfaces using simulated mass showing evident detection capabilities. The final stage of the project was the destructive testing of a wind turbine blade conducted at TWI.

2.3. ACOUSTIC-BASED SHM OF A WIND TURBINE BLADE

Acoustic emission sensors can be divided into three main categories: conventional piezoelectric sensors, MEMS sensors, and fiber optic sensors. Conventional piezoelectric and MEMS sensors work based on the properties of an electrical signal, while fiber optic sensors use light.

2.3.1. CONVENTIONAL AE SENSORS

Acoustic emission in structures is primarily measured by conventional piezoelectric sensors. The transducer in these sensors is made from piezoelectric crystals such as lead zirconate titanate (PZT) which converts the mechanical movement of vibrating surface to an electrical signal. Transducers are selected based on operating frequency, sensitivity, and environmental characteristics and are grouped into two classes: resonant and broadband. A schematic of an AE sensor and how it is used to monitor damage is shown in Figure 2.8.

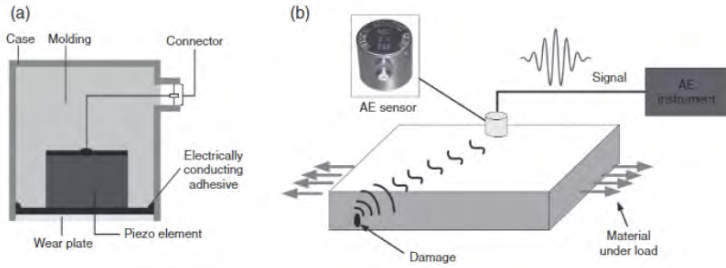


Figure 2.8: (a) Schematic illustration of the structure of a conventional piezoelectric acoustic sensor, (b) how acoustic emission is used to monitor damage [30]

Although these sensors are well developed, they have the same problem as conventional vibration sensors in terms of how to attach them to a wind turbine blade and operate them continuously for the 20-25 year lifetime of a wind turbine.

2.3.2. ACOUSTIC MEMS SENSORS

Acoustic MEMS sensors convert the movement from vibrating surfaces to an electrical signal using three main principles: piezoresistivity, capacitance, and piezoelectricity, [31, 32]. The working principle of acoustic MEMS sensors is similar to those which are vibration-based. They both work on the basis of a mass-damper-spring system on a micro-scale. The difference is in their operating frequency; while acoustic MEMS sensors operate at the resonant frequency of the microstructure, accelerometer MEMS operate below the resonant frequency [33]. The main drawback of acoustic MEMS sensors is their low sensitivity, so their application is limited to the detection of high energy source damage such as wire breaks [31]. They are not suitable for detecting low-energy AE source damage such as cracks in composite materials. Comparing conventional and piezoelectric acoustic MEMS sensor performance shows that the shapes of signals recorded by both sensors are similar. But, the amplitudes of signals recorded by conventional piezoelectric acoustic sensors are two orders of magnitude higher than those of piezoelectric acoustic MEMS sensors [33].

2.3.3. FUSED TAPERED COUPLER SENSORS

Fused tapered coupler sensors have been well developed for AE measurements [21]. A schematic illustration of a fused tapered coupler sensor is shown in Figure 2.9. These sensors are manufactured by placing two single-mode optical fibers in close parallel contact, stretching them under a hydrogen flame and fusing them together as shown in Figure 2.9.

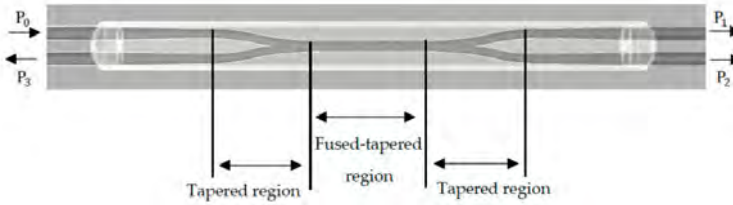


Figure 2.9: A schematic illustration of a bi-directional fused tapered coupler sensor where P_0 is the input light power source, and P_1 and P_2 are the power outputs. P_3 is the backscattered power. [21]

When an external acoustic source produces an elastic wave, it excites the coupler and the elastic wave propagates along the coupling region. This propagation changes the length of the coupler and changes the optical power outputs. This change in the outputs is used to measure the acoustic emission waves. Fu et al. used these fiber optic sensors to measure the acoustic emission in unidirectional carbon fiber reinforced plastics (CFRP) materials. The sensor was embedded in the middle layer of a test specimen with dimensions of 200 mm × 15 mm × 1.5 mm. They compared acoustic measurements from both conventional surface-mounted and embedded monitoring sensors under a quasi-bending load. The results showed that fused tapered coupler sensors could detect elastic waves resulting from damage in the specimen [34]. In another experiment, Fu et al. embedded the same type of sensor in a CFRP plate to detected impact damage [35]. By using four fused tapered coupler sensors, they were able to identify the location of the impact source.

2.3.4. FIBER BRAGG GRATING SENSOR

In its basic form, a fiber Bragg grating (FBG) sensor is made by exposing a segment of Ge-doped single-mode fiber core to a spatial pattern of ultraviolet light in the 244–248 nm region [36]. Each pattern is called a grating, as shown in Figure 2.10. These patterns (gratings) cause the periodic modulation of the core refractive index, which in turn reflects a specific wavelength of the input light. Any elastic wave, as it passes through the cable, changes the grating distances and the wavelength of the reflected wave.

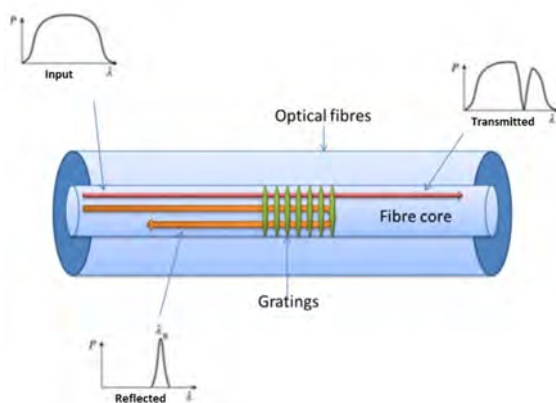


Figure 2.10: Operating principle of a fiber Bragg grating (FBG) sensor, [37].

Zhang et al. (2017) compared the performance of FBG and conventional piezo-electric sensors by measuring the characteristics of elastic waves generated by an aluminum plate impacted by a ball. They concluded that the FBG sensors could detect the AE events and could potentially be used for structural health monitoring, [38]. Other researchers have evaluated FBG sensor performance, and have reached similar conclusions, [39, 40].

2.3.5. INTERFEROMETRY BASED SENSORS

Mach-Zehnder, Michelson, and Fabry-Perot interferometer sensors make use of a coherent light source to detect very small displacements.

In the case of a Mach-Zehnder interferometer, the coherent light from a laser is sent down a fiber cable and is split into two arms using a beam splitter. One beam is used as a reference, and the other is exposed to an external perturbation such as an acoustic wave. These two beams are then re-merged and sent to a detector as shown in Figure 2.11. The acoustic wave changes the optical path in the sensing arm compared with the reference arm which in turn creates a phase difference between the re-merged coherent optical light sources which can be measured using an appropriate detector. A Michelson interferometer (shown in Figure 2.12) uses a similar principle based on mirrors. Both Mach-Zehnder and Michelson sensors, by measuring changes in reference and sensing beams, detect changes integrated over a path are known as distributed sensors.

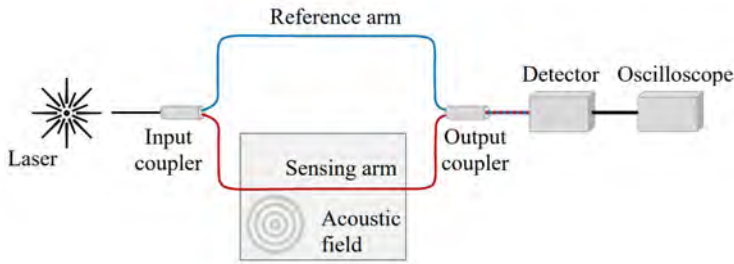


Figure 2.11: Schematic illustration of Mach-Zehnder interferometer, [41].

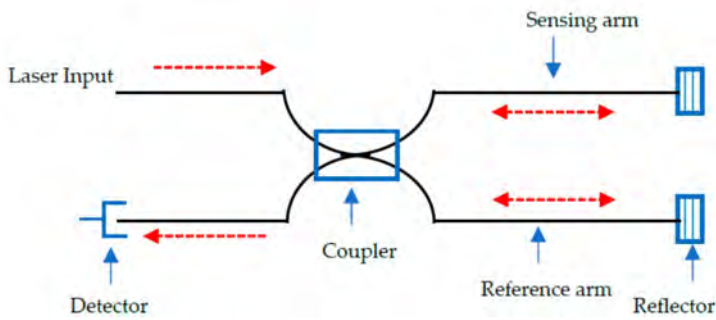


Figure 2.12: Schematic illustration of Michelson interferometer, [41].

A Fabry-Perot interferometer is a point sensor. It uses a reflector cavity composed of two parallel highly reflective surfaces separated by a certain distance as shown in Figure 2.13. An acoustic wave changes the cavity length and thus the phase difference between the light reflected from one end of the cavity (connected to a diaphragm exposed to the acoustic wave) and the other end of the cavity which is fixed. This phase difference is thus representative of the change in displacement local to a point [42].

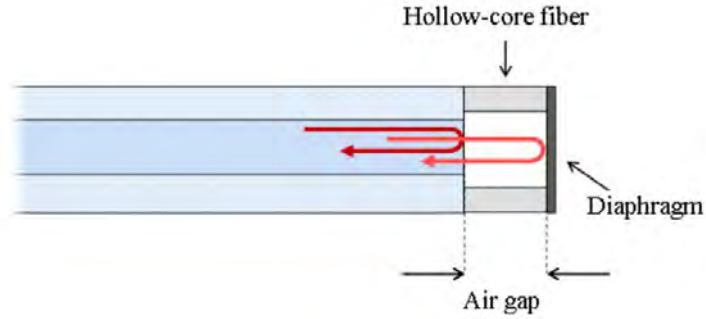


Figure 2.13: Schematic illustration of Fabry-Pérot interferometer, [41].

The sensors described above are suitable for measuring acoustic waves having frequencies up to MHz, which is suitable for the detection of micro-cracks [43]. Further studies have also shown that interferometry sensors are suitable for measuring acoustic emissions [41, 44–46].

2.3.6. BACK SCATTERING BASED SENSORS

Some proportion of the light that travels in a fiber optic cable is reflected back or backscattered. When the cable is in contact with a surface which experiences an acoustic wave, this changes its back-scattering characteristics. Scattering of light in a fiber optic cable is due to three main scattering processes: Rayleigh, Raman, and Brillouin [47]. The nature of these scattering processes depends on the interaction of photons (light) with the molecules and atoms of the fiber material. More details about the different mechanisms which lead to Rayleigh, Raman, and Brillouin scattering can be found in Bao et al. [48]. A typical spectrum of backscattered light within a fiber optic cable is shown in figure 2.14. In this figure, The contributions from the Rayleigh, Raman and Brillouin scattering processes are shown.

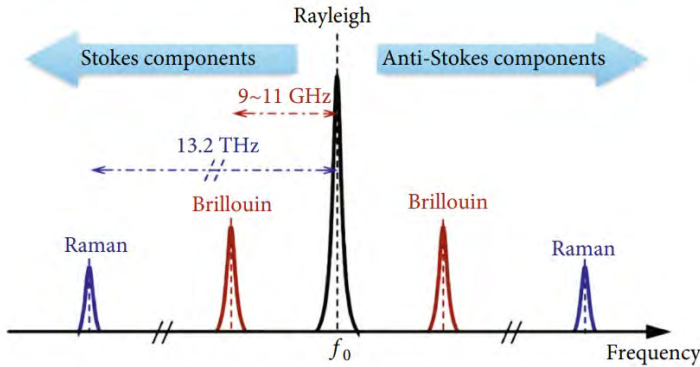


Figure 2.14: A typical spectrum of backscattering light in a fiber optic cable [48].

The light source projected down a fiber optic cable is normally a narrow band optical pulse or a frequency-modulated continuous wave signal (CWS). The analysis of back-scattered light based on a narrow band optical pulsed source is called optical time domain reflectometry (OTDR), and the analysis of back-scattered light based on a frequency-modulated continuous wave signal (CWS) is called optical frequency domain reflectometry (OFDR). The basic configuration of a device based on the Rayleigh back-scattering method is shown schematically in figure 2.15.

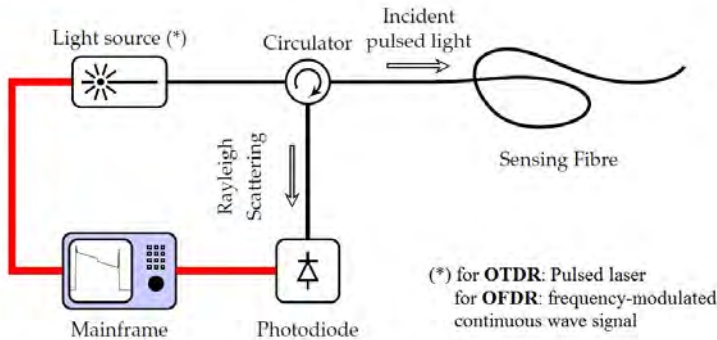


Figure 2.15: Schematic of a device for measuring acoustic waves based on the Rayleigh back-scattering method [47].

A narrow band optical pulse or frequency-modulated continuous wave signal is sent down the fiber optic cable. A circulator guides the backscattered light to a photodetector and prevents it from returning back to the source path. When a sensing fiber experiences an acoustic wave source, it is alternately stretched and compressed thus changing the characteristics of backscattered light.

When detecting acoustic waves from Brillouin scattering, a combination of OTDR and OFDR is used. The basic configuration of a device based on Brillouin scattering is shown in figure 2.16.

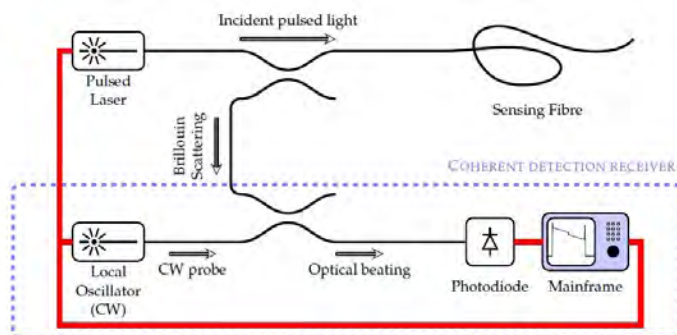


Figure 2.16: Schematic of a device for measuring acoustic waves based on Brillouin scattering [47].

The proportion of Raman backscattered light is mostly only affected by the temperature [49] whereas Rayleigh and Brillouin backscattered light are affected by both temperature and acoustic waves (strain). Therefore the Rayleigh and Brillouin back-scattered light are usually used to detect an acoustic wave source.

Sensors employing Rayleigh and Brillouin back-scattering for the purposes of detecting acoustic waves have developed enormously in the past ten years [48]. However, such sensors have not yet been used to detect damage in a wind turbine blade. The advantages of these sensors are that they could be embedded in the blade structure, and they have the capability to make continuous spatial measurements over a long distance (blade length of 100 meters or more). Having these advantages and considering development trends during recent years, it should be possible to see these types of sensors used more widely in wind turbine blades in the near future.

2.4. THE POTENTIAL FOR A THERMOGRAPHIC SHM SYSTEM FOR A WIND TURBINE BLADE

During the operation of a wind turbine, due to fatigue load and structural damping, heat is generated within the blade structure and especially the adhesive joints. Any damage in these joints causes extra generation of heat, leading to an excessive increase in temperature.

Thermographic techniques could effectively detect and quantify damage in composite materials, especially damage to the adhesive joints in a wind turbine blade. Damage could be quantified by estimating the loss factor of the damaged parts from temperature measurements. The temperature of a wind turbine blade could be measured using an infrared camera or fiber optic sensors.

2.4.1. THERMOGRAPHIC ANALYSIS USING AN INFRARED CAMERA

There are two main types of infrared camera: fixed and portable. A fixed infrared camera could be installed within the wind turbine blade. Figure 2.17 shows a photo of a fixed infrared camera developed by the FLIR company. Using this camera, the condition of adhesive joints in an operational wind turbine could be monitored continuously.



Figure 2.17: Photo of a FLIR A310 f, a fixed type infrared camera which could be installed inside the wind turbine blade, taken from FLIR website, [50]

Figure 2.18 shows a photo of the spar cap-shear web assembly of a wind turbine blade. As seen in this photo, there is enough space inside the blade to install an infrared camera and monitor the condition of this assembly by measuring its temperature. Although an infrared camera could effectively detect damage in adhesive joints, the number of cameras and the cost of implementation of this system to record and transfer data is still high at present.



Figure 2.18: Photo of the shear web assembly of a wind turbine blade taken from the inside of a blade,[51].

2.4.2. THERMOGRAPHIC ANALYSIS USING FIBER OPTIC SENSORS

Fiber optic sensors can be embedded in composite materials, and they could be an appropriate candidate for measuring the temperature of a wind turbine blade. Fiber Bragg grating (FBG), continuous fiber Bragg grating, and Raman scattering distributed temperature sensors are possible candidates for measuring temperature [52]. Drusova et al. evaluated the performance of these three types of fiber optic sensors for groundwater temperature measurements. They concluded that all these sensors had a comparable accuracy of around 0.2°C with a resolution of less than 0.1°C .

Mikolajek et al. discussed different fiber optic sensors suitable for temperature measurement [53] concluding that temperature measurements by fiber optic sensors based on blackbody and grey body radiation, luminescence, fiber Bragg gratings (FBGs), and interferometers were being extensively developed. Ramakrishnan et al. presented a comprehensive overview of fiber optic sensors for measurement of temperature in composite materials [54]. They concluded that embedded temperature fiber optic sensors are useful in smart sensing applications for composite materials in a wide range of areas, including aerospace and civil structure. They believed that extensive research and development in this field would inevitably make this technology more commercially feasible.

Szczerska reviewed the latest developments in Fabry–Pérot interferometer fiber optic temperature sensors made with polymer technology [55]. Low cost is a big advantage of these types of sensors. The relatively limited temperature range in which such sensors can measure (between -55°C - 105°C) properly seems to be the main limitation, but this range is enough for temperature monitoring of a wind turbine blade.

3

VIBRATION ANALYSIS

This chapter discusses the use of vibration analysis to characterize damage in test specimens representative of spar cap-shear web adhesively-bonded connections. Damping is estimated by measuring the vibration response of the test specimens, and then the change in damping is correlated to the damage level. The effect of an increase in local damping on the phase of the components of the mode shapes is used to localize damage.

S. Khoshmanesh, S.J. Watson, D. Zarouchas, The effect of the fatigue damage accumulation process on the damping and stiffness properties of adhesively bonded composite structures, Compos Struct, 287, 2022.

S. Khoshmanesh, S.J. Watson, D. Zarouchas, New indicator for damage localization in a thick adhesive joint of a composite material used in a wind turbine blade, Engineering Structures Volume 283, 2023.

3.1. INTRODUCTION

A structural health monitoring techniques that can be used to detect damage in structures is vibration analysis. This technique is easy to implement and, at the same time, can provide useful information related to the damage process. Vibration analysis involves extracting the dynamic properties of a structure such as natural frequencies, mode shapes, and damping by measuring the response of a structure, i.e., displacement, velocity, or acceleration to the input force. Vibration analysis of a structure can be divided into three levels, measurements, modal analysis and damage identification.

3.1.1. MEASUREMENTS

Input force and the structural response to this input, i.e. displacement, velocity, or acceleration, are the parameters that should be measured to extract the dynamic properties of a structure. The input force in the experiments reported in this thesis is provided through an excitation applied by a hammer or shocker to the structure. The input force is measured by a load cell attached to these devices. Responses of the structure, i.e., displacement, velocity, or acceleration, are measured using an accelerometer attached to the structure of interest (e.g. the test specimen) or a laser vibrometer fixed far away from the structure.

3.1.2. MODAL ANALYSIS

Modal analysis is a method to extract the frequency response function (FRF) and mode shapes of a structure. To understand the physical meaning of a FRF, consider the general equation of vibration for a structure. Without loss of generality, the damping can be considered in this equation as viscous damping, although it is not the case for composite materials.

$$M\ddot{\bar{U}}(t) + K\bar{U} + C\dot{\bar{U}}(t) = \bar{F}(t) \quad (3.1)$$

Where M , K and C are the mass, stiffness and damping matrices and \bar{U} is the displacement vector. If the structure is divided into n elements then \bar{U} is a vector with n components, M , K and C are $n \times n$ matrices. In the frequency domain, this equation can be written;

$$(-\omega^2 M + K + i\omega C)\bar{\bar{U}}(\omega) = \bar{\bar{F}}(\omega) \quad (3.2)$$

Rearranging this equation;

$$\bar{\bar{U}}(\omega) = (-\omega^2 M + K + i\omega C)^{-1} \bar{\bar{F}}(\omega) \quad (3.3)$$

From this equation, the FRF is defined as;

$$FRF = (-\omega^2 M + K + i\omega C)^{-1} \quad (3.4)$$

As it can be seen the FRF is an $n \times n$ matrix where its elements are dependent on the properties of the structure such as stiffness and damping.

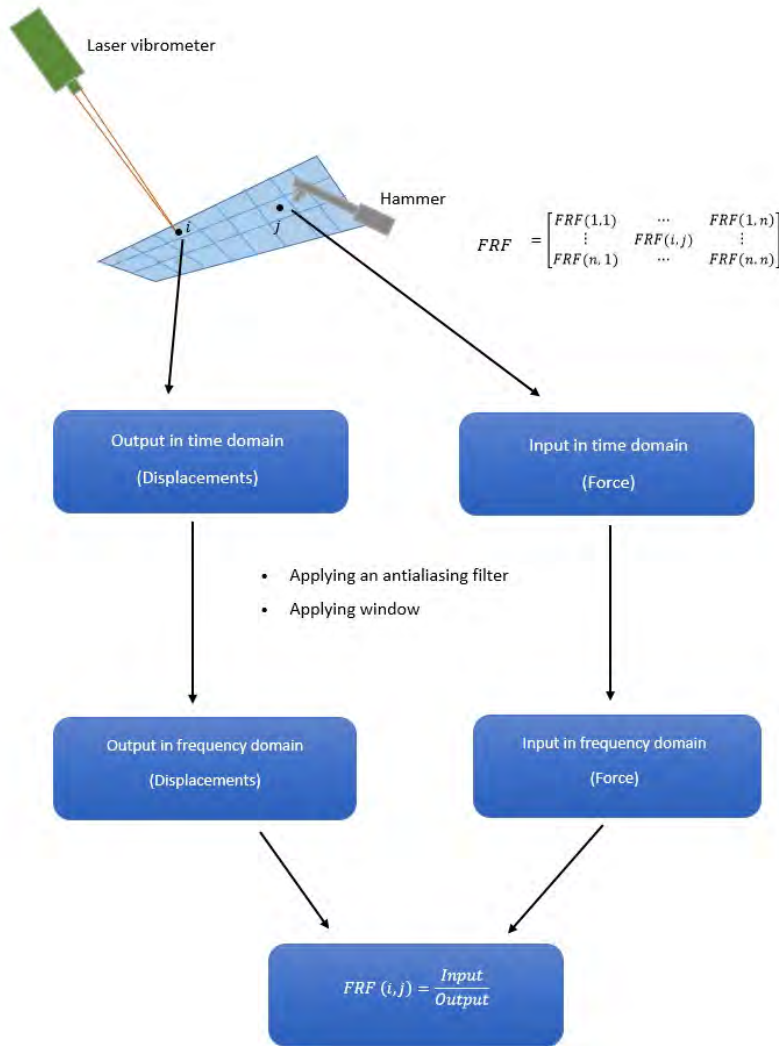


Figure 3.1: Steps required for performing a modal analysis.

The FRF matrix can be determined by measuring the input force and output response of the structure as shown in figure 3.1. For more details, refer to chapter 2 of Avitabile's book [56].

3.1.3. DAMAGE IDENTIFICATION METHODS

Two properties of materials, stiffness, and damping, can be used to diagnose damage in a structure using vibration analysis. Most proposed damaged detec-

tion methods so far are based on the change in stiffness. The change in stiffness affects the dynamic properties of the structure, such as its natural frequencies and mode shapes. The natural frequencies and mode shapes of a structure are derived from its FRF.

Damage reduces the stiffness, which causes a reduction in the natural frequencies of the structure. Moreover, a change in the stiffness affects the mode shape parameters, i.e., curvature and modal strain energy of the structure. Based on these changes, some methods have been proposed to identify and localize the damage in a structure. For more details about different methods, refer to Sohn et.al. [57]. In figure 3.2 the three levels of vibration analysis with some typical damage identification methods are shown.

Unfortunately, damage to composite materials, especially composite joints in a wind turbine blade, do not lead to a significant reduction in stiffness. Therefore, methods based on changes in stiffness cannot reliably be used to detect and diagnose damage. The only parameter that may be useful to characterize damage in a composite material is damping. Damage to a composite material increases the damping. Modal damping can be estimated from the FRF and used as an index for damage detection. Unfortunately, for damage localization based on damping, an effective method has not been proposed as yet.

3.1.4. CHAPTER OVERVIEW

This chapter investigates fatigue damage characterization in a shear web adhesively-bonded connection of a wind turbine blade using vibration analysis. This chapter covers the following topics:

- An historical overview and the latest developments in damage detection using vibration analysis.
- A methodology to characterize damage in test specimens representative of shear web adhesively-bonded connections.
- A new method for localization of damage in the test specimens based on changes in damping.
- Experimental set-up and measurements.
- Results, discussion and conclusion.

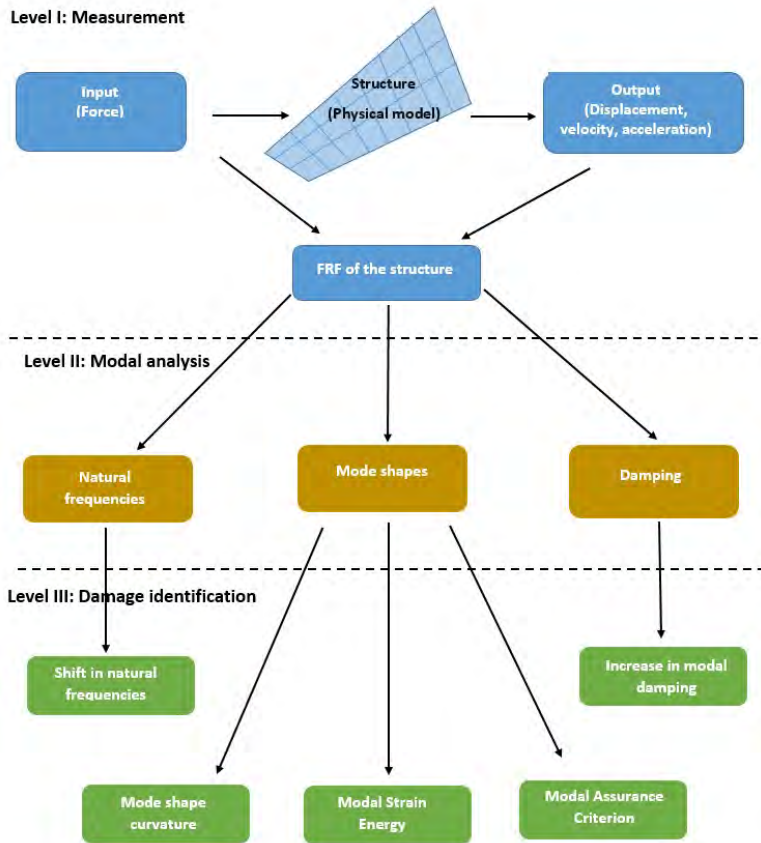


Figure 3.2: A flowchart showing the steps for performing a vibration analysis and typical methods for detection and localization of damage.

3.2. LITERATURE REVIEW

3.2.1. HISTORICAL OVERVIEW

Early studies in vibration-based damage detection date back to the 1970s and early 1980s and focused mainly on the offshore oil industry, [58]. Researchers tried to find damage in an offshore oil platform by observing the change in the natural frequencies of these structures.

Vandiver (1975, 1977) presented a numerical approach to detect damage in an offshore light station tower by examining the change in the frequencies of the first two bending modes and first torsional mode,[59],[60]. He simulated

damage by removing members from the tower and demonstrated that greater than 1% change in natural frequencies could be observed when a member was damaged. He also numerically simulated rust formation by reducing the wall thickness of the structure showing that this led to a reduction in the bending mode frequencies of the tower.

Begg, et al. (1976) showed that severance of members in a scale model offshore structure led to 5% to 30% change in resonant frequencies, [61]. In addition, adding an extra bracing member to a North Sea platform increased the resonant frequency by 10%. Loland and Dodds (1976), Wojnarowski, et al. (1977), Coppolino and Rubin (1980), Duggan, et al. (1980), Kenley and Dodds (1980) used the same methodologies to detect damage in oil offshore platforms [62–66].

Crohas and Lepert (1982) used a “vibro-detection device” mounted on structural members of an offshore oil platform to measure the frequency response function of the member [67]. The device applied an input (excitation) to the member, and then the acceleration response of the member was measured. Flooding of a test brace produced a 10% decrease in the resonant frequency, while the frequencies of neighboring braces were unaffected. Nataraja (1983), Whittome, and Dodds (1983) used the same methodology to detect damage in the North Sea platforms and British Petroleum’s Alpha Forties platform, respectively, [68, 69]. In the case of the North Sea platforms, the results showed that only the lowest natural frequencies could be identified with certainty, and these frequencies were stable throughout the 2 year monitoring period. The authors concluded that changes in natural frequencies is useful for detecting global changes in the structure and not localizing damage. In the case of British Petroleum’s Alpha Forties platform, the results showed less than a 1.5% change in the resonant frequencies over the 2.5 year monitored time. But this change was during the drilling operations and due to added mass on the deck.

In the 1980s and 1990s, there were some attempts to identify cracks in the structures using the change in the natural frequency. The studies of Gudmundson (1982), Ismail et al. (1990), Chowdhury and Ramirez (1992), Fox (1992), and Srinivasan and Kot (1992) reported some of these attempts, [70–74].

In the mid-1980s and 1990s, researchers, among them Pandey et al. (1991), Chance et al. (1994), Stubbs et al. (1995), and Nwosu et al. (1996), tried to localize damage by using the change in mode shape curvatures, [75–78]. Moreover, other researchers such as West (1984), Yuen (1985), Rizos et al. (1990), Osegueda et al. (1992), Fox (1992), Kam and Lee (1992), Mayes (1992), KO, et al. (1994), Lam, et al. (1995) used modal assurance criteria (MAC) to localize the damage in a structure, [73, 79–86].

During the 1980s and 1990s, damage analysis based on changes in stiffness to identify and localize damage became well developed.

3.2.2. IDENTIFICATION AND LOCALIZATION OF DAMAGE BY DAMPING

The methods proposed to date rely mostly on measuring changes in the stiffness of a structure to identify and localize damage. But in a complex structure like a

wind turbine blade, which consists of several structural elements, such as spar caps, trailing and leading edges, etc, changes in the stiffness may not be significant unless severe damage occurs which can compromise the operation of the wind turbine [87]. One property of a composite structure which seems to be more effective than stiffness for early damage detection and its evolution is its damping. Early experimental investigations to identify damage by measuring the damping property of a material were carried out by Modena [88] and Zonta et al [89]. They evaluated the use of modal damping to identify manufacturing defects or structural damage in pre-cast reinforced concrete. In a similar fashion, Kawiecki [90] showed the feasibility of measuring modal damping by using arrays of piezoelectric transducers in a study on two types of concrete blocks. It was found that damping could be a useful property to detect damage in the structure. Keye et al [91] also verified the concept of measuring the change in modal damping as a suitable indicator to identify damage in carbon fibre reinforced polymer (CFRP) materials. Kyriazoglou et al [92] measured the specific damping capacity of woven glass fibre reinforced polymer (GFRP) laminate before and after the introduction of damage using quasi-static loading. The results indicated that measurement of damping could be a promising technique for detection of initial cracks in a woven fabric composite. Zhang et al. [93] studied the effect of fatigue damage on damping of unidirectional GFRP and CFRP laminate. They also found that a change in damping was a useful indicator to detect the formation and growth of micro cracks in these laminates. Kiral et al [94] investigated the effect of impact damage on the damping in a woven GFRP beam-type structure. The results showed changes to the damping ratio to be a more sensitive measure of impact damage than changes in the natural frequency. Birman et al [95] presented an analytical method to estimate the effect of matrix cracks on damping in unidirectional and cross-ply ceramic matrix composites. The results showed that damping considerably increases with growth of the matrix cracks. Cao et al [96] reviewed several studies using changes to damping properties as a way to detect structural damage. They concluded that a number of the studies did demonstrate that changes in damping showed greater sensitivity to damage than changes in the natural frequencies or mode shapes, but that damping-based damage identification is still a research area 'in progress' and is not yet well-established. Kopparthi et al [97] studied the effect of delamination on visco-elastic properties of woven GFRP laminates. They observed that the loss factor increases as a result of the delamination but its change is dependent on the size and the location of the delaminated area. Shen et al [98] also studied the effect of delamination on the visco-elastic properties of plant fibre-reinforced composite. They concluded that delamination can greatly increase the loss factor of this type of composite material. Unlike identification, the localization of damage based on changes in damping is a more complicated challenge. Some researchers have tried to propose a method to localize damage but with limited success. Among these researchers, Keye [91] attempted to localize de-lamination damage in a carbon fibre reinforced polymer (CFRP) structure by measuring changes in its modal damping and the introduction of a modified modal assurance criterion.

Although the concept of change in modal damping as an indicator of damage in CFRP materials was verified, its use regarding damage localization required further work. Montalvao et al.[99] proposed a method to localize damage in a CFRP plate. They combined the change in modal damping factor from a reference state to a damaged state with the modal strain shape to produce a spatial damage index. The significant number of false positive and false negative results were a drawback of this method and further research was suggested to improve the accuracy of the index. Another disadvantage was that this method relies on identifying large number of mode shapes which makes it practically too difficult.

3.3. WIND TURBINE BLADE STRUCTURE

A wind turbine blade consists of aerodynamic shells (the pressure side and suction side) and shear webs which are moulded separately and then bonded together in an assembly process using a structural adhesive. The load carrying parts of the shells (spar caps) are constructed from uni-directional composite laminates such as thick GFRM (glass fibre-reinforced materials)[100, 101].

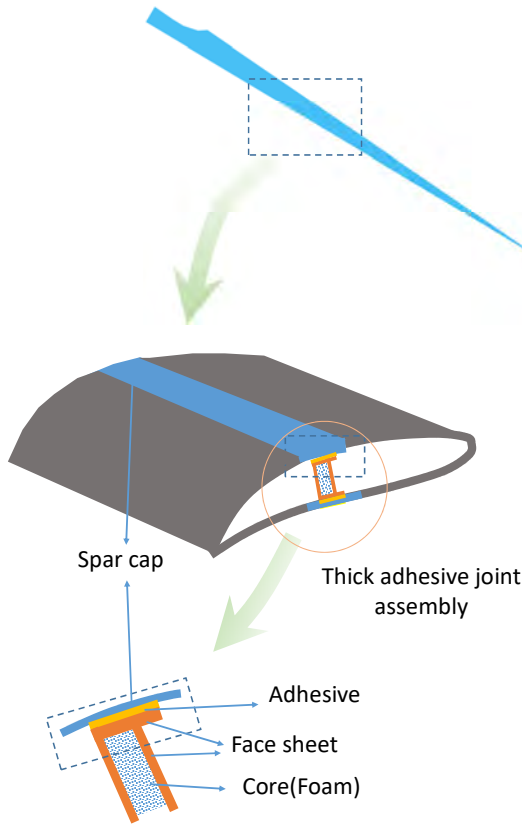


Figure 3.3: Schematic illustration of a spar cap/shear web thick adhesive joint.

Shear webs are built from multi-axial fibre lay-ups and a core of balsa wood or polyvinyl chloride (PVC) foam. The web body is produced by infusion of a balsa/foam core with thin skin laminates, whereas the web foot is primarily made of multi-axial direction glass fibres. The spar-web adhesive joint is manufactured by bonding the web foot onto the spar cap of the blade as shown in Figure 3.3. This web adhesive joint is a key element for the structural integrity of the blade. If the joint suffers fatigue damage at the bond-line then this can propagate through the spar cap and lead to de-lamination and de-bonding of the spar cap from the webs. Early detection of such damage is important for wind turbine maintenance, but such maintenance normally requires visual inspection either from the ground or by climbing the turbine. As damage may not be visible from the outside such methods may not be reliable. Remote measurements based on vibrometry or thermography have the potential to provide more reliable information about blade damage and their use and analysis are thus the motivation for this work.

3.4. TEST SPECIMEN

The selection of test specimen and testing methodology was based on previous work using an asymmetric three-point bending fatigue test of a Henkel beam, representative of a spar to shear web assembly of a wind turbine blade [9]. This bending test indicated that damage progresses on the upper spar face of the beam which is under tension. This test showed that damage began with transverse cracks in the bond-line of the upper spar to shear web of the beam and when the cracks reached the saturation state, damage progressed to de-bonding and final failure of the beam. In the lower spar face of the beam, no damage was observed until instability occurred in the final stage of failure. Moreover the transverse shear stress component was about 10% of the normal tensile stress component. This suggested that a simple fatigue tension test can provide a realistic assessment of incipient damage in a web adhesive joint present in a wind turbine blade. The use of a simple small test specimen to represent the joint has the advantage that manufacturing flaws can be minimised ensuring that results are consistent and accurate.

3.4.1. TEST SPECIMEN PROPERTIES

Several test specimens were manufactured for the experiment. Each test specimen consisted of two skins of unidirectional fibre glass which were made by the infusion of epoxy resin into three layers of unidirectional (UD(0)) fibres. These two skins were then bonded together by a layer of adhesive. The material properties of all components for manufacturing the test specimens are given in Table 4.1 and a schematic illustration of a test specimen is shown in Figure 4.4.

Table 3.1: Mechanical properties of different components for manufacturing of test specimens where: E_Y =Young's Modulus, σ_u =ultimate strength and ρ =volume density.

	Material specification		E_Y (GPa)	σ_u (MPa)	ρ (g/cm ³)
Adhesive	Resin	Epoxy Epikote Resin MGS BPR135G2	5.5	75	1.1-1.2
	Curing agent	Epoxy Epikure Curing Agent MGS BPH1355G			
Adherent	Resin	Epoxy Epikote Resin MGS RIMR135	31-33	400-500	1.3-1.17
	Curing agent	Epoxy Epikure Curing Agent MGS RIMH 137			0.99
	UD fibre glass	Fibre glass non-crimp fabric UD (0), 1210g/m ² , S14EU960			-

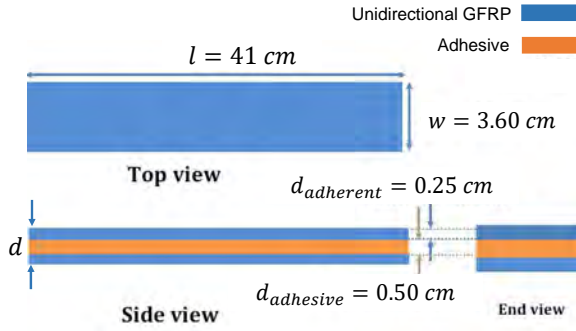


Figure 3.4: Schematic illustration of a test specimen.

3.5. PART A: DAMAGE PROPAGATION AND IDENTIFICATION

The wind turbine blade is fixed in one end and it can represent a cantilever beam-type structure. Therefore test specimen has been fixed in one end, vibrated in bending mode, and has been modeled as a 1D cantilever beam. The viscous-elastic damping model is used to derive the vibration equation. Damping is calculated by fitting the theoretical and experimental frequencies response function (FRF).

3.5.1. METHODOLOGY

Compared to metals, composite materials have generally a higher damping capacity. The main reason for this is the viscous-elasticity of the polymeric matrix [102]. In fibre-reinforced polymers, the dominant damping mechanism is related to the visco-elastic behaviour of the matrix and/or fibre materials. Coulomb friction due to slip in un-bonded regions of the fiber/matrix interface appears to have less influence than viscous-elastic effects. Thermoelastic damping and other mechanisms, such as dislocation damping, are important in metal matrix composites but not in a polymer matrix, [103]. For a linear visco-elastic material, the constitutive equation for a simple one-dimensional stress-strain relationship at time t can be written as [104],

$$\sigma(t) = \int_{-\infty}^t g(t - \tau) d\epsilon(\tau) \quad (3.5)$$

where $\sigma(t)$ is the time-dependent stress, $\epsilon(t)$ is the time-dependent strain, τ is the characteristic relaxation time and $g(t)$ is the relaxation modulus associated with the material properties. The Laplace transform of Eq. 3.19 can be written as,

$$\bar{\sigma}(s) = s\bar{G}(s)\bar{\epsilon}(s) \quad (3.6)$$

where $\bar{\sigma}(s)$, $\bar{G}(s)$ and $\bar{\epsilon}(s)$ are the Laplace transformed components of $\sigma(t)$, $g(t)$ and $\epsilon(t)$, respectively and s is the complex frequency parameter in the Laplace domain. If the strain is assumed to be harmonic with amplitude of ϵ_0 and angular frequency of ω then,

$$\epsilon(t) = \epsilon_0 e^{j\omega t}. \quad (3.7)$$

In the Laplace transformed domain,

$$\bar{\epsilon}(s) = \epsilon_0 \delta(s - j\omega) \quad (3.8)$$

where δ is the Dirac delta function. Using the definition of the inverse Laplace transform,

$$\sigma(t) = \int_{-\infty}^{+\infty} \bar{\sigma}(s) e^{st} ds. \quad (3.9)$$

Substituting Equation 3.6 and Equation 3.8 into Equation 3.9 gives:

$$\sigma(t) = \int_{-\infty}^{+\infty} s \bar{G}(s) \epsilon_0 \delta(s - j\omega) e^{st} ds \quad (3.10)$$

which results in:

$$\sigma(t) = j\omega \bar{G}(\omega) \epsilon_0 e^{j\omega t}. \quad (3.11)$$

This equation relates the stress and strain for a harmonic excitation where the term $j\omega \bar{G}(\omega)$ is the dynamic modulus and is usually expressed as:

$$j\omega \bar{G}(j\omega) = E'(\omega) + jE''(\omega) \quad (3.12)$$

where E' is the storage term and E'' is the loss term. The loss tangent or loss factor represents the damping of the material and is defined as:

$$\tan(\delta(\omega)) = \frac{E''(\omega)}{E'(\omega)}. \quad (3.13)$$

The time domain equation of motion of a linear visco-elastic material for a single element in finite element form can be written as [105]:

$$\mathbf{M}^e \ddot{\mathbf{y}}(t) + g(t) \mathbf{K}^e \mathbf{y}(0) + \int_0^t g(t-\tau) \mathbf{K}^e \frac{d\mathbf{y}(\tau)}{d\tau} d\tau = \mathbf{f}(t) \quad (3.14)$$

where \mathbf{M}^e , \mathbf{K}^e , $\mathbf{y}(t)$ and $\mathbf{f}(t)$ are the mass matrix, stiffness matrix (where the dynamic modulus has been factored out), displacement vector and force vector for a single element, respectively.

For a harmonic load, $\mathbf{f}(t) = \bar{\mathbf{F}}(\omega) e^{j\omega t}$, the response is also harmonic, i.e. $\mathbf{y}(t) = \bar{\mathbf{Y}}(\omega) e^{j\omega t}$, and Eq. 3.14 becomes:

$$-\omega^2 \mathbf{M}^e \bar{\mathbf{Y}}(\omega) + (E'(\omega) + jE''(\omega)) \mathbf{K}^e \bar{\mathbf{Y}}(\omega) = \bar{\mathbf{F}}(\omega) \quad (3.15)$$

where $\bar{\mathbf{F}}(\omega)$ and $\bar{\mathbf{Y}}(\omega)$ are the amplitude of the harmonic load and the displacement, respectively.

Eq. 3.15, can be applied to all elements of a structure and the dynamic response of a structure to a harmonic force can be obtained. The form of the equation for the dynamic response of the whole structure is the same as that for a single element (Eq. 3.15) except that element terms such as M^e , K^e and $\bar{Y}(\omega)$ should be replaced with M , K and Y for the whole structure. In this case, the Frequency Response Function (FRF) for the whole structure is defined as:

$$\mathbf{FRF} = (-\omega^2 \mathbf{M} + (E'(\omega) + jE''(\omega))\mathbf{K})^{-1} \quad (3.16)$$

where M and K are now the global mass and stiffness matrices.

From Eq. 3.16, the analytical response of a structure in the frequency domain can be calculated. In this paper, the GHM (Golla-Hughes-McTavish) parametric form of the dynamic modulus has been used,[105]:

$$E'(\omega) + jE''(\omega) = G^0 \left[1 + a \frac{(s^2 + 2\zeta\bar{\omega}s)}{(s^2 + 2\zeta\bar{\omega}s + \bar{\omega}^2)} \right] \quad (3.17)$$

Where $s = j\omega$ and G^0 , a , ζ and $\bar{\omega}$ are model parameters which are fitted to experimental data.

3.5.2. EXPERIMENTAL SET UP

Three test specimens were subjected to a tension fatigue test using a 100 kN hydraulic fatigue rig under load control as shown in Figure 3.5. Figure 3.5(a) shows the real-life set-up and Figure 3.5(b) shows a schematic representation of the modal test set-up. Before the start of each fatigue test, a modal test was carried out on the healthy test specimen using an automatic hammer to excite the specimen and a laser vibrometer connected to a data acquisition system to record the vibration data. After a specified number of cycles, the fatigue test was halted and a further vibration test was carried out. This was repeated several times to build up a time-line of vibration response during progressive fatigue damage.

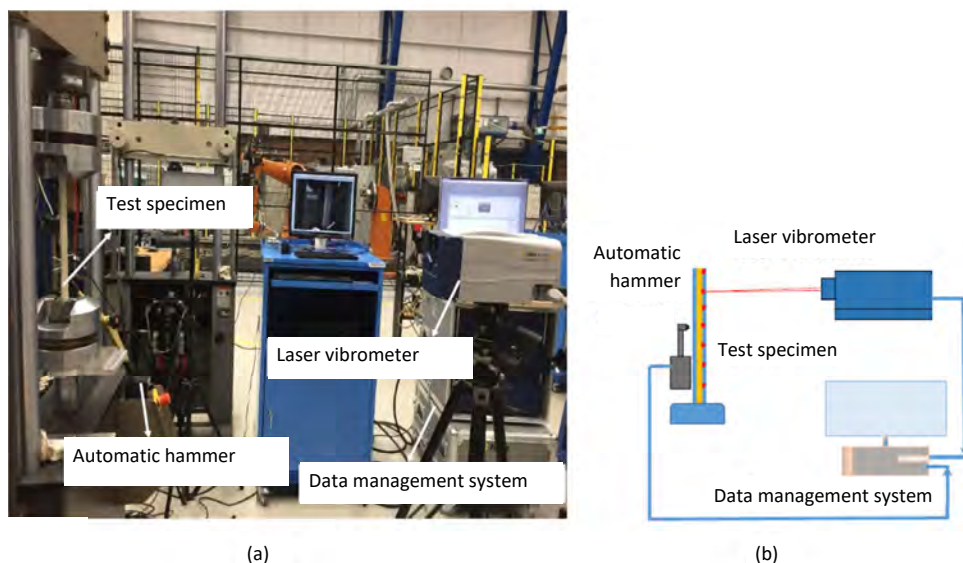


Figure 3.5: (a) Actual and (b) schematic of the experimental test set up to carry out the fatigue and modal tests

The purpose of the modal tests was to determine the experimental FRF of each test specimen. In conjunction with an analytical form of the FRF, it was then possible to determine the stiffness and damping properties of the specimen.

3.5.3. RESULTS AND DISCUSSION

DAMAGE EVOLUTION IN THE ADHESIVE JOINT

Each test specimen was subjected to a fatigue tension test with the stress ratio, R (ratio of minimum load amplitude to maximum load amplitude) equal to 0.1, a fatigue cycling frequency of 3 Hz and a progressive maximum load amplitude as shown in the Figure 3.6. Increasing the load ratio causes the development of fatigue damage propagation at a faster rate. This reduces the required time for the experimental test and the storage space needed for the acoustic data.

This figure shows the progression of damage in one specimen but the trend is same for the other specimens. After around 1.3×10^4 cycles, the first cracks appeared in the adhesive joints.

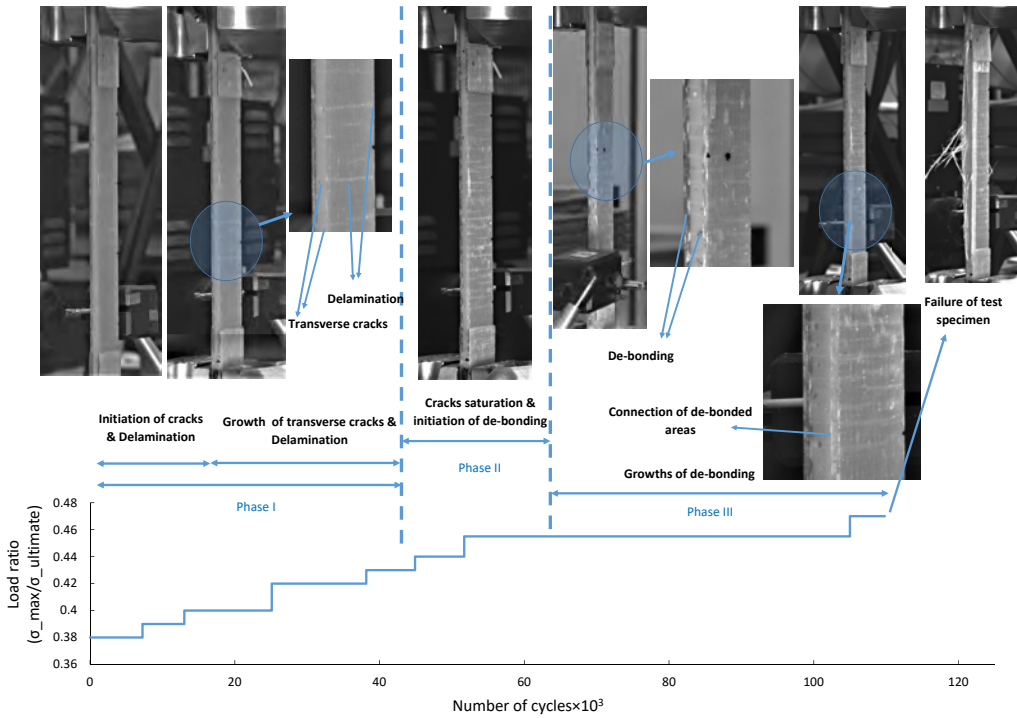


Figure 3.6: Damage progression in one of the test specimens during the tension fatigue test. N.B. On the vertical axis, σ_{\max} and σ_{ultimate} are the maximum stress amplitude of the fatigue test and the ultimate strength of the test specimen, respectively.

As cracks occurred in the adhesive, delamination appeared simultaneously in the vicinity of the crack point in the laminate. This can be considered as the first damage phase (I). As the depth of the cracks through the adhesive increased, so did the area of de-lamination. This trend continued until the cracks reached the saturation phase where the crack density was 66.7 m^{-1} across the length of the test specimen. During the damage saturation phase (II), due to increase in the crack depth and de-lamination area, de-bonding of the adhesive from the face-sheets in the vicinity of some crack points took place. The initially limited number of de-bonded areas increased and became widespread throughout the test specimen. In the final phase of damage (III), these disconnected de-bonded areas became linked together and led to the final failure of the test specimen. The progressive phases of damage as a function of load cycle are shown in Figure 3.6. The crack density versus the number of fatigue cycles during the three different phases of damage for the three test specimens (samples) are shown in Figure 3.7. The three specimens show relatively consistent results with a small amount of spread. After around 6.4×10^4 cycles, the number of cracks stopped increasing but de-bonding continued to increase until the final failure of the test specimen.

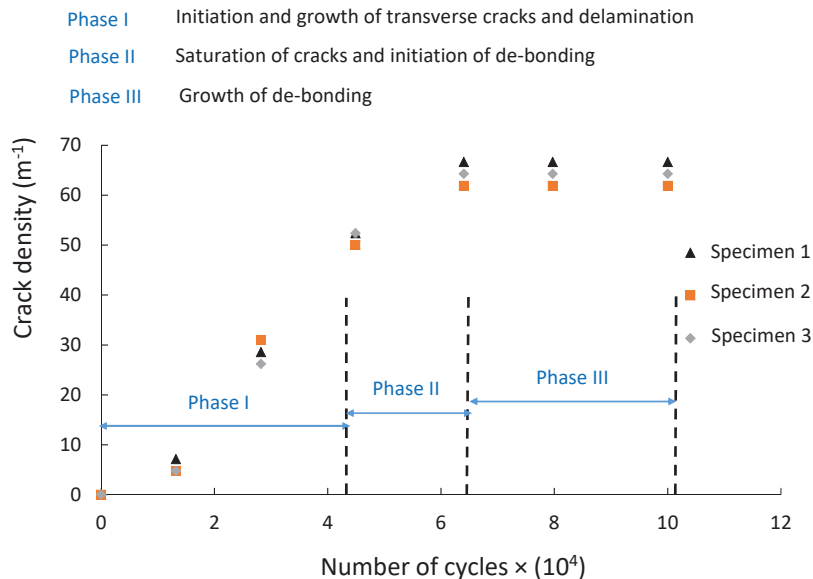


Figure 3.7: Crack density versus fatigue load cycles during the different phases of damage throughout the fatigue test.

STIFFNESS MEASUREMENT

During the different phases of damage, the fatigue test was halted and the stiffness was measured using an extensometer. The results are shown in Figure 3.8. Noticeably, there is more spread in the stiffness values for the three specimens compared to the crack density. In the first phase of damage, which corresponds to the initiation of the transverse cracks, there was no significant change in the stiffness. During the crack saturation phase, an average reduction of 4.7% in the stiffness was observed. The stiffness reduced while de-bonding was initiated and expanded and the test specimen experienced a total average reduction of 8.6% in stiffness before final failure.

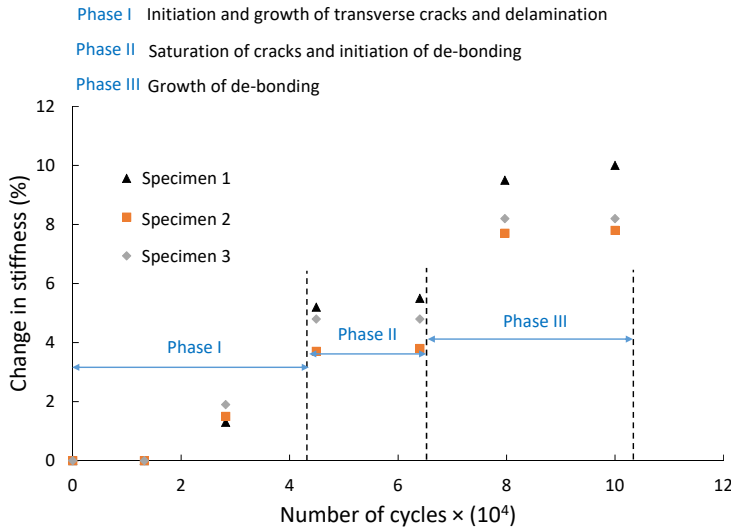


Figure 3.8: Reduction in stiffness versus fatigue load cycles during different phases of damage.

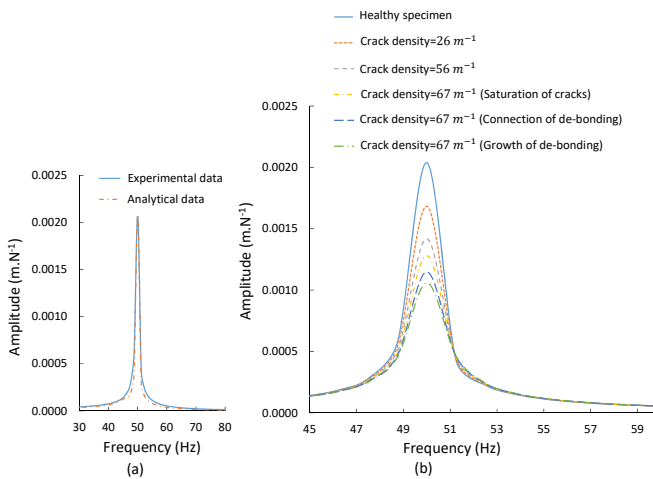


Figure 3.9: (a) Comparison of the theoretical and experimental FRF (b) The best fit FRF to the data in the vicinity of the first natural frequency for different levels of damage.

CALCULATION OF THE LOSS FACTOR

Using Eq. 3.40, a best fit to the experimental data close to the first natural frequency is made of the GHM parametric form of the dynamic modulus by adjusting the model parameters. A comparison between the experimental FRF and theoretical FRF of one specimen is shown in Figure 3.9(a). The best fit FRF for different levels of damage is shown in Figure 3.9(b). The best fit theoretical FRF is then used to calculate the loss factor for different levels of damage as shown in Figure 3.10. The loss factor varies with the frequency with a maximum value near to the first natural frequency. The change in the value of the loss factor close to the first natural frequency for the three distinct phases of damage is shown in Figure 3.11. It can be seen from this figure that in Phase I, as the number of cracks increases, the loss factor also increases. In the crack saturation state (Phase II), although the number of cracks does not change, the loss factor does increase due to growth in de-lamination. The average cumulative change in the loss factor from initiation of cracks until crack saturation is 65.7%. In the third phase of damage, due to the increase in the depth of transverse cracks, the shear stress between the adhesive and the laminate increases leading to de-bonding of the adhesive from the laminate. The disconnected de-bonded areas become linked together and lead to the final failure of the test specimen. This mechanism seems to be the reason for the increase of the loss factor in this third damage region. An average cumulative increase in the loss factor of 111.4 % is estimated before failure of the test specimen.

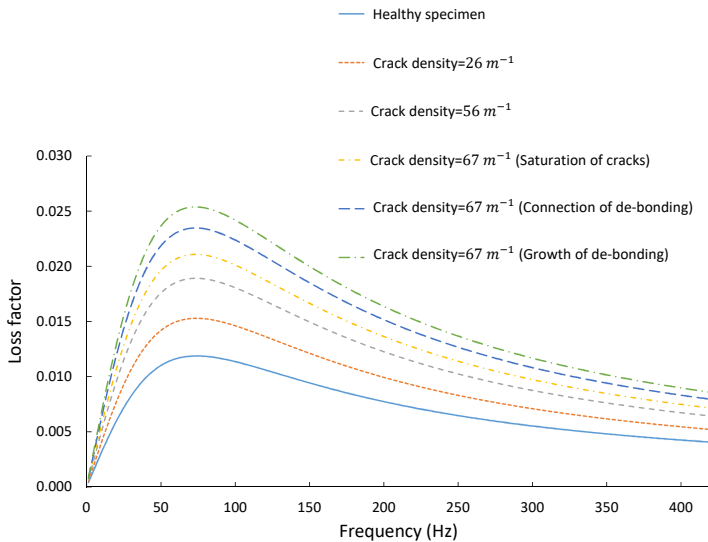


Figure 3.10: Loss factor versus frequency for different levels of damage.

- Phase I Initiation and growth of transverse cracks and delamination
 Phase II Saturation of cracks and initiation of de-bonding
 Phase III Growth of de-bonding

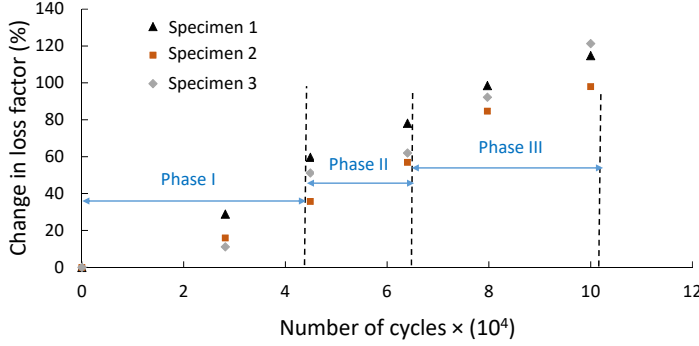


Figure 3.11: Change in loss factor versus fatigue load cycles during the different phases of damage.

3.6. PART B: DAMAGE LOCALIZATION

3.6.1. FINITE ELEMENT VISCO-ELASTIC DAMPING MODEL

The visco-elastic behaviour of a composite material is the dominant mechanism for energy dissipation in such a material when subjected to fatigue. Logically, this type of behaviour should be expected for such as a spar cap-shear web thick adhesive joint in a wind turbine blade. Therefore, to investigate the dynamic behaviour of such a structure, a finite element visco-elastic vibration model is used.

Using a finite element framework, the displacement within each element of a structure is expressed in a Lagrangian context as a function of initial position and time, which can be written as [106]:

$$\vec{U}^e(X, Y, Z, t) = N(X, Y, Z)\vec{q}^e(t) \quad (3.18)$$

In this equation, variables with an arrow over the top denote a vector and variables with a bold letter denote a matrix or tensor. X , Y and Z are the initial position of elements in the structure and $\vec{U}^e(X, Y, Z, t)$ is the displacement vector for each element within the structure. $N(X, Y, Z)$ is the shape function matrix and is dependent on the type of each element. $\vec{q}^e(t)$ is the nodal displacement vector whose initial position $\vec{q}^e(t = 0)$ is known but its change in position with time needs to be calculated.

For a linear visco-elastic material, the constitutive equation for the stress-strain

relationship at time t can be written as: [104, 105]:

$$\sigma(t) = C(t)\epsilon(0) + \int_0^t C(t-\tau)\dot{\epsilon}(\tau)d\tau \quad (3.19)$$

where $(\dot{})$ represents the time derivative operator:

$$(\dot{}) = \partial()/\partial(t) \quad (3.20)$$

τ is the characteristic relaxation time and $C(t)$ is the visco-elastic fourth order tensor of the material properties which due to the symmetry of the stress and strain can be represented in Voigt notation as a 6×6 dimension matrix. The strain $\epsilon(t)$ and stress $\sigma(t)$ are second-order tensors which due to symmetry can also be expressed in Voigt notation as 6×1 vectors [106].

$$\vec{\sigma} = \begin{Bmatrix} \sigma_x \\ \sigma_y \\ \sigma_z \\ \sigma_{xy} \\ \sigma_{yz} \\ \sigma_{xz} \end{Bmatrix}, \quad \vec{\epsilon} = \begin{Bmatrix} \epsilon_x \\ \epsilon_y \\ \epsilon_z \\ \epsilon_{xy} \\ \epsilon_{yz} \\ \epsilon_{xz} \end{Bmatrix} \quad (3.21)$$

In contrast to an elastic material, for a visco-elastic material, $C(t)$ varies with time. The weak form equation of motion for the structure can be derived by applying the principle of virtual work for each element of a structure. This states that for a structure in dynamic equilibrium, the work of the applied forces (including the inertia force) on the structure due to a small deviation, $\delta\vec{U}$, from the equilibrium position is zero. Applying this principle for each element [106], this gives:

$$\int_{V_e} \ddot{\vec{U}}^T \delta\vec{U} \rho dV + \int_{V_e} \vec{\sigma}^T \delta\vec{\epsilon} dV + \int_{V_e} \vec{\tau}^T \delta\vec{U} \rho dV + \int_{V_e} \vec{f}^T \delta\vec{U} \rho dV = 0 \quad (3.22)$$

The first term is work due to inertial forces within the volume of an element, the second term is work due to stresses within an element, the third term is work due to boundary forces over the surface of an element and the last term is work due to gravitational forces within an element. These terms are for a small displacement of a structure $\delta\vec{U}$ from time t to time $t + \delta t$. $\vec{\tau}$ is the boundary force per unit area for an element and \vec{f} is the gravitational force per unit volume of an element. The subscript e indicates that a vector or matrix belongs to an element e of the structure and the superscript T indicates the transpose of a vector or matrix. From Equation 3.18:

$$\delta\vec{U}^e = N\delta\vec{q}^e \quad (3.23)$$

Strain in a structure can be related to the displacement field as:

$$\vec{\epsilon} = D\vec{U} \quad (3.24)$$

where D is the operator matrix which acts on the shape function and its form and components depend on the element type and selected solution. From Equations 3.18 and 3.24:

$$\bar{\epsilon} = DN\bar{q}^e \quad (3.25)$$

$$\delta\bar{\epsilon} = DN\delta\bar{q}^e \quad (3.26)$$

$$\dot{\bar{\epsilon}} = DN\dot{\bar{q}}^e \quad (3.27)$$

The matrix B is then defined as $B = DN$. By substitution of Equations 3.25-3.27 into Equation 3.22 and after some manipulation, the finite element form of the equation of motion for an element of the structure is obtained:

$$M^e \ddot{\bar{q}}^e + \bar{q}^e(0)K^e(t) + \int_0^t K^e(t-\tau)\dot{\bar{q}}^e d\tau = \bar{F}^e \quad (3.28)$$

where the element mass and stiffness matrices and the force vector are defined as:

$$M^e = \int_{V_e} N^T N \rho dV \quad (3.29)$$

$$K^e = \int_{V_e} B^T C(t) B \rho dV \quad (3.30)$$

$$\bar{F}^e = \int_{V_e} N^T \bar{t} ds + \int_{V_e} N^T \bar{f} dV \quad (3.31)$$

Applying the virtual work principle for all elements and then assembling the mass, stiffness and force vector for the whole structure gives:

$$M \ddot{\bar{q}} + \bar{q}(0)K(t) + \int_0^t K(t-\tau)\dot{\bar{q}} d\tau = \bar{F} \quad (3.32)$$

where M , $K(t)$ and \bar{F} are mass and stiffness matrices and force vector for the whole structure, respectively. Equation 3.32 in the Laplace domain can be written as:

$$s^2 M \bar{\bar{q}}(s) + sK(s)\bar{\bar{q}}(s) = \bar{F}(s) \quad (3.33)$$

For a visco-elastic material, the relaxation matrix properties $C(t)$ can be written as the sum of an equilibrium part and a time-dependent part:

$$C(t) = C^0 + h(t) \quad (3.34)$$

where C^0 is the matrix of relaxation properties as $t \rightarrow \infty$.

Substituting Equation 3.34 into Equation 3.30 gives:

$$K^e = \int_{V_e} B^T C^0 B \rho dV + \int_{V_e} B^T h(t) B \rho dV \quad (3.35)$$

By introducing the terms: $K^{0e} = \int_{V_e} B^T C^0 B \rho dV$ and $H^e(t) = \int_{V_e} B^T h(t) B \rho dV$ then:

$$K^e(t) = K^{0e} + H^e(t) \quad (3.36)$$

In the Laplace form:

$$s\bar{K}^e(s) = K^{0e} + s\bar{H}^e(s) \quad (3.37)$$

where $s\bar{K}^e$, K^{0e} and $s\bar{H}^e(s)$ are the dynamic modulus, storage modulus and loss modulus matrix for an element of structure, respectively. By introducing, $\bar{D}^e(s) = s\bar{H}^e(s)$ and substituting equation 3.37 into the Laplace form of Equation 3.28 and then assembling the mass, stiffness and force vector for the whole structure, gives:

$$s^2 M \bar{q}(s) + K^0 \bar{q}(s) + \bar{D}(s) \bar{q}(s) = \bar{F}(s) \quad (3.38)$$

This is the Laplace form of the equation of motion where M is the mass matrix, K^0 is the stiffness matrix and $\bar{D}(s)$ is the damping matrix. This equation is used to extract complex eigenvalues and complex mode shapes as explained in Section 3.14

3.6.2. DAMAGE MODELLING OF A SPAR CAP-SHEAR WEB THICK ADHESIVE JOINT

The thick adhesive joint consists of two skins of unidirectional fibre glass laminate which are bonded together by means of an adhesive. To study the theoretical response of this joint under varying levels of damage, a model of this joint, shown schematically in Figure 3.12, is used. Material properties and dimensions of this joint are given in Table 3.2. E , G , ν and ρ are Young's modulus, shear modulus, Poisson ratio and density. The index x and y are pointed out to the directions in a Cartesian coordinate system as shown in figure 3.12.

For the purposes of the vibration analysis, the adhesive joint is considered as a solid structure consisting of solid type elements and fixed at one end as shown in Figure 3.13 modelled using ANSYS Structural Analysis 18.2 FE software. To ensure convergence, the number of elements in the test specimens was increased until the natural frequencies did not change. This was achieved when the total number of elements in the test specimen was 744 and changes in natural frequency were less than 0.001%.

To identify and localize damage, the mass, stiffness and damping matrix are extracted. These matrices are used as input to a MATLAB code to calculate the complex mode shapes and the phase of the components of the mode shapes.

The damage is introduced within a small section of the modelled adhesive joint by adjusting the parameters of the Young's (shear) modulus which is assumed to be dynamic:

$$E(t) = E^0 + h(t) \quad (3.39)$$

where E^0 is a fixed term (the relaxation modulus) and $h(t)$ is a time-varying term. In the Laplace domain, this equation can be written as:

$$s\bar{E}(s) = E^0 + s\bar{h}(s)E^0 \quad (3.40)$$

where $s\bar{E}(s)$, E^0 , $s\bar{h}(s)E^0$ and $s\bar{h}(s)$ are the dynamic, storage modulus, loss modulus and loss factor of the visco-elastic material, respectively [105]. An expression for the loss factor introduced by McTavish et.al. [105] (also known as the Golla-Hughes-McTavish or GHM model) is given by:

$$s\bar{h}(s) = a \frac{s(s + 2\zeta\bar{\omega})}{(s^2 + 2\zeta\bar{\omega}s + \bar{\omega}^2)} \quad (3.41)$$

where a , ζ and $\bar{\omega}$ are model parameters. Equation 3.40 can also be written as:

$$s\bar{E}(s) = E^0 + \eta(s)E^0 \quad (3.42)$$

Where $\eta(s)$ is the material loss factor. The loss factor is dependent on the frequency and can be identified by experimental modal analysis. Fatigue damage in a spar cap-shear web thick adhesive joint usually manifests as the progression of transverse cracks in the adhesive which lead to de-lamination and de-bonding of the adhesive from the laminate [107].

In the section 3.5 of this chapter, a fatigue tension test on the same type of adhesive joint modelled in this paper, was conducted and the loss factor for a healthy joint was determined by use of modal analysis using the GHM formulation for a range of frequencies. These values are used in this present study for the undamaged section of the joint structure. For the damaged section, the damage intensity level (DIL) is defined as:

$$DIL = \frac{\eta_d}{\eta} \quad (3.43)$$

where η_d is the loss factor for the damaged section. The data in table 3.2 are used for the storage modulus. The loss modulus is calculated by multiplying the loss factor by the storage modulus. Using these values as input to ANSYS Structural Analysis 18.2 FE software, the mass matrix M , stiffness matrix K^0 and damping matrix $\bar{D}(s)$ from equation 3.38 at range of frequencies were extracted.

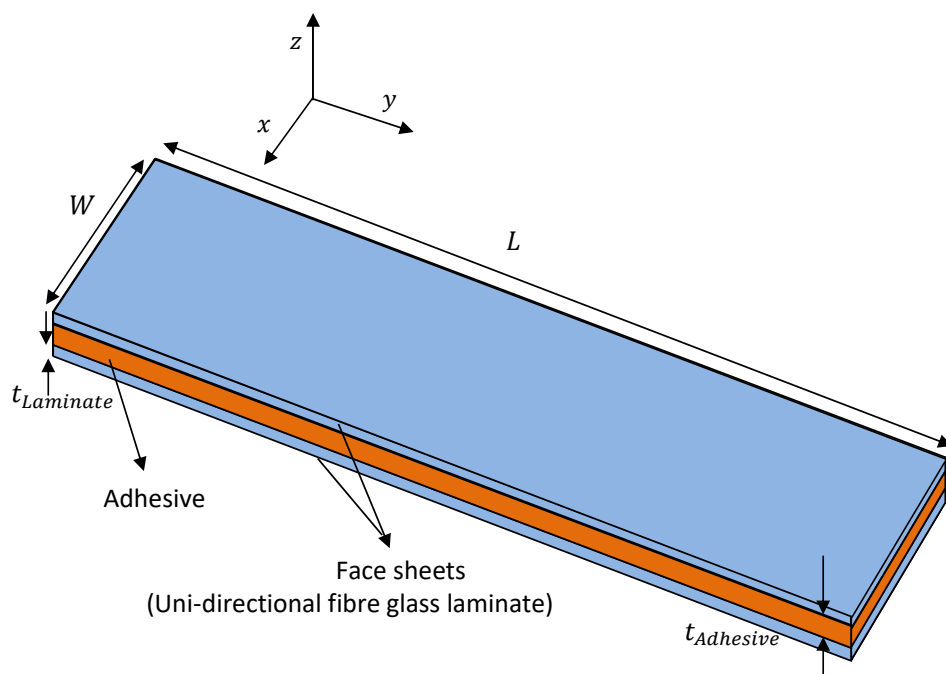


Figure 3.12: Schematic illustration of the spar cap-shear web thick adhesive joint modelled in this study

Table 3.2: Material properties and dimensions of the thick adhesive joint modelled in this study

Parts	Material specification		E_Y (Gpa)	E_x (Gpa)	G_{x-y} (Gpa)	ν_{xy}	ν_{yz}	ρ (g/cm ³)	L/W/t (cm)
Adhesive	Resin	Epoxy Epikote Resin MGSBPR135G2	5.2	5.2	2.03	0.35	0.35	1.1	37.5/4/0.5
	Curing agent	Epoxy Epikure Curing Agent MGS BPH1355G							
Face sheets	Uni-directional fibre glass laminate		31.5	5	3.8	0.4	0.3	1.6	37.5/3.6/0.25

3.6.3. DAMAGE IDENTIFICATION AND LOCALIZATION

The approach proposed in this work for damage localization is based on the premise that damage in a certain part of a composite structure leads to a substantial localized increase in damping (non-proportionality). This local damage creates non-proportionality in the energy dissipation throughout the structure. This means that in the damaged area, the dissipation of energy due to damp-

ing is greater compared with the case when there is no damage. This non-proportionality in energy dissipation affects the phase of the characteristic mode shapes of the structure. If the adhesive joint is considered as a number of solid elements supported at one end as shown in Figure 3.13, then the k^{th} eigenvector (mode shape) of the structure can be written as:

$$\bar{\phi}^{(k)} = \begin{Bmatrix} \phi_1^{(k)} \\ \dots \\ \phi_i^{(k)} \\ \dots \\ \phi_n^{(k)} \end{Bmatrix}, \quad (3.44)$$

where $\phi_i^{(k)}$ ($i = 1, 2, \dots, n$) are the components or structural element displacements of each mode shape k . The components of the eigenvector are complex and can be written as:

$$\phi_i^{(k)} = \|\phi_i^{(k)}\| e^{j\partial_i^{(k)}}, \quad i=1,2,\dots,n \quad (3.45)$$

where $\|\phi_i^{(k)}\|$ is the magnitude and $\partial_i^{(k)}$ is the phase of the i^{th} component of the k^{th} eigenvector and $j = \sqrt{-1}$.

When there is no damage, the dissipation of energy is proportional throughout the structure and the phases of the components of each eigenvector are zero ($\partial_i^{(k)} = 0$, $i = 1, 2, \dots, n$), [108]. When there is damage in a certain part of the structure, this results in phase differences between the components of the eigenvector especially for those nodes close to the area of damage.

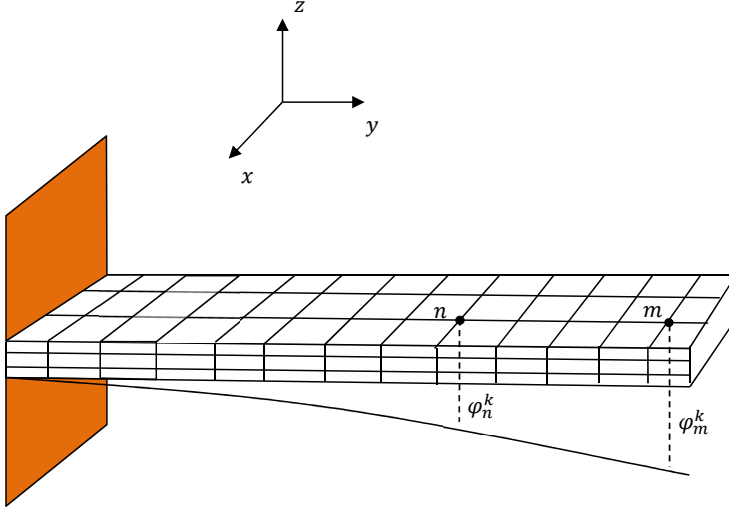


Figure 3.13: Schematic illustration of the thick adhesive joint in first bending mode

To localize damage, the phases of the complex mode shapes (ϑ) are calculated. When local damage occurs in a structure, the damping matrix is non-proportional and the eigenvectors are complex. The method used here to calculate the complex eigenvectors is based on expressing each complex mode shape (complex eigenvector) as a linear combination of normal modes and then using a Neumann expansion method to find the vector coefficients.

To identify damage, modal damping is calculated and an increase in modal damping is taken as an indication of damage in the structure. The complex natural frequency of mode k , as denoted by \hat{n}_k , can be written:

$$\hat{n}_k = -R_k + jI_k \quad (3.46)$$

Where R_k is the real part and I_k is the imaginary part of complex natural frequency for the k^{th} mode. The complex natural frequency \hat{n}_k is related to the eigenvalue, s_k :

$$\hat{n}_k = js_k \quad (3.47)$$

The magnitude of the complex natural frequency and the modal damping are denoted by ω_k and ζ_k , respectively, and are determined using [109]:

$$\omega_k = \sqrt{R_k^2 + I_k^2} \quad (3.48)$$

$$\zeta_k = -I_k / \omega_k \quad (3.49)$$

Substituting Equation 3.49 and 3.48 into Equation 3.46 gives an expression for the complex natural frequency:

$$\hat{n}_k = \omega_k(\sqrt{1 - \zeta_k^2} - j\zeta_k) \quad (3.50)$$

3.6.4. CALCULATION OF COMPLEX EIGENVALUES AND EIGENVECTORS

For a non-proportional damped system with n degrees of freedom, each mode shape of this system is a linear vector composition of n un-damped mode shapes[110]:

$$\bar{\phi}^{(k)} = \sum_{i=1}^n a_i^{(k)} \bar{b}^{(i)} \quad (3.51)$$

where $\bar{\phi}^{(k)}$ is the eigenvector of the k^{th} mode of the non-proportional damped structure, $\bar{b}^{(i)}$ is the eigenvector of the i^{th} mode of the un-damped structure and $a_i^{(k)}$ is a constant. To calculate the coefficients of Equation 3.51, this equation can be substituted into Equation 3.38, with $F(s) = 0$, [111]. The left hand side of this equation is then multiplied by the transpose of the m^{th} mode shape, $(\bar{b}^{(m)})^T$, and using the orthogonal properties of the un-damped mode shapes:

$$a_m^{(k)} s_k^2 + a_m^{(k)} \omega_k^2 + a_k^{(k)} K_{mk} + a_m^{(k)} K_{mm} + \sum_{i=1, i \neq k, i \neq m}^n a_i^{(k)} K_{mi} = 0 \quad (3.52)$$

where

$$K_{mi} = (\bar{b}^{(m)})^T \bar{D}(s = s_k) \bar{b}^{(i)} \quad (3.53)$$

Without loss of generality, $a_k^{(k)}$ is considered equal to 1 and equation 3.52 can be rewritten as:

$$a_m^{(k)} \left(\frac{s_k^2 + \omega_m^2 + K_{mm}}{-1} \right) - \sum_{i=1, i \neq k, i \neq m}^n a_i^{(k)} K_{mi} = K_{mk} \quad (3.54)$$

In matrix form, this equation can be written as (see [111]):

$$[P_k - Q_k]A_k = B_k \quad (3.55)$$

where

$$P_k = \begin{bmatrix} \frac{s_k^2 + K_{11} + \omega_k^2}{-1} & 0 & \dots & (k^{th} \text{ term deleted}) & 0 & 0 \\ 0 & \frac{s_k^2 + K_{22} + \omega_k^2}{-1} & 0 & & \dots & 0 \\ \dots & \dots & \dots & & \dots & \dots \\ (k^{th} \text{ term deleted}) & & & (k^{th} \text{ term deleted}) & & (k^{th} \text{ term deleted}) \\ 0 & 0 & 0 & & \dots & 0 \\ 0 & 0 & 0 & (k^{th} \text{ term deleted}) & \dots & \frac{s_k^2 + K_{nn} + \omega_k^2}{-1} \end{bmatrix} \quad (3.56)$$

$$Q_k = \begin{bmatrix} 0 & K_{12} & \dots & (k^{th} \text{ term deleted}) & \dots & K_{1n} \\ K_{21} & 0 & \dots & & & \\ \dots & \dots & \dots & & & \\ (k^{th} \text{ term deleted}) & & & (k^{th} \text{ term deleted}) & \dots & (k^{th} \text{ term deleted}) \\ \dots & \dots & \dots & & & \\ K_{1n} & K_{2n} & \dots & (k^{th} \text{ term deleted}) & \dots & 0 \end{bmatrix} \quad (3.57)$$

$$A_k = \begin{bmatrix} a_1^{(k)} \\ a_2^{(k)} \\ \dots \\ (k^{th} \text{ term deleted}) \\ \dots \\ a_n^{(k)} \end{bmatrix}, B_k = \begin{bmatrix} K_{1k} \\ K_{2k} \\ \dots \\ (k^{th} \text{ term deleted}) \\ \dots \\ K_{nk} \end{bmatrix} \quad (3.58)$$

The k^{th} row and column of the matrices correspond to the coefficients $a_k^{(k)}$ which are assumed to be known ($a_k^{(k)}=1$), so are removed to give a solution for coefficients other than $a_k^{(k)}$.

Using the Neumann expansion method, the coefficients matrix for k^{th} mode shape can be written as:

$$A_k = [I_{N-1} + R_k + R_k^2 + R_k^3 + \dots]A_0 \quad (3.59)$$

where,

$$R_k = P_k^{-1} Q_k \quad (3.60)$$

$$A_0 = P_k^{-1} B_k \quad (3.61)$$

To solve the matrix form of Equation 3.55, an initial guess is made for the k^{th} eigenvalue, for example, by setting $m = k$ in Equation 3.52. Knowing that $a_k^k = 1$, then this equation can be rewritten as:

$$s_k^2 + \partial_k + \omega_k^2 = 0 \quad (3.62)$$

where:

$$\partial_k = K_{kk} + (B_j)^T A_j \quad (3.63)$$

Then,

$$s_k = -\partial_k + i \sqrt{4\omega_k^2 - \partial_k^2} \quad (3.64)$$

For the first guess, the term $(B_j)^T A_j$ is neglected. The algorithm used to find the complex mode shapes is summarized in Figure 3.14.

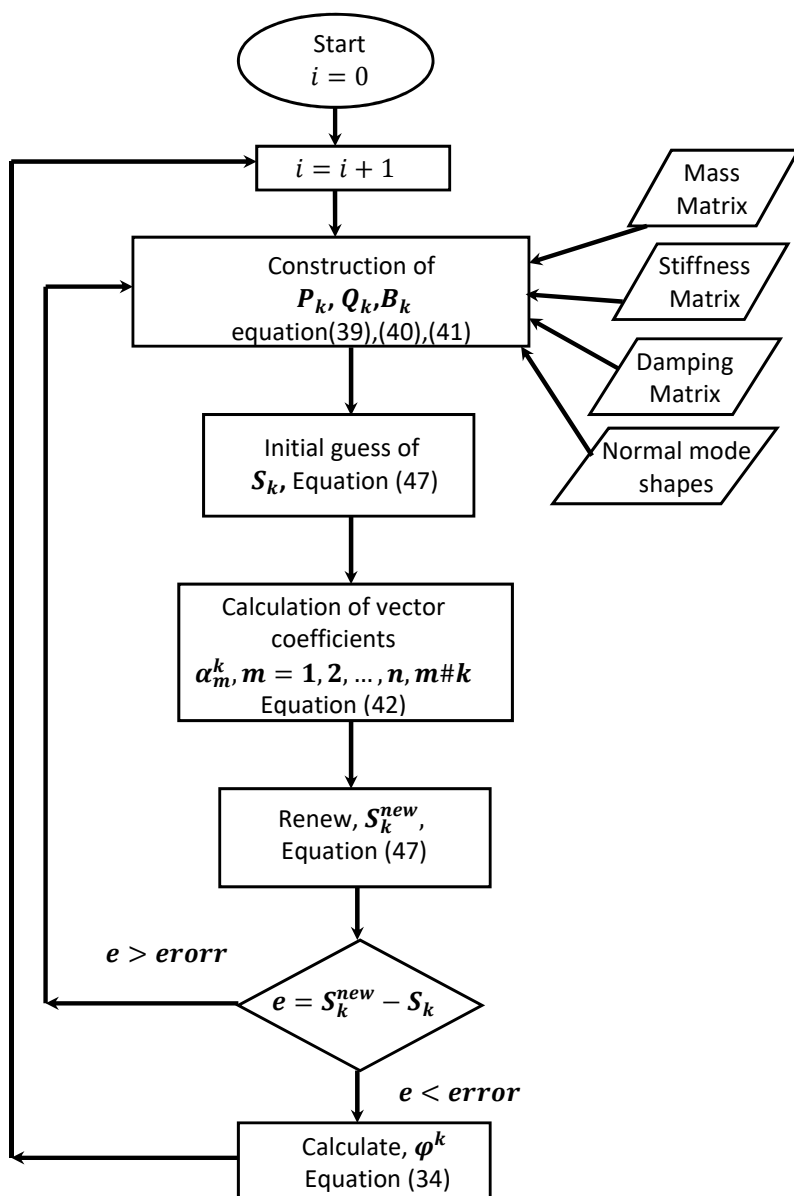


Figure 3.14: Algorithm for calculation of complex mode shapes

3.6.5. RESULTS

Damage was simulated by varying the material loss factor in four different locations of the thick adhesive joint. Then the effect of damage on the phase angle of motion of the structural elements was investigated for different mode shapes. The four locations were at 2.5%, 10%, 20% and 40% of the length of the joint from the fixed end, denoted as Damage Cases 1-4, respectively. Damage intensity levels (DILs) were identified by the ratio of the loss factor of the damaged area (η_d) to the loss factor of the healthy area (η), i.e., η_d/η . Each face sheet and adhesive bond line of the adhesive joint were divided into 244 solid elements (in total 744 elements) of which 12 elements in each face sheet and adhesive bond line (in total 36) were considered as damaged elements.

EFFECT OF DAMAGE LOCATION ON THE PHASE OF MODE SHAPES

The effect of damage on the phase angle of motion of the structural elements of the first mode shapes for Damage Case 1 was determined and the results are shown in Figure 3.15. The results show that, from the fixed end, the phase angle increases close to the area of damage to a maximum positive value just before this area and then rapidly decreases through the damaged area reaching a minimum just beyond and then tending to a value close to zero near the free end. The maximum amplitude of the phase angle change increases with level of damage giving a value of 1.55° for DIL=9.

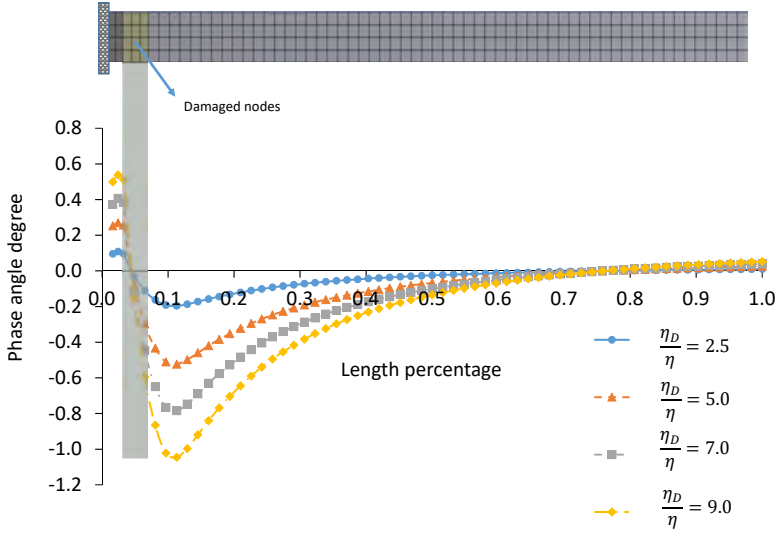


Figure 3.15: Phase angle of the nodal components of the first bending mode for Damage Case 1. The damaged area is shown by the shaded region. The specimen is fixed on the left hand side.

The effect of local damage on the modal damping of the whole specimen is shown in Figure 3.16. The change in modal damping varies from 22.3% for $DIL=2.5$ to 110% for $DIL=9$.

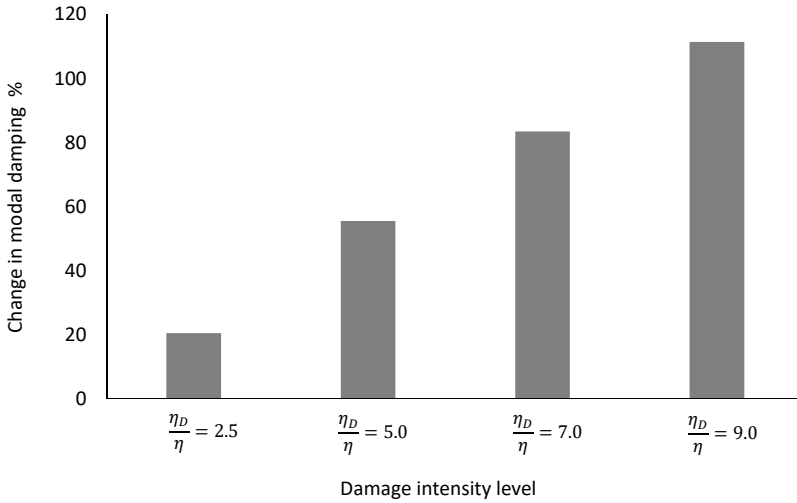


Figure 3.16: Variation of modal damping for Damage Case 1 for different DILs.

The effect of damage on the phase angle of motion of the structural elements for the first mode shape for Damage Case 2 for different DILs is shown in Figure 3.17. The pattern of variation in the phase angle is similar to Damage Case 1, with the maximum peak shifted further away from the fixed end close to the area of damage. The maximum difference in phase for the same DIL=9 is reduced significantly from 1.5° in Damage Case 1 to 0.55° in this case. For this DIL, the change in modal damping also reduces from 110% in Damage Case 1 to 88% relative to an undamaged specimen as shown in Figure 3.18.

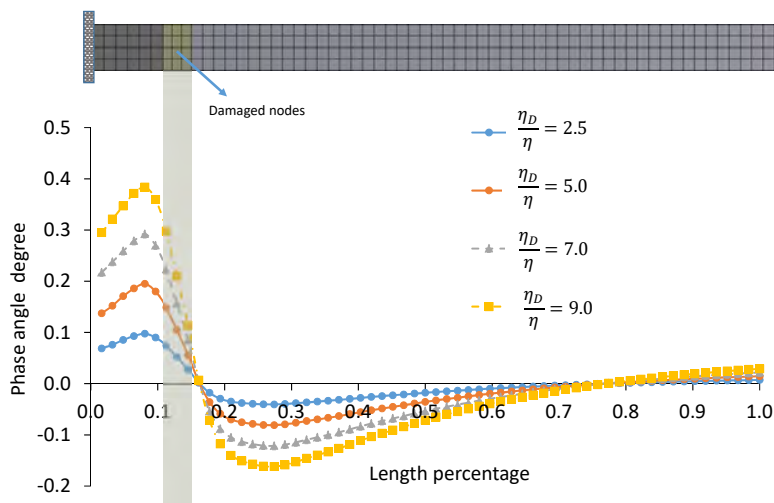


Figure 3.17: As figure 3.15 but for Damage Case 2.

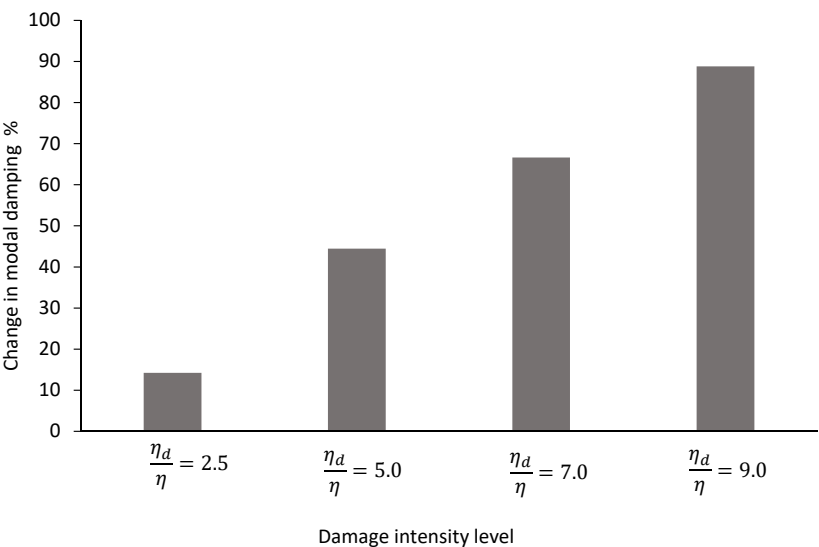


Figure 3.18: Variation of the modal damping for Damage Case 2 at different DILs.

To better localize damage, the spatial derivative of the phase angle for the first bending mode for DIL=9 is calculated and the results shown in Figure 3.19. It can be seen that the derivative becomes increasingly negative around the damaged elements reaching a minimum value within the area of damage. The results for other DILs are not shown but show a similar pattern.

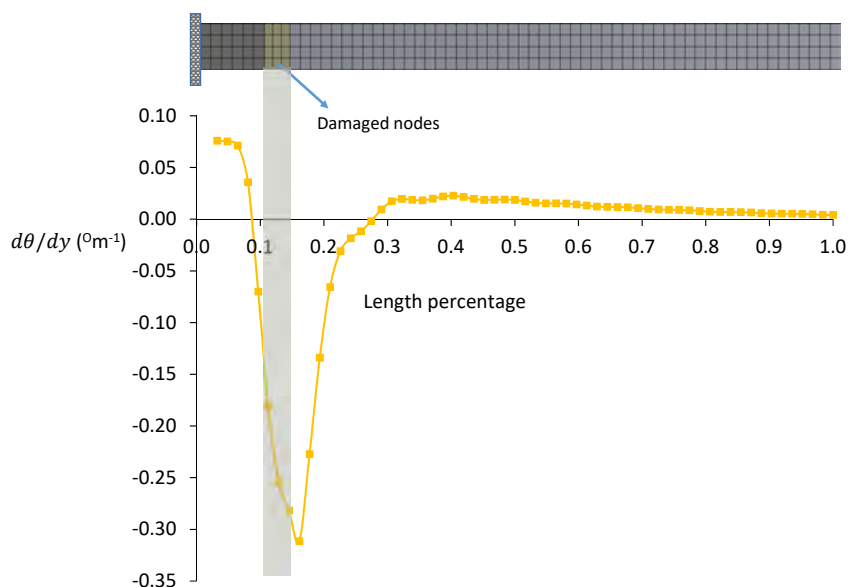


Figure 3.19: Derivative of the phase angle at different nodal components for the first bending mode at DIL=9.

For all four damage cases, the nodal phase angles are plotted for DIL=9 in Figure 3.20.

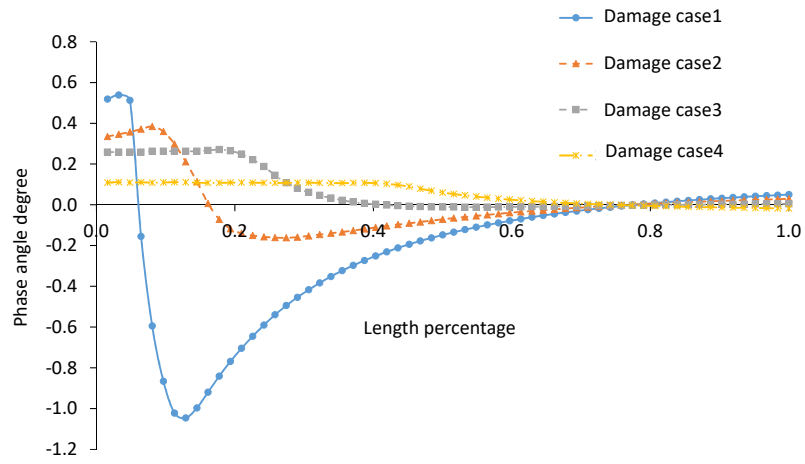


Figure 3.20: Phase angle of the nodal components for the first bending mode for different damage locations for DIL=9.

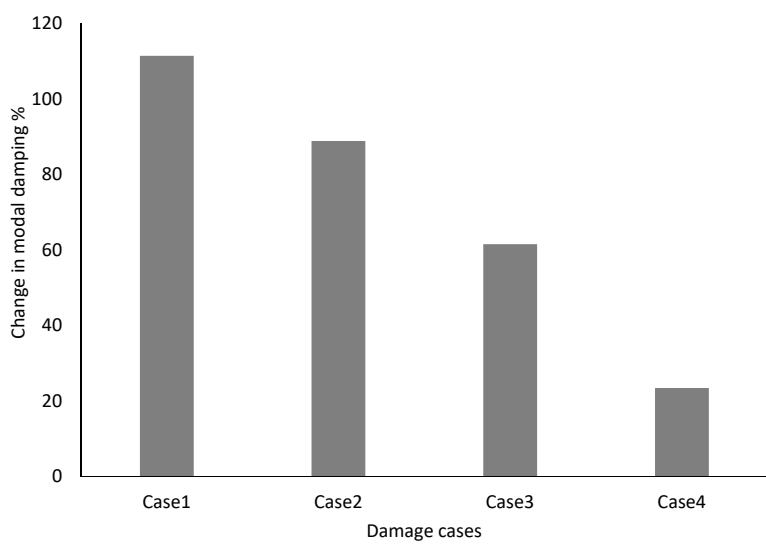


Figure 3.21: Modal damping of the first bending mode for the different damage cases and a DIL $\eta_d/\eta=9$

The magnitude of the phase angle change reduces significantly as the damaged section moves away from the fixed end. This is logical for the first mode shape as local strains progressively reduce moving away from the fixed end and therefore the dissipation of energy is less. This effect can also be observed when analysing the modal damping of the specimen for the four damage cases as shown in Figure 3.21 where the change in modal damping reduces from 110% in Damage Case 1 to 19.8% in Damage Case 4.

EFFECT OF DAMAGE ON DIFFERENT MODE SHAPES

The effect of damage on the phase angle of motion of the structural elements for the third bending mode for Damage Case 4 for different DILs is shown in Figure 3.22 for part of the specimen. The third bending mode shape has a node (the point on the structure without any movement) at structural element 32 as shown in the inset to Figure 3.22. The damaged area in this case is located far from the fixed end and closer to the structural element where the levels of strain are relatively high. This leads to higher local levels of energy dissipation and a larger change in the phase angle close to the area of damage compared to the first bending mode. For DIL=9, the maximum change in phase angle is now around 0.4° compared with only 0.1° for the first bending mode.

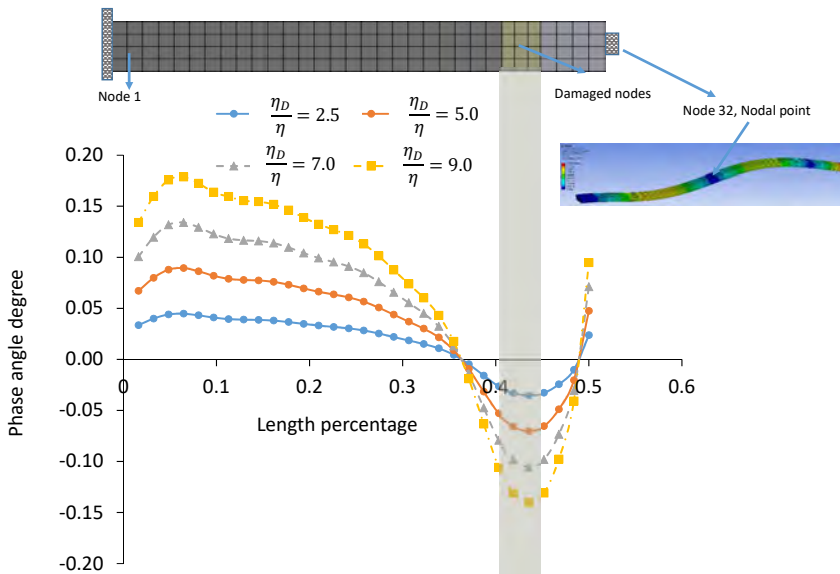


Figure 3.22: Nodal phase angles of the third bending mode for Damage Case 4 for different DILs.

The modal damping of the specimen for the third bending mode for Damage Case 4 at different DILs is shown in Figure 3.23. It can be seen that at DIL $\eta_d/\eta=9$,

the increase in modal damping is about 25% which is higher compared with the first bending mode (19.8%). The spatial derivative of the phase angle for the third bending mode is shown in Figure 3.24. This is shown for DIL $\eta_d/\eta=9$ but similar results are seen for other DIL values. It can be seen from Figure 3.24 that the location of the damage is where the derivative of the phase angle shows a minimum. It seems that derivatives of nodal phase angle is a useful parameter to localize damage although the large value near the structure node could be misleading due to overestimating of this value near to the structure node.

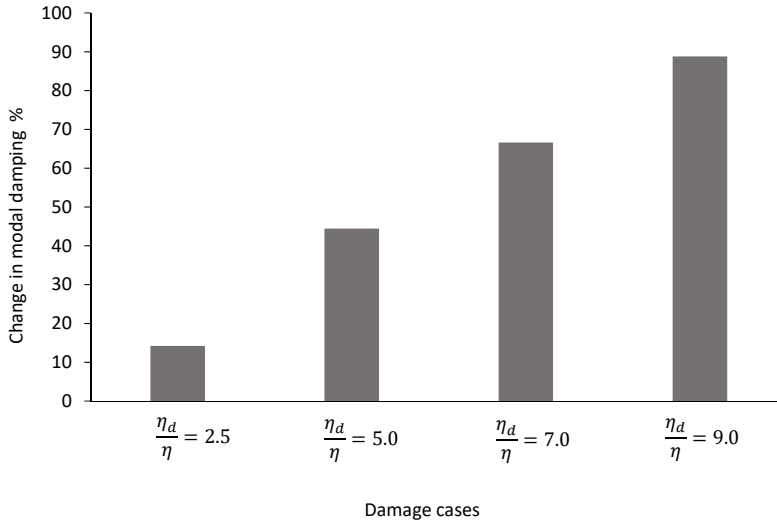


Figure 3.23: Variation in modal damping for the third bending mode for Damage Case 4 and different DILs.

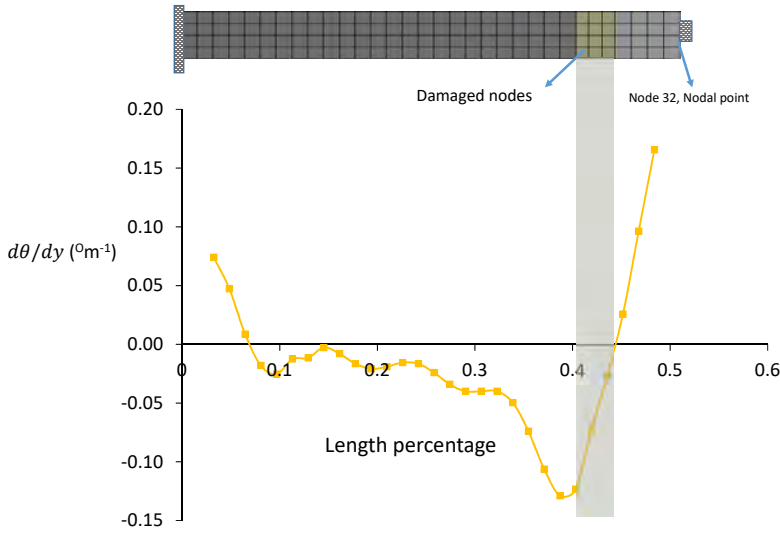


Figure 3.24: Derivative of the phase angle at different nodal components for the first bending mode at $DIL \eta_d/\eta=9$.

SENSITIVITY TO THE SIZE OF THE DAMAGED AREA

To look at the effect of the size of the damaged area on the maximum change in the phase angle of the mode shape, three different areas of damage for Damage Case 1 with $DIL=9$ were considered. For a damaged area equal to 4% of the total area of the test specimen, the maximum change in the phase angle of the first bending mode was 1.58° . For damaged areas equal to 2.6% and 1.3% of the total area of the test specimen, the maximum changes in the phase angle of the first bending mode were equal to 0.975° and 0.371° , respectively. The ability to measure such changes in phase angle in a real specimen is difficult to determine, but this analysis at least gives an indication of the size of change that would be expected.

EFFECT OF DAMAGE ON RESONANT FREQUENCY AND MODE SHAPE

The change in material stiffness is small during damage progression compared with damping. Therefore, the stiffness of the damaged sections was considered unchanged in this model, and only damping assumed to have increased. This means that the natural frequencies for all damaged cases are the same and there is a negligible change in resonant frequencies due to damping. The first mode resonant frequency for the healthy specimen is 49.272 Hz, and in Damage Case 1 with $DIL=9$, the resonant frequency is 49.321 Hz. The mode shapes are effectively the same, with very small changes around the damaged region that cannot be distinguished by Modal Assurance Criterion (MAC) values.

The phase angle of the mode shape changes for the worst case scenario (Damage Case 1 and DIL=9) from 0.539 degrees to –1.05 degrees, with cosine values of 0.99995 and 0.99983 respectively, which gives a MAC value very close to 1 (0.9999996).

3.6.6. DISCUSSION

From the modal analysis, the time-dependent displacement of the structure is determined. This time-displacement response is then used to determine the frequency response function (FRF) of the structure. In this section, it is shown that the phase of the diagonal components of the FRF is related to the phase at the locations of the structural elements for a given mode shape which can be used as an alternative method to localize damage. This is a potentially more useful method as the FRF can be estimated firstly using modal analysis and then the phase angle of the motion of the structural elements for a given mode shape can be extracted.

The FRF has n degrees of freedom and is a $n \times n$ matrix. Each component of the FRF has a magnitude and phase which are dependent on the frequency. The phase of the FRF at the resonant frequency for a specific excitation mode in a healthy structure is 90° as the damping is almost proportional throughout the entire structure. When local damage occurs in the structure, the damping is no longer proportional, the mode shapes become complex and the phases of motion of the structural elements of the FRF at resonant frequency are no longer 90° .

The damping matrix in a viscoelastic damping model of the structure is dependent on the frequency (see Equation 3.38). Because we are interested in the response of the structure in a narrow band around the resonant frequency, the damping matrix can be considered constant in this narrow band and equal to its value at the resonant frequency. With this assumption, the diagonal components of the FRF at the k^{th} resonant frequency ($\omega_{k,res}$) can be written as [108]:

$$FRF_{i,i}(\omega = \omega_{k,res}) = \frac{\phi_i^{(k)} \phi_i^{(k)}}{m_k(\hat{\eta}_k^2 - (\omega_{k,res})^2)} + \sum_{q=1, q \neq k}^n \frac{\phi_i^{(q)} \phi_i^{(q)}}{m_q(\hat{\eta}_q^2 - (\omega_{k,res})^2)} \quad (3.65)$$

Where $\phi_i^{(k)}$ is the i^{th} component of the k^{th} complex displacement mode shape and $\omega_r^{(k)}$ is the k^{th} resonant frequency. The index q refers to the different displacement mode shapes, other than the k^{th} mode shape. The modal mass of the k^{th} mode shape is defined as:

$$m_k = (\bar{\phi}^{(k)})^T M \bar{\phi}^{(k)} \quad (3.66)$$

The resonant frequency $\omega_{k,res}$ is the frequency of the structure where the amplitude of the FRF components are greatest. From Equation 3.65, this maximum amplitude occurs when the denominator is minimised. This occurs when the k^{th} resonant frequency is equal to:

$$\omega_{k,res} = \omega_k \sqrt{1 - 2\zeta_k^2} \quad (3.67)$$

The FRF at the k^{th} resonant frequency, to a good approximation, can be estimated by neglecting the effect of the second term in Equation 3.65 [108]. Neglecting the second term and substituting Equation 3.45 and 3.67 into Equation 3.65 then:

$$FRF_{i,i}(\omega = \omega_{k,res}) = \frac{\|\phi_i^{(k)}\|^2 e^{2j\theta_i^{(k)}}}{j(2m_k \omega_k^2 \zeta_k \sqrt{1 - \zeta^2})} \quad (3.68)$$

The phase of the diagonal components of the FRF at the k^{th} resonant frequency can be written as:

$$Arg(FRF_{i,i}(\omega = \omega_{k,res})) = Arg(\|\phi_i^{(k)}\|^2 e^{2j\theta_i^{(k)}}) - Arg(j(2\omega_k^2 \zeta_k \sqrt{1 - \zeta^2})) - Arg(m_k) \quad (3.69)$$

The phase of the first term in Equation 3.69 is equal to $2\theta_i^{(k)}$ and the phase of the second term is equal to 90° . For simplicity, $Arg(FRF_{i,i}(\omega = \omega_{k,res}))$ is replaced by $\beta_{i,i}^{(k)}$ and then Equation 3.69 can be written as (assuming all angles in degrees):

$$\beta_{i,i}^{(k)} = 2\theta_i^{(k)} - Arg(m_k) - 90^\circ \quad (3.70)$$

When there is no damage, damping is proportional and $\theta_i^{(k)}$ is zero and the modal mass is a real number so its arguments are also zero and therefore the phase of the i^{th} component of the FRF at the k^{th} resonant frequency is -90° as expected. When there is local damage, $\theta_i^{(k)}$ is no longer zero and the modal mass of the k^{th} mode shape is a complex number. The modal mass is an overall property of the structure and is dependent on the mass matrix and mode shape. Therefore, local damage does not have much influence on this parameter or its phase. This can be seen by considering the phase of the modal mass in this study at DIL= 9 and at the first resonant frequency ($\omega_1 = 49.32\text{Hz}$) which is equal to 0.0000435° . Therefore, Equation 3.70 can be written as:

$$\beta_{i,i}^{(k)} \approx 2\theta_i^{(k)} - 90^\circ \quad (3.71)$$

This equation relates the phase of the motion of the structural components for a particular mode shape to the phase of the diagonal components of the FRF.

3.6.7. CONCLUSION

A new indicator for the localization of fatigue damage in a fibre glass composite material, *i.e.*, the thick adhesive joint of a wind turbine blade is presented. The indicator analyses the change in the phase of mode shapes of the structural elements to localize damage.

Using a well-known finite element structural code, the results show that this approach can effectively localize simulated damage, though the phase changes observed are relatively small, which may be challenging to detect in practice. In the case of a real wind turbine blade, aerodynamic damping will play a role though this is more likely to affect the global movement of the blade rather than the relative movement of localized elements. It is this relative change that is the important factor in damage detection. Nevertheless, it would require further

work to assess its impact on the ability to detect damage using the proposed indicator.

The change in the phase of mode shape of the structural elements depends on the location of damage and detecting damage in locations with less strain energy is more challenging than in other locations where the level of strain is higher. Therefore, the selection of the most appropriate mode shapes to use for this method plays an important role in the localization of damage.

In a practical measurement system, the phase angle of each structural element should be obtained from the FRF. For this indicator to be used, the spatial change in phase angle should be measured at a few key positions. Installing vibration sensors at relatively few locations on a blade would be sufficient based on a finite element study to determine the relevant mode shapes although damage localization accuracy may be limited.

To have good accuracy in measuring the change in phase angle of mode shapes, a relatively large number of sensors would be required. Increasing the number of sensors adds complexity when installing a monitoring system, however, by using fibre optic sensor technology this is not insurmountable. In addition, the use of ground-based or airborne remote laser scanning technology could be a future solution to be used in periodic inspection. It should be stressed that the purpose of this study was merely to establish the ability to use changes in damping properties as a way of detecting damage. Clearly, further work is required to develop an operational measurement system. The overall dimensions of the structure and the relative size of adhesive layer to laminate thickness will affect the potential change in phase angles during damage initiation. However, the purpose of this work was to provide a proof of concept which would require further research and refinement in a real world situation.

4

ACOUSTIC ANALYSIS

Wind turbine blades carry the risk of impact damage during transportation, installation, and operation. Such impacts can cause levels of damage that can propagate throughout the structure compromising performance and safety. In this study, the effect of impact damage on fatigue damage propagation in test specimens representative of a spar cap-shear web adhesively-bonded connection of a wind turbine blade was investigated. In addition, the effectiveness of using acoustic emissions to detect early impact-induced fatigue damage and to monitor the progression of damage was studied.

S. Khoshmanesh, S.J. Watson, D. Zarouchas, Early detection of impact fatigue damage in an adhesively-bonded connection using acoustic emission, submitted to Engineering Structures, Oct 2023.

4.1. INTRODUCTION

With the increasing size of wind turbine blades, transportation, and installation, especially offshore become ever more challenging. Installation is usually carried out by floating crane vessels. These vessels are subject to the wave-induced motion which leads to the movement of the crane tip and the possibility of blade strikes on the hub or tower [12]. It is prudent to consider this risk and to evaluate the effect of an impact load on a blade.

A wind turbine blade consists of aerodynamic composite shells (facing the pressure side and suction side) and shear webs which are moulded separately and then bonded together in an assembly process using a structural adhesive. The load-carrying parts of the shells (spar caps) are constructed from uni-directional composite laminates such as thick GFRM (glass fiber-reinforced materials). This spar cap-shear web adhesively-bonded connection is a key element for the structural integrity of the blade. Impacts can induce damage in this structure and affect the overall integrity of the blade structure. During the lifetime of a wind turbine, blades need to be periodically inspected. In this study, an evaluation is made of the measurement of structure-borne acoustic emissions and how they could assist in the health monitoring of a blade especially to detect fatigue damage resulting from earlier impacts.

Acoustic emission means recording the elastic waves and extracting their features to diagnose damage in the structure.

Acoustic emission technique to perform the acoustic analysis consists of four sections, figure 4.1, [112]

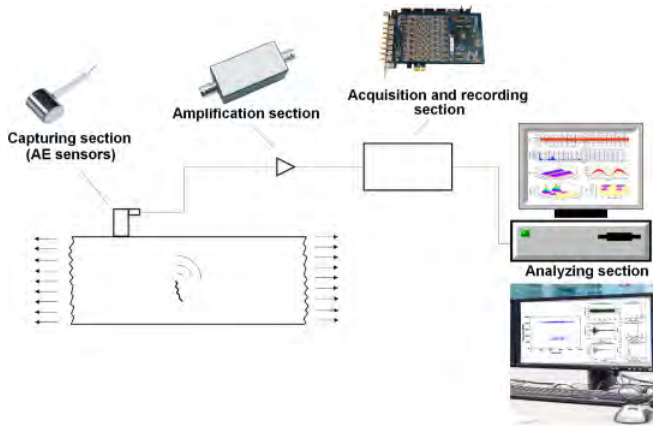


Figure 4.1: Schematic illustration of the acoustic emission tools for recording elastic wave and its features.

- Capturing section.

In this section, the acoustic emission sensors capture the elastic wave generated within the structure. This elastic wave, also called a solid acoustic wave, is the

vibration of a structure on a micro-scale. This vibration is due to the rupture of the atomic band, which releases the elastic energy within the structure. The acoustic emission sensors, usually piezo-electric transducers, convert the surface vibration to the analog current or voltage signal.

- Amplification section.

In this section the analog signal captured by the acoustic emission sensors are amplified and send to the acquisition and recording section.

- acquisition and recording section.

In this section the analog signal from the amplifier is converted to digital signal and recorded. These digital signals are sent to analysis section for further data processing.

- Analysing section section.

In this section the features of recorded acoustic emission signals are extracted. A schematic view of a recorded elastic wave and its features has been shown in figure 4.2. These features are explained as followings,

(1) Threshold.

The threshold is a parameter that users can choose. Based on the nature of their experiment and the possible noises which may arise from different sources, the appropriate value for the threshold is specified. The threshold can help avoid storing the features of signals that can be noisy signals and not the real signals originating from the structure.

(2) Peak amplitude

The highest value of amplitude described as voltage or dB in the Wave form (signal).

(3) Rise time

The time interval between the first threshold crossing and the maximum amplitude. It is usually reported in μs .

(4) Duration

The time interval between the first and the last threshold crossings. It is usually reported in μs .

(5) Count

The number that the waveform crosses the threshold in the increasing direction within the waveform's duration.

(6) Energy

The area beneath the squared waveform within the wave- form's duration.

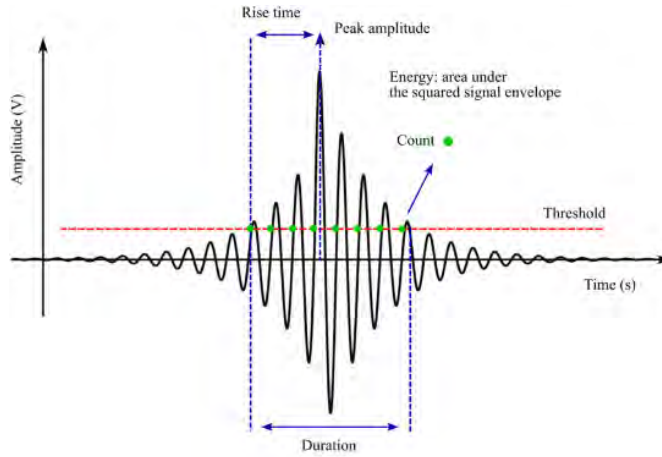


Figure 4.2: Schematic illustration of an elastic waves and its features.

4.2. LITERATURE REVIEW

4.2.1. HISTORICAL OVERVIEW

Acoustic is usually referred to the pressure wave generated in the air and detected by a human's ear. But the term "acoustic emission" is usually referred to the phenomena of the elastic wave generated within a solid material. Elastic wave in the solid material is generated due to the rapid change in the stress state of some regions. Rapid change in the stress of a region can be associated with the occurrence of the tiny cracks in a solid material [113]. In a metal both intergranular and trans-granular cracking of metal crystallites can generate acoustic emission. In addition emission can also be generated at inclusions by either the fracture of the inclusion or the breaking of the bonds between the inclusion and metal. In a composite materials, matrix cracking, de-bonding of fibre from the matrix, de-lamination of two plies of lamina and de-bonding of the laminate from the adhesive in a adhesive joint and fibre breakage are the source of acoustic emission, [113].

Although the discovery of acoustic emission (AE) is a point of discussion between the reporters but it seems that AE has been discovered by F. Kishinoue in Japan around 1933. He studied the process of shock occurrence in a wood specimen under flexural stress. He used a phonograph to pick up the AE signals by inserting the steel needle into the tension side of a wooden beam under the bending stress, [114]. As bending proceeded the cracks in the wooden beam generated the elastic wave. This elastic wave vibrated the needle and then an oscillogram picked up the vibration of the needle and converted it to an electrical signal. This study was delivered by F. Kishinoue on November 21, 1933 at a meeting of the Earthquake Research Institute in the University of Tokyo (Imperial University of Tokyo). The article was published in 1934 and later it was translated

into English by K. Ono and published in the Journal of Acoustic Emission, [115].

In Germany, early AE experiments were performed by F. Förster. He measured the AE signals generated during the martensite transformations of a wire-shaped nickel-steel specimen. He used a built electro-dynamic transmitter/receiver system to transform the mechanical vibrations into electrical voltages[114].

In the geological field, in 1936, L. Obert conducted seismic velocity tests in the lead-zinc mines of northern Oklahoma and during this experiment he reported the discovery of micro-seismic emissions in the rock[114].

A major achievement in the field of AE was not succeeded until the research study of Kaiser during his PhD. He studied the behaviour of acoustic emission during the deformation and fracture of various materials [116]. During his study he discovered a famous irreversibility, which is now called as the Kaiser effect. Ten years later in 1960, the Kaiser discovery drew the attention of B.H Schofiels and He reexamined the Kaiser effect and he entitled his work as "Acoustic Emission". This was the first time that the terminology of acoustic emission was used, [116].

In a period from 1960-1980 the majority of research in AE field was focused on the identification the AE sources and the relation of the micro scale parameters such as dislocations with the AE signals. In these years the the failure of pressure vessels during the pressure test in the nuclear power plant was one of the major issue. So a lot of researchers tried to use the AE technique to identify and monitor the crack growth during the test and to prevent such a failure. SCRUBY et.al and Bentley summarised the studies related to this subject in two separate works, [117], [118]. It is worth to add that regardless of all these efforts the success was limited.

In a period from 1980-1994 the decline in the nuclear power plant which was the most promising area for the AE applications lead to less investments in the AE field. In these years the AE researchers were looking for the other industries especially petrochemical plant and aerospace industries to examine the AE technique. Among these researchers, T. J. Fowler successfully employed AE signals for the detection of damage in a fibre reinforced plastic petrochemical pressure vessels during the pressure test. By employing the AE system, he prevented the catastrophic failure of the vessel and eliminated the risk of loss of life during the test. It was quite impressive safety record,[116]. His AE inspection programs of fibre reinforced plastic vessels and piping became the primary mission of the Committee on Acoustic Emission from Reinforce Plastic (CARP), resulting in codification by the American Society for Testing and Materials (ASTM) and American Society of Mechanical Engineers (ASME).

In addition continuous growth of composite materials, monitoring of the friction source of damage in the rotary equipment's internal parts such as i.e bearings and inspection of the deteriorated concrete bridges, were the other factors that helped the acceleration in the development of AE.

Since 1994, with an increase in the RAM of computer for data storage and the availability of the powerful software for post processing of data, the AE has been greatly developed. Nowadays AE is one the promising method for structural health monitoring (SHM) and researchers have tried to use AE techniques for

damage diagnostic and prognostic in a structure. In the next section the state of the art of AE techniques for damage diagnostics in a composite material have been presented.

4.2.2. ACOUSTIC EMISSION IN A COMPOSITE MATERIALS

In these years, researchers have been investigated the application of the AE techniques for damage characterization in a composite material.

Manufacturing flaws and impact are two main sources for initiation and propagation of damage in a composite material. These sources of damage under the quasi static or the fatigue load, generate the elastic wave, called AE events.

Actually composite materials in the case of manufacturing process can be divided into two main categories; composite laminate and composite joint. Composite laminate is the bonding of different plies (lamina) of a composite material by the action of the resin infusion for a fibre glass material and the heat and pressure for the carbon fibre material. The adhesive joint is the bonding of two composite laminate by the use of an adhesive.

Chou et al. investigated the inception of failure in carbon fiber reinforced composite (CFRP) pressure vessels by measuring the accumulation of AE events during a pressure test [119]. It was concluded that an abrupt increase in the AE hit rate is an indication of the initiation of failure of the vessel. Lissek et al. tried to correlate the crack growth during the inter-laminar toughness testing of a fiber-reinforced composite material to the material properties. They used a double cantilever beam (DCB) test specimen and measured the cumulative energy of AE events during a quasi-static loading process and observed a jump in the cumulative energy during the loading process which was taken as a sign of the initiation of damage [120]. Nikbakht et al. studied the delamination of a composite laminate with different interface fiber orientations using an AE technique [121]. In this case, a fiberglass DCB composite test specimen was used. It was observed that the load-displacement curve and cumulative AE events seemed to be well correlated. Once again, a sharp jump in cumulative AE events was associated with damage initiation. Barile undertook a similar study to investigate mode I delamination growth for a DCB test specimen made of CFRP material [122] noting similar results to [121]. Saidane et al. investigated the failure mechanism of the Mode I inter-laminar fracture toughness of flax, glass, and hybrid flax-glass fiber woven composites using an AE technique [123] using the increase in the rate of the cumulative AE events to predict the initiation of damage. They divided the AE events into four clusters and tried to find the contribution of each cluster to the damage propagation.

Tabrizi et al. investigated the behavior of glass/carbon fiber hybrid composites under pure bending and tensile loading conditions also using an increase in the rate of cumulative AE events as a sign of initiation of damage in a test specimen, [124]. Ali et al. used the same method to analyze the damage mechanism in woven carbon fabric laminates under a tensile test [125]. Ameer et al. investigated the identification of damage mechanisms of unidirectional carbon/flax hybrid composites using an AE technique [126]. They performed static and fatigue

tension tests on test specimens consisting of unidirectional carbon and flax fiber plies with different stacking sequences to create different levels of damage, classifying the amplitude of AE event from low to high which were associated with four types of damage including matrix cracking, fiber-matrix de-bonding, delamination/fiber pull-out, and fiber breakage. Based on this assumption, they calculated the cumulative number of AE events and cumulative energy of AE events for each class. Haggui et al. used the same methodology as [126] to describe the damage mechanism in flax fiber reinforced thermoplastic composites [127]. Khademi et al. used wavelet analysis of acoustic emission signals to characterize damage in carbon/epoxy composites under a quasi-static tensile test [128].

Saeedifar et al. used AE and machine learning to characterize damage in an adhesively-bonded Bi-material joint [129] employing two different structural adhesives, ductile (Methacrylate-based) and brittle (Epoxy-based), to bond CFRP skins to a steel core. The fabricated joints were subjected to quasi-static tension load tests while damage evolution was monitored using AE. In order to distinguish and classify different damage mechanisms, different tests were conducted. Each test on the coupons was representative of one type of damage mechanism present in an adhesively-bonded Bi-material. The AE signals captured during these tests were used to train an ensemble bagged tree classifier. The same group used acoustic emission to assess low-velocity impact damage in a Carbon Fiber Reinforced Polymer (CFRP) composite plate [130]. The test specimen was subjected to a repeated quasi-static indentation test where a loading-unloading-reloading test profile with five repetitions was adopted. A Felicity Ratio (FR) was used to measure damage severity during loading. Pasco et al. studied crack growth during the cyclic fatigue loading of a double cantilever beam (DCB) specimen, consisting of two aluminum arms [131]. It was found that crack growth can occur both during loading and unloading, but only while the strain energy release rate is above a crack growth threshold value. It was concluded that to fully understand the link between the acoustic emission signals and the actual crack growth process, further research was necessary.

Round et al. investigated the static load and fatigue behavior of glass/epoxy composite laminates. The specimens were subjected to static loading and cyclic fatigue tensile tests and the AE events were recorded [132]. AE events based on the amplitude range were classified into four clusters. Each amplitude range was associated with one type of failure. The damage was divided into matrix cracking, matrix fiber de-bonding, delamination, and breakage with amplitude ranges of 45 – 65dB, 65 – 80dB, 80 – 90dB, and greater than 90dB, respectively. The contribution of each class to the damage propagation was estimated during the static loading and cyclic fatigue tension tests. Saeedifar et al. studied damage evolution in a CFRP composite material under a quasi-static indentation loading using AE [133]. A sentry function (the logarithm of the ratio of mechanical energy given to the test specimen during loading to the AE energy due to the damage) was used to characterize damage propagation. Different AE event clustering methods were used to evaluate the contribution of different damage mechanisms during testing. It was concluded that a hierarchical model was a good candidate

for clustering AE events related to three damage mechanisms, i.e., matrix cracking, fiber breakage, and delamination. The same approach was used to detect scarcely visible damage in CFRP composite material [134]. Saidane et al., Malpot et al. and Zhou et al. used clustering of AE events to monitor damage propagation in hybrid flax-glass fiber composites, woven glass fiber reinforced plastic (GFRP), and woven CFRP under quasi-static tension, fatigue tension, and quasi-static tension tests, respectively [123, 135, 136].

Tang et al. attempted to classify AE events from a wind turbine blade during a fatigue test [137]. K-means clustering was used to classify AE events measured during the fatigue test of a 45.7 m long wind turbine blade loaded in the flap-wise direction into four different classes. These classes were related to the different damage mechanisms that occurred during the fatigue test including matrix cracks, delamination, de-bonding, and fiber breakage.

The studies described above rely primarily on observing an abrupt change in the rate of generation of accumulated AE events during constant loading conditions to identify damage. This has limitations in a real loading scenario where a wind turbine blade is operating in turbulent and time-varying wind conditions. Furthermore, it is difficult to monitor progressive damage. To address these limitations, in this paper, we explore the possibility of monitoring the spatial distribution and local density of AE events to identify damage initiation and monitor damage accumulation during the fatigue life of a representative composite test specimen.

Sørensen et al. conducted an experimental study at Risø National Laboratory to investigate damage evolution in wind turbine blades [138]. They subjected a 25 m wind turbine blade (type V52, provided by Vestas Wind Systems A/S) to full-scale extreme loads and cyclic loading corresponding to a 20-year fatigue life. Seven types of damage were observed, with one major type being damage formation and growth in the adhesive layer joining the skin and main spar flanges (skin/adhesive debonding and/or main spar/adhesive layer debonding). Sundaresan et al. also conducted a static test on a 9 m wind turbine blade and demonstrated that the high-pressure skin, spar cap, and shear web are areas prone to damage in wind turbine blades [139]. Mishnaevsky et al. reviewed the root causes and mechanisms of damage and failure in wind turbine blades [140]. This review, along with two others by Shohag et al. [141] and Ciang et al. [142], indicated that one critical area prone to damage is the upper spar cap/flange of the wind turbine blade. Mishnaevsky et al. concluded that the strength and durability of wind turbine blades are largely controlled by the strength of adhesive joints. These studies highlight the critical role of the spar cap-shear web adhesively bonded connection in wind turbine blades. Zarouchas et al., Sayer et al., and Khoshmanesh et al. conducted experimental investigations into the evolution of fatigue damage in this joint [8, 9, 143].

Impact during transportation is one of the sources of damage to wind turbine blades. However, the effect of initial impact with varying energy levels on fatigue damage propagation in a thick adhesively bonded connection has not been previously explored. In this chapter, we present an experimental study to in-

investigate the effect of this initial impact on fatigue damage accumulation in the adhesive joint. Additionally, we examine the feasibility of using acoustic emission measurements to monitor damage accumulation by analyzing their spatial distribution and local characteristics.

4.3. METHODOLOGY

To investigate the effect of impact damage on the fatigue damage accumulation process in a spar cap-shear web adhesively bonded connection of a wind turbine blade, three cases of impact damage were instigated using a gas cannon on test specimens representative of this bonded connection. These three cases were chosen to induce different levels of initial damage on the test specimens.

The test specimens were then subjected to fatigue tension tests with a stress ratio, R (ratio of minimum load amplitude to maximum load amplitude) equal to 0.1 and a fatigue cycling frequency of 3 Hz. Two acoustic sensors were attached to the top and the bottom of the test specimens to measure AE events. An AE event (elastic wave) is generated in a material when the bonds between atoms are broken. This happens when the test specimens are subjected to a load. To identify the spatial distribution and local density of generated AE events the test specimens were divided into a number of spatial elements subsequently referred to as bins. The cumulative number of AE events generated in each bin during the fatigue tests was determined. The difference in the arrival time of AE events recorded by two sensors was used to locate the source of damage [144]:

$$X = (d - V \cdot \Delta t) / 2 \quad (4.1)$$

Referring to the schematic of a test specimen subjected to a fatigue tension load F as shown in Figure 4.3, X is the distance of the source of an AE event from Sensor 1, V is the velocity of the elastic wave associated with the event, Δt is the difference in the time of arrival of the event at Sensor 1 and Sensor 2 and d is the distance between the two sensors.

The cumulative normalized number of AE events, $N_n(t, i)$, detected in bin i at time t is given by:

$$N_n(t, i) = \frac{N(t, i)}{N_o} \quad (4.2)$$

where $N(t, i)$ is the absolute number of the AE events generated since the beginning of the fatigue test in the i^{th} bin of each test specimen and N_o is the total number of the AE events generated throughout the entire length of a test specimen during its fatigue life. This measure gives an indication of the spatial location of the damage to the test specimen.

A high-resolution camera was used to photograph the damaged test specimens. Using the pictures of the damaged test specimens at different fatigue life cycles the effect of impact on the fatigue damage accumulation process was investigated.

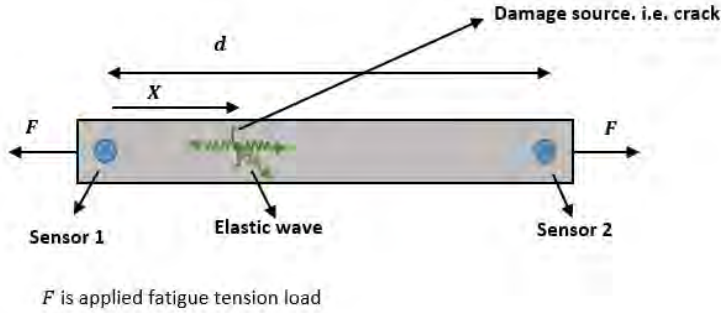


Figure 4.3: Schematic illustration of the test specimen in a tension fatigue load with a damage source, i.e. crack and two sensors to identify the damage source.

An acoustic emission technique was used to detect the initial impact damage on the test specimens. This was done by dividing the test specimens into a number of spatial elements subsequently referred to as bins. The cumulative number of AE events generated in each bin during the initial phase of damage was determined. The bin with the largest number of AE events was expected to be the area where impact damage was initially instigated. To monitor the fatigue damage accumulation process during the fatigue life, the cumulative spatial distribution of AE events within the test specimens was analysed.

4.4. EXPERIMENTAL SET UP

4.4.1. TEST SPECIMEN

The test specimen used in the research was an adhesive joint representative of a spar cap-shear web adhesively bonded connection that would be seen in a wind turbine blade. Several test specimens were manufactured. Each test specimen consisted of two skins of unidirectional fiberglass which were made by the infusion of epoxy resin into three layers of unidirectional (UD(0)) fibers. These two skins were then bonded together by a layer of adhesive with a thickness of 0.5cm. The material properties of all components for manufacturing the test specimens are given in Table 4.1 and a schematic illustration of a test specimen is shown in Figure 4.4.

Table 4.1: Mechanical properties of the different materials used for the manufacturing of the test specimens where: E_Y =Young's Modulus, σ_u =ultimate strength and ρ =volume density.

	Material specification		E_Y (GPa)	σ_u (MPa)	ρ (g/cm ³)
Adhesive	Resin	Epoxy Epikote Resin MGS BPR135G2	5.5	75	1.1-1.2
	Curing agent	Epoxy Epikure Curing Agent MGS BPH1355G			
Adherent	Resin	Epoxy Epikote Resin MGS RIMR135	31-33	376	1.3-1.17
	Curing agent	Epoxy Epikure Curing Agent MGS RIMH 137			0.99
	UD fibre glass	Fibre glass non-crimp fabric UD (0), 1210g/m ² , S14EU960			2.65

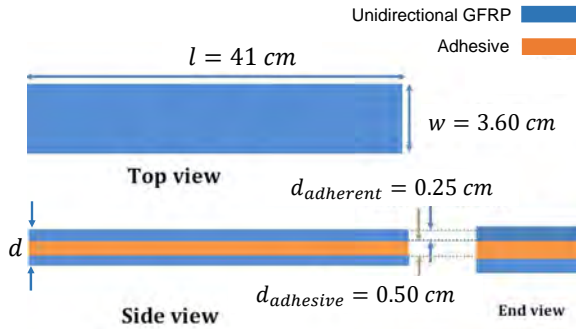


Figure 4.4: Schematic illustration of a test specimen.

4.4.2. IMPACT CASES

The test specimens were fixed on both ends and then different levels of impact damage were imposed on the test specimens using a gas cannon. A gas cannon uses compressed air to shoot a projectile with a specified energy using a regulator to adjust the air pressure. There is also an air relief valve that can be opened manually to fine-tune this pressure. Once the pressure is set to the desired level, to which the velocity of the projectile is proportional, a valve is opened and the projectile is propelled via a cylinder to the intended target. The experimental set-up using the gas cannon is shown in Figure 4.5.

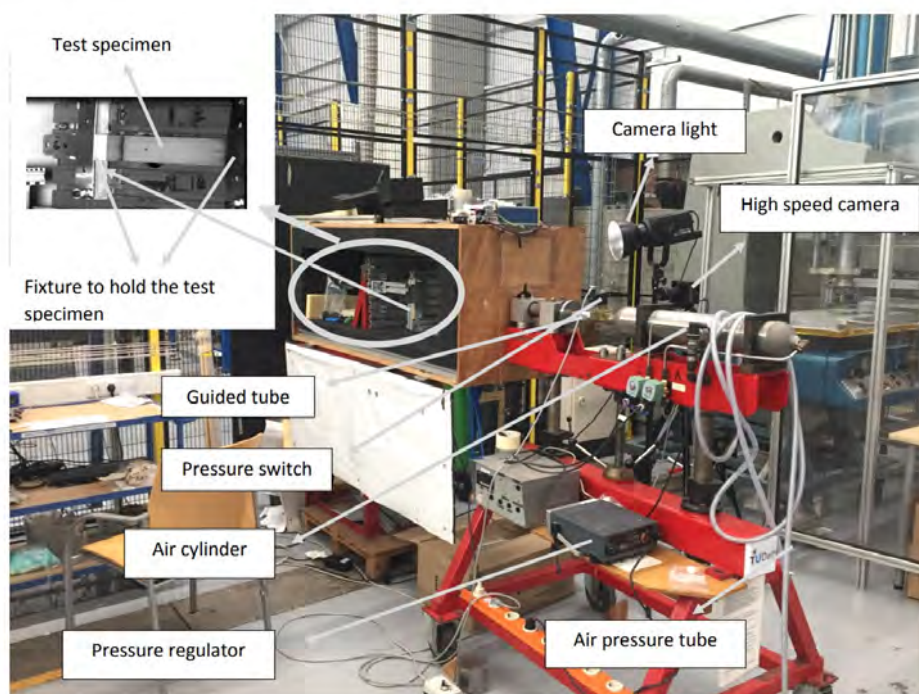


Figure 4.5: Experimental set-up using the gas cannon to impose impact damage on the test specimens.

In Figure 4.6, images of the projectile before, during and after hitting the test specimen are shown.

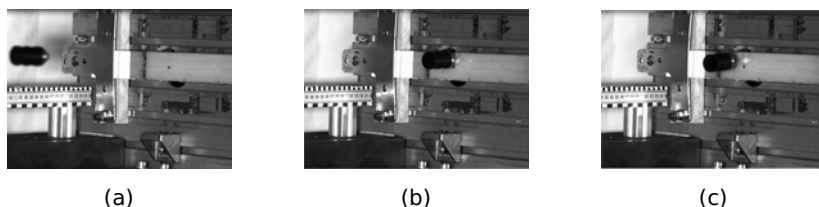
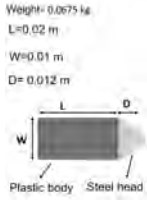


Figure 4.6: Images of the projectile (a) before (b) during and (c) after hitting the test specimen.

Three impact cases (Case 1, Case 2, and Case 3) representing different levels of impact damage were imposed on the test specimens. Photos of the impact-damaged specimens are shown in Figure 4.7. The velocity of each projectile was measured using a high-speed camera. With Having the velocity and mass of the projectile the kinetic energy or energy level can be calculated. The characteris-

tics of each impact including projectile properties, velocity, and energy level are given in Table 4.2.

Table 4.2: Impact test characteristics and projectile properties.

Energy level	Test specimen No	projectile velocity (m/s)	Energy (Joule)	Projectile properties
Case 1	C.1.1	21.1	15.7	
	C.1.2	22.7	17.4	
	C.1.3	21.7	15.9	
Case 2	C.2.1	25.9	22.6	
	C.2.2	27.3	25.1	
	C.2.3	26.3	23.4	
Case 3	C.3.1	31.9	34.3	
	C.3.2	30.3	30.4	
	C.3.3	30.6	31.6	

For each impact case, three test specimens were damaged giving a total of nine test specimens used for the experiment. The test specimens after impact are shown in Figure 4.7. In this figure, the nine test specimens are divided into three sets with each set showing the three different cases of impact damage.

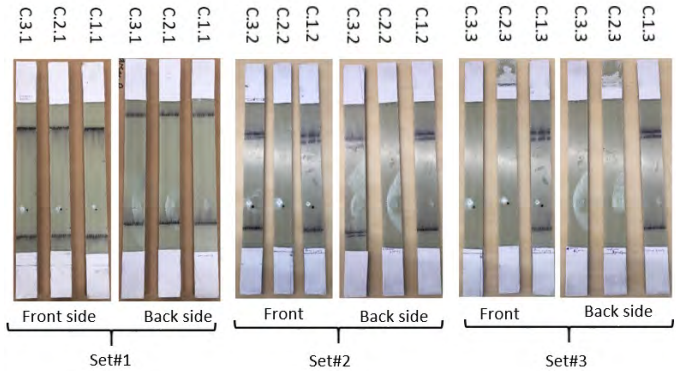


Figure 4.7: The set of test specimens following the initial impact damage showing both front and back.

4.4.3. ACOUSTIC MEASUREMENT

To capture AE events, during the fatigue tests, two broadband, resonant-type, and single-crystal piezoelectric transducers from Vallen Systeme GmbH, model AE1045SVS900M, with two external 34 dB pre-amplifiers were used. The optimum operating frequency range of the AE sensors was [100–900] kHz. To record the AE events, an AMSY-6 Vallen, 4-channel AE system with a maximum sampling rate of 10 MHz was used. The threshold of the receiving AE signals, sampling rate, Duration Discrimination Time (DDT) and Rearm Time (RAT), were 60 dB, 2 MHz,

200 μs and 400 μs , respectively. Sonotech Ultrasonic couplant was applied between the sensor and specimen surfaces to get an appropriate acoustic coupling. The functionality of the AE sensors and the data acquisition system was checked by performing a pencil lead break test according to the ASTM E976 standard. The test setup is shown in Figure 4.8.

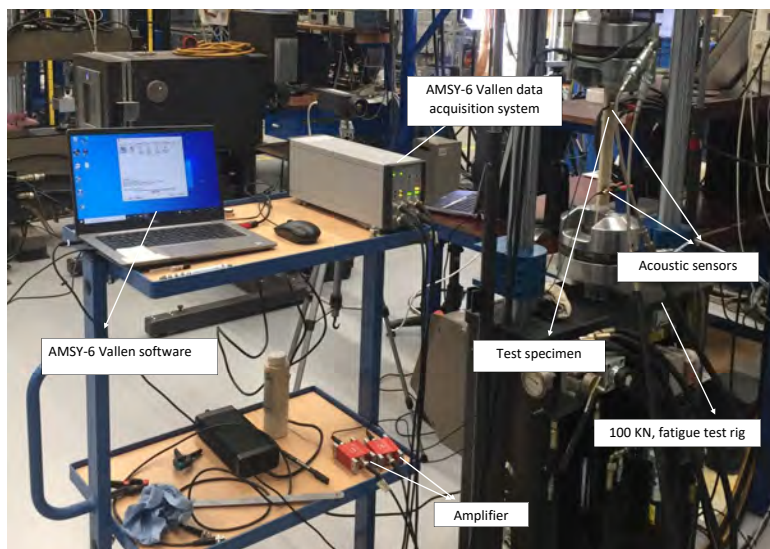


Figure 4.8: The AE measurement and fatigue test set-up.

4.5. RESULTS AND DISCUSSION

4.5.1. FATIGUE DAMAGE ACCUMULATION PROCESS BASED ON HIGH-RESOLUTION PHOTOS

During each fatigue tension test, photos of the test specimens by a high-resolution camera at different fatigue load cycles are taken. As the three test specimens showed a similar pattern of damage, the results of only one test specimen for each case of impact damage is shown.

The fatigue damage accumulation process for C.1.1 is shown in Figure 4.9. As can be seen from this figure, damage initiates with cracks in the adhesive during the early stage of the fatigue test. This is the initiation phase of damage (Phase I). Cracks in the test specimen are transverse and initiate within the adhesive. They grow transversely and reach the interface of laminate and adhesive causing de-bonding of the laminate from the adhesive. Each horizontal white line seen in Figure 4.9 (at the position where a crack has occurred) is a de-bonded area. The width of each line shows how far the crack has progressed in depth within the test specimen. As the number of fatigue load cycles increases, cracks become widespread throughout the test specimen and this trend continues until the number of cracks reaches a saturation level. This phase of damage is

known as the crack saturation level (Phase II). During Phase III, cracks deepen and consequently the de-bonded areas increase. The de-bonded areas grow as the number of fatigue load cycles increases. Finally, the de-bonded areas become connected leading to failure of the test specimen. The first crack is not within the impact zone and subsequent cracks which appear are not associated with this zone. This indicates that the fatigue damage accumulation process was not influenced by the size and location of the impact damage and it is identical to that seen in previous tests on an undamaged test specimen [145].

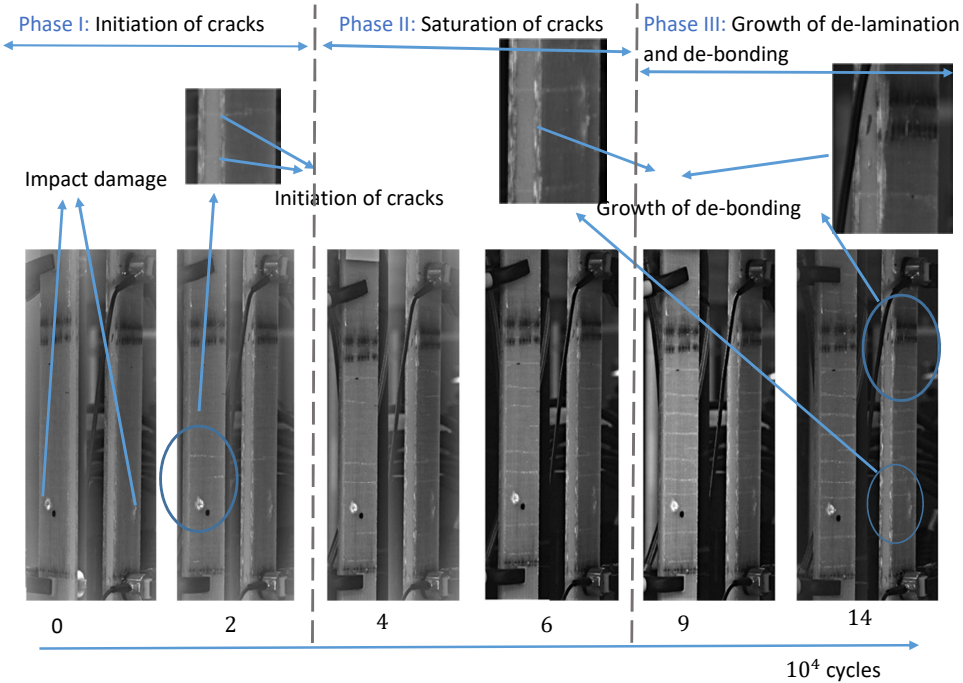


Figure 4.9: Damage propagation in one of the test specimens (C.1,1) subjected to the low energy level impact. The left image of each pair shows the front where impact occurred and the right image is the back. Each photo shows an AE sensor attached at the top and bottom of each test specimen.

The fatigue damage accumulation process for C.2.1 is shown in Figure 4.10. In this case, crack initiates close to the impact zone. As damage propagates, a higher crack density than in other areas of the test specimen is observed near the impact zone. The de-laminated area in the impact zone also grows more than elsewhere in the test specimen during the fatigue test ultimately resulting in failure in this zone.

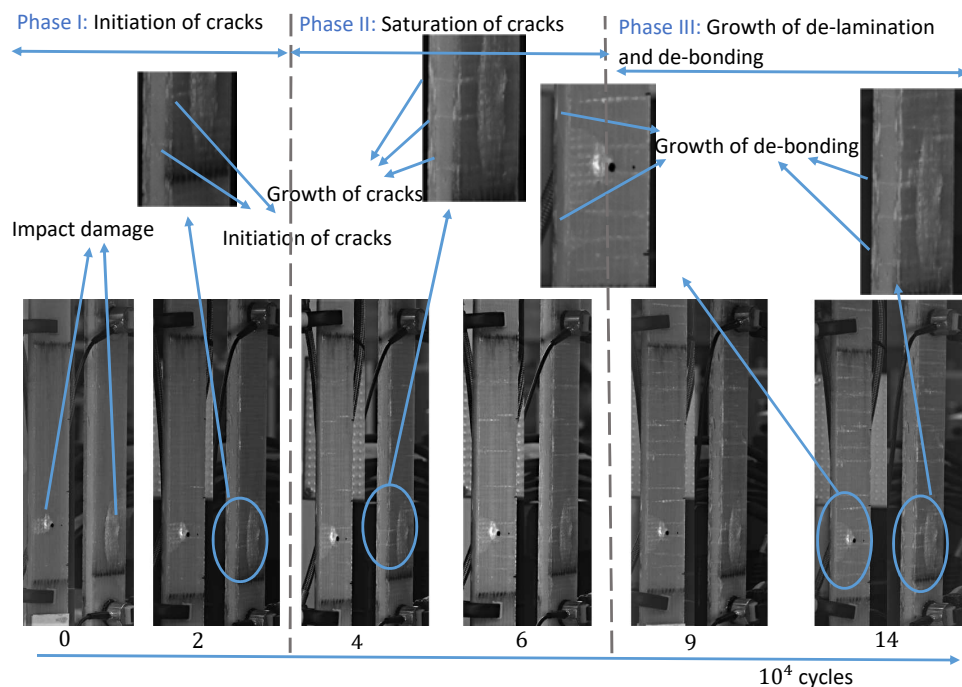


Figure 4.10: As Figure 4.9 but for C.2.1.

The fatigue damage accumulation process for C.3.1 is shown in Figure 4.11. Similar to C.2.1, the early cracks occur at the impact zone and the crack density in this zone is higher than other parts of the test specimen. In this case, the de-laminated area around the impact zone grows more extensively and faster compared with C.2.1 leading ultimately to failure in this zone.

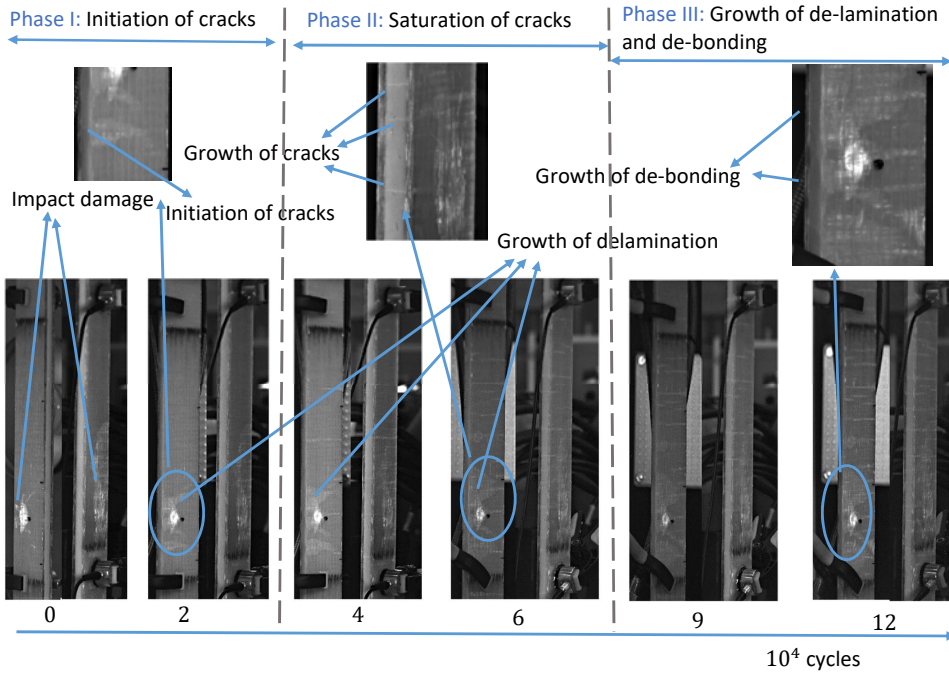


Figure 4.11: As Figure 4.9 but for the C.3.1.

4.5.2. EARLY DETECTION OF IMPACT DAMAGE

To detect the impact damage during Phase I of the fatigue test, the test specimens were divided into 2 cm bin lengths as shown in Figure 4.12. Each impact position was 4.2 cm from the lower AE sensor as shown in the photos in Figures 4.9 to 4.11. The length (L) of the de-laminated area surrounding the impact point in the lateral direction depends on the impact energy level, varying from 2 cm to 8 cm. To detect the impact damage in the early stage, the normalized number of AE events (against a total number of acoustic events) during Phase I of damage in the fatigue test for each bin was calculated. Because impact damage accelerates the generation of AE events, it was expected that the bins located in the impact zone would have the highest number of events. In this section, results for all three test specimens subjected to the same level of impact energy are presented to show the degree of variability in damage localization.

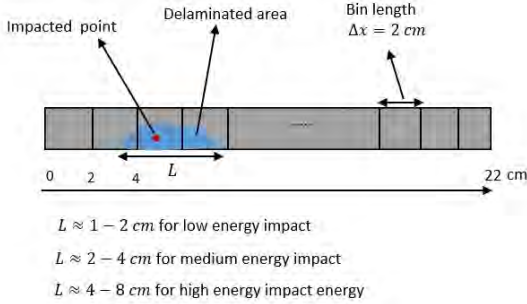


Figure 4.12: Schematic illustration of the test specimen divided into 2cm bins. Also illustrated are the impact point, and length of de-laminated area (L) in the lateral direction.

4

CASE 1 IMPACT

The total number of normalized AE events by bin during Phase I of the fatigue test for the test specimens subjected to the Case 1 impact is shown in Figure 4.13.

It can be seen for C.1.1 that the 0 – 2 cm bin (inside the impact zone) was not the most damaged section but rather the 20 – 22 cm bin, far from the impact area. For C.1.3, the most damaged section was located between 20 – 22 cm which is also far from the impact zone.

CASE 2 IMPACT

The corresponding results for the test specimens subject to the Case 2 impact are shown in Figure 4.14. It can be seen that the bins between 0 – 2 cm and 4 – 6 cm are the most damaged sections of C.2.1 which are relatively close to or within the impact area respectively.

The results for C.2.2 and C.2.3 show peaks in normalized events in bins 2 – 4 cm and 4 – 6 cm, respectively, which are inside the impact zone.

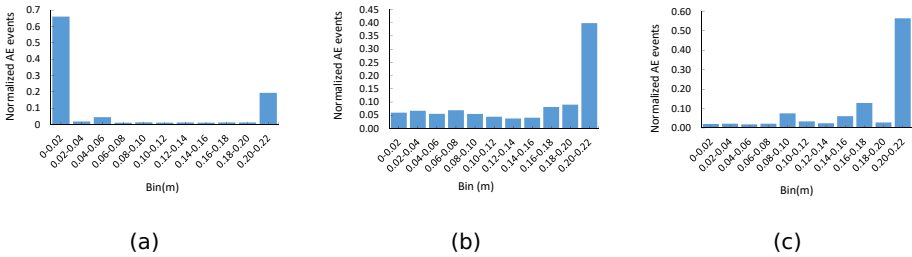


Figure 4.13: The total number of normalized AE events by bin at the end of Phase I of the fatigue test for the three test specimens subjected to the Case 1 impact: a) C.1.1 b) C.1.2 c) C.1.3.

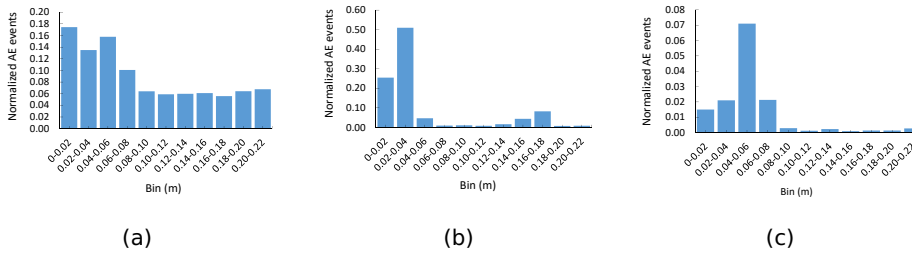


Figure 4.14: The total number of normalized AE events by bin at the end of Phase I of the fatigue test for the three test specimens subjected to the Case 2 impact: a) C.2.1 b) C.2.2 c) C.2.3.

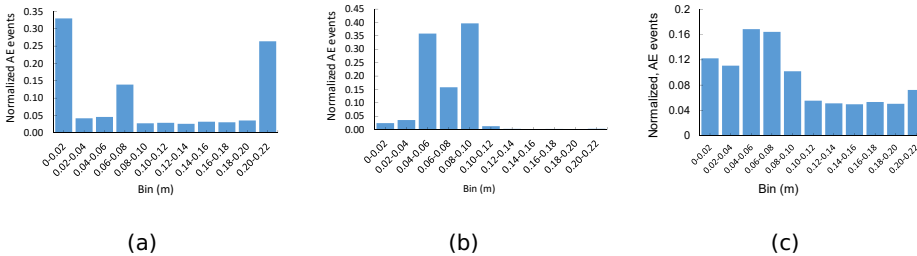


Figure 4.15: The total number of normalized AE events by bin at the end of Phase I of the fatigue test for the three test specimens subjected to the Case 3 impact: a) C.3.1 b) C.3.2 c) C.3.3.

CASE 3 IMPACT

Figure 4.15 shows the corresponding results for the test specimens subjected to the Case 3 impact. C.3.1 shows the largest peak in normalized events in the bin close to the bottom of the specimen (0 – 2 cm), with another smaller peak at the top (20 – 22 cm). C.3.2 and C.3.3 show the largest number of normalized events in the bins spanning the sections from 4 – 10 cm which encompass the impact zone.

CORRELATION BETWEEN IMPACT AND FATIGUE DAMAGE

From the results of the three cases of damage, the AE measurements would seem to broadly confirm the levels of visual damage observed in Figures 4.9–4.11. For the test specimens subjected to the Case 1 impact, fatigue damage is not correlated with the area of the initial impact. For the test specimens subjected to the Case 2 and Case 3 impacts, fatigue damage does appear to initiate close the area of impact, though there is some variability between the test specimens. In some cases, peaks in fatigue damage occur at the ends of the specimens which may

be due to the gripping force induced by the end clamps where damage initiation and growth is facilitated.

4.5.3. MONITORING OF THE FATIGUE DAMAGE ACCUMULATION PROCESS BY USING THE SPATIAL DISTRIBUTION OF AE EVENTS

During the fatigue tension tests, the amplitude of the load increases gradually to induce damage and facilitate its growth. The change in the generation of AE events can be a sign of damage in the test specimen during the fatigue tension test. But the increase in load also increases the generation of AE events, the phenomenon known as the Kaiser effect,[116]. The Kaiser effect increases the AE generation homogeneously within the test specimens. Therefore, to localize damage, the local density of AE events in a specimen should be considered alongside an indicator of the load. For this purpose a load ratio (LR) can be defined:

$$LR = \frac{F}{F_i} \quad (4.3)$$

Where F is the load during the fatigue test and F_i is the initial load at the start of the fatigue test. The load ratio is increased during the fatigue test to assess the effectiveness of using the spatial distribution of AE events for identification and monitoring of the fatigue damage accumulation under variable load conditions. In addition, increasing the load ratio causes the development of fatigue damage propagation at a faster rate. This reduces the required time for the experimental test and the storage space needed for the acoustic data.

CASE 1 IMPACT

Figure 4.16 shows temporal changes in normalized AE events and load ratio during the fatigue test for C.1.1. This gives an indication of where changes in the load give rise to an increase in AE event generation, but also shows where damage is accelerating where it is not necessarily associated with a change in the load. Figure 4.17 shows the corresponding spatial density of normalized AE events. The damaged sections can clearly be seen during the fatigue life cycle marked in red. Initially, the [0 – 2] cm and [20 – 22] cm sections of the test specimen show significant damage. As the fatigue test progresses and damage propagates in the test specimen, the [17 – 20] cm section of the test specimen show significant damage. It is therefore clear that throughout the full fatigue test, the location of the fatigue damage is not associated with the impact zone.

Figure 4.18 shows the changes in normalized AE events and load ratio during the fatigue test for C.1.2. The corresponding spatial density of AE events for this test specimen can be seen in Figure refSpatial distribution, TS L2. Similar results are seen compared to C1.1 and if anything, the damage is quite uniformly distributed throughout the test specimen for the duration of the fatigue test. Figure 4.20 show the changes in normalized AE events and load ratio during the fatigue test for C.1.3 and Figure 4.21 shows the corresponding spatial density of

AE events. There a notable increase in events at around 3.5×10^4 cycles which corresponds to areas of damage indicated in red in Figure 4.21, but otherwise damage in this case is quite uniformly distributed and not associated with the location of the impact damage.

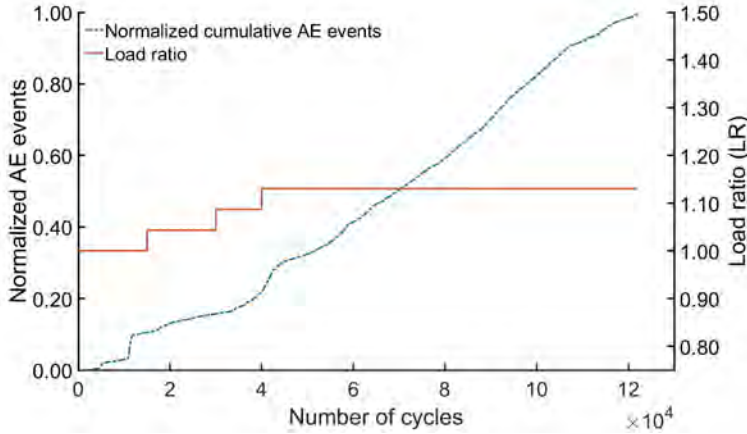


Figure 4.16: Normalized AE events during the fatigue test for C.1.1.

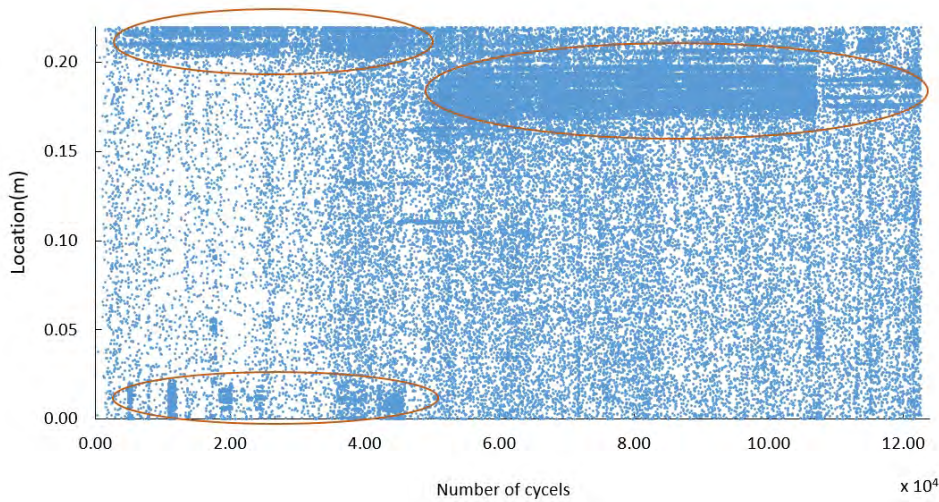


Figure 4.17: Spatial distribution of AE events during the fatigue life, for C.1.1.

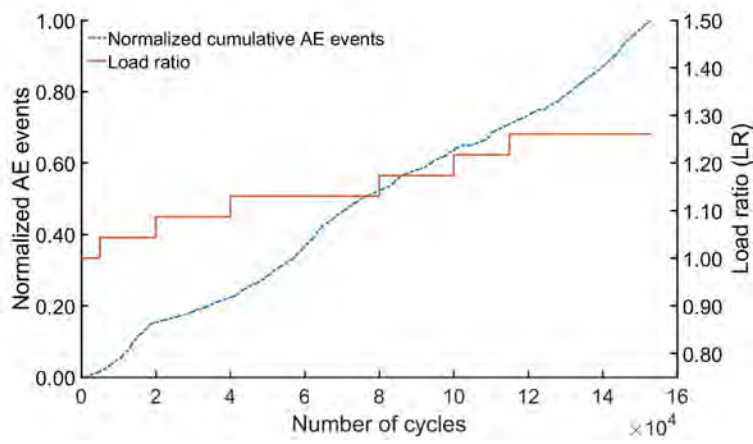


Figure 4.18: As figure 4.16 but for the C.1.2.

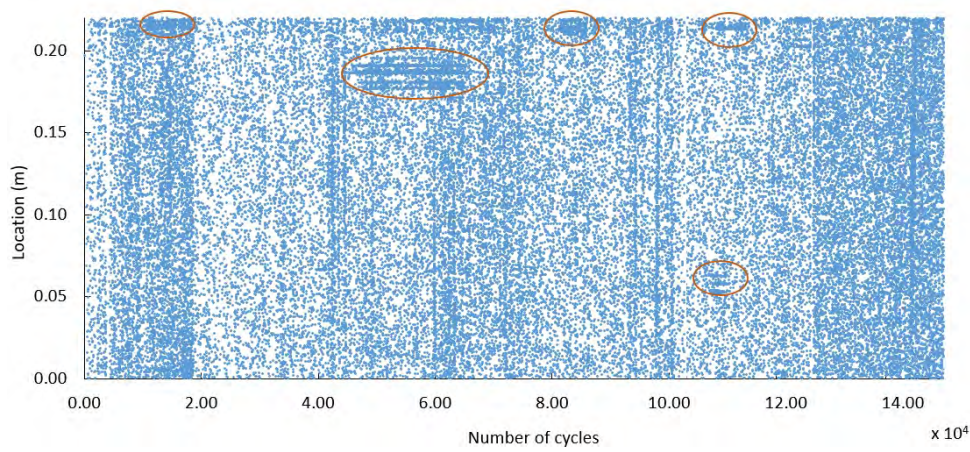


Figure 4.19: As figure 4.17 but for C.1.2.

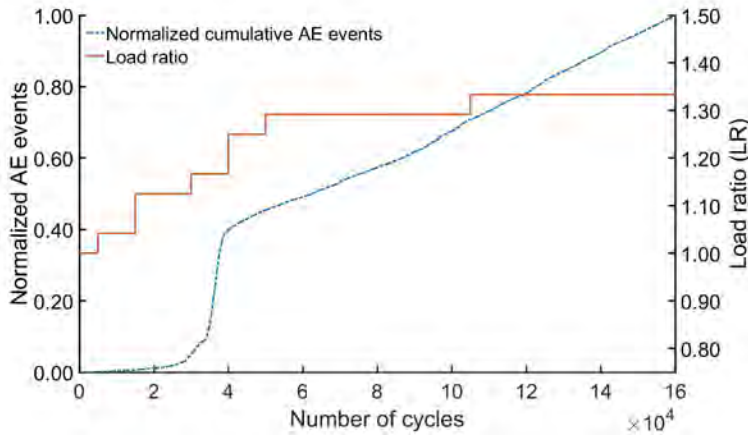


Figure 4.20: As figure 4.16 but for C.1.3.

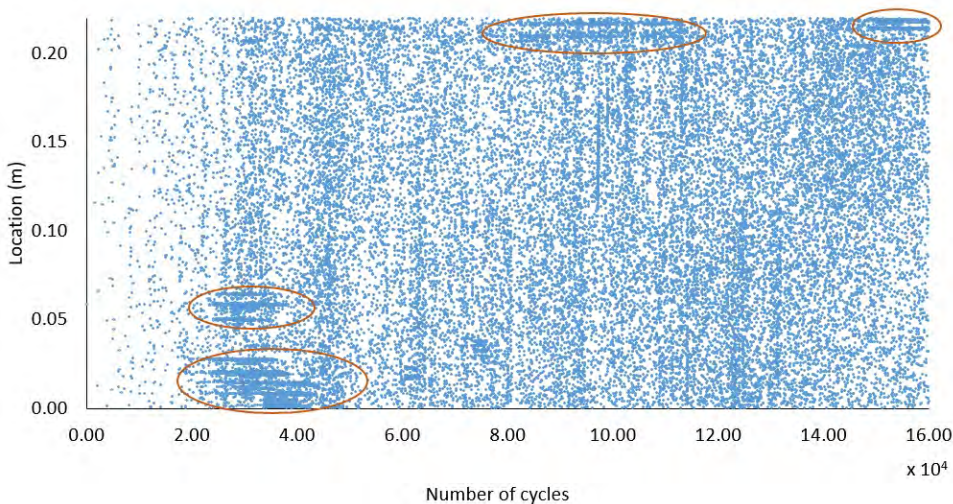


Figure 4.21: As figure 4.17 but for C.1.3.

CASE 2 IMPACT

Figures 4.22 to 4.27 show the corresponding results for the the test specimens subjected to the Case 2 energy impact. For all test specimens, there is a definite increase in the density of AE events within the impact zone at the beginning of the fatigue tension test, indicating that significant damage has occurred in this area. Continual growth in damage (higher density of AE events) within the impact zone for C.2.2 and C.2.3 can be seen until the end of the fatigue tension test. For C.2.1, the damage is initiated in the impact zone and then as the number of fatigue

load cycles increases, it propagates to other sections of the test specimen. This propagation can be seen in Figure 4.23 between load cycles 4×10^4 and 6×10^4 .

4

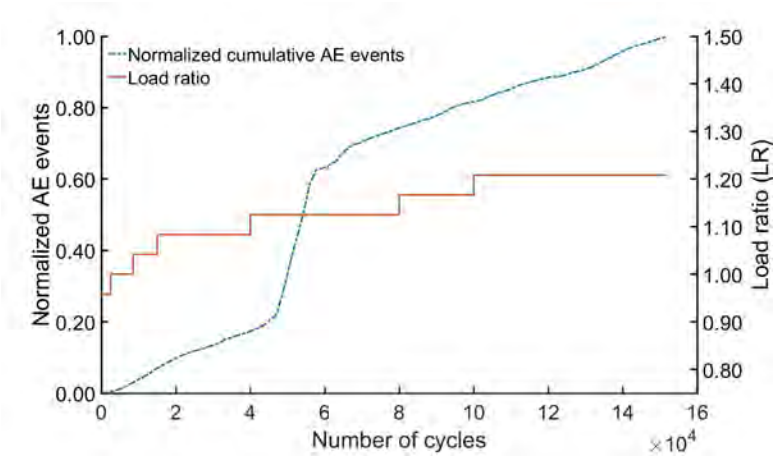


Figure 4.22: Normalized AE events during the fatigue test for C.2.1.

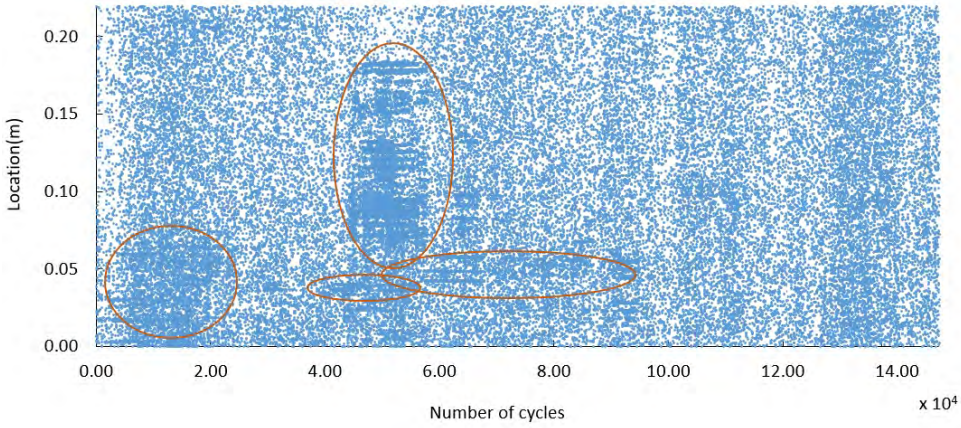


Figure 4.23: Spatial distribution of AE events during fatigue life, for C.2.1.

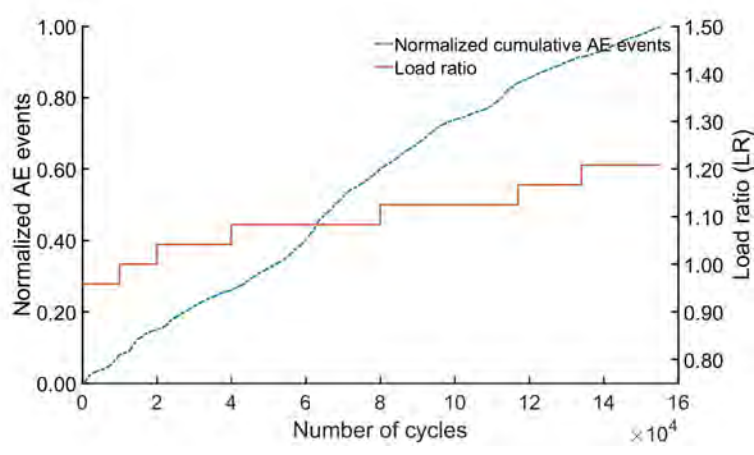


Figure 4.24: As figure 4.22 but for C2.2.

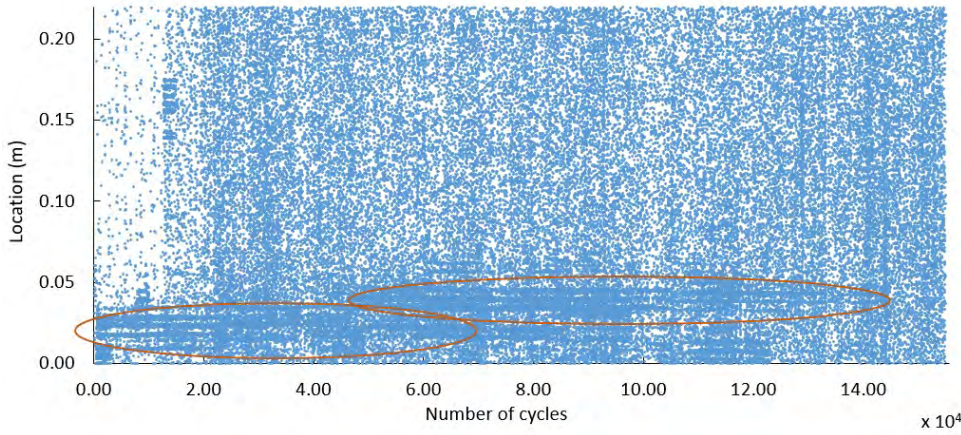


Figure 4.25: As figure 4.23 but for C.2.2.

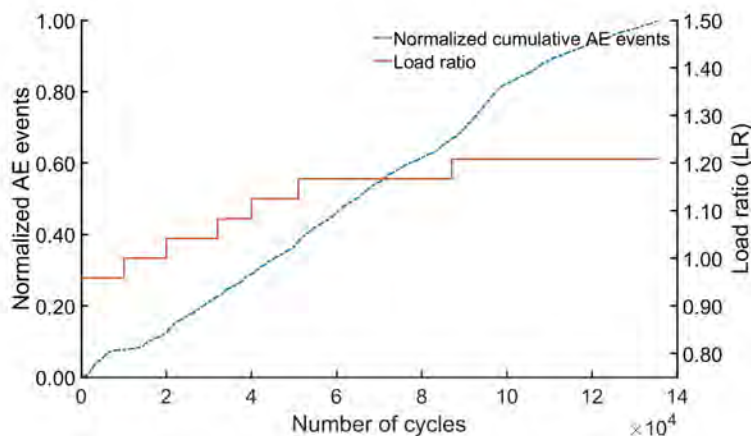


Figure 4.26: As figure 4.22 but for C.2.3.

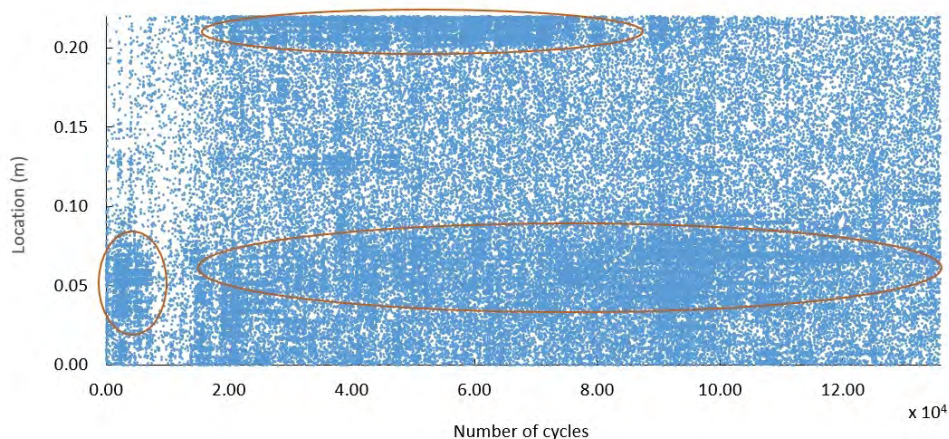


Figure 4.27: As figure 4.23 but for C.2.3.

CASE 3 IMPACT

Figures 4.28 to 4.32 show the corresponding results for the the test specimens subjected to the Case 3 energy impact. For C.3.1 and C.3.2, damage was initiated from within the impact zone at the beginning of the fatigue test. The spatial density of AE events in this zone increases during the fatigue test, indicating the growth of damage in this zone. For C.3.3, there is no significant change in the spatial density of AE events in the impact zone, at the beginning of fatigue test as seen in Figure 4.33. However, as the number of fatigue load cycles is increased, growth of the damage in the initial impact zone can be seen. This behavior is in slight contrast to the results seen for C.3.1 and C.3.2.

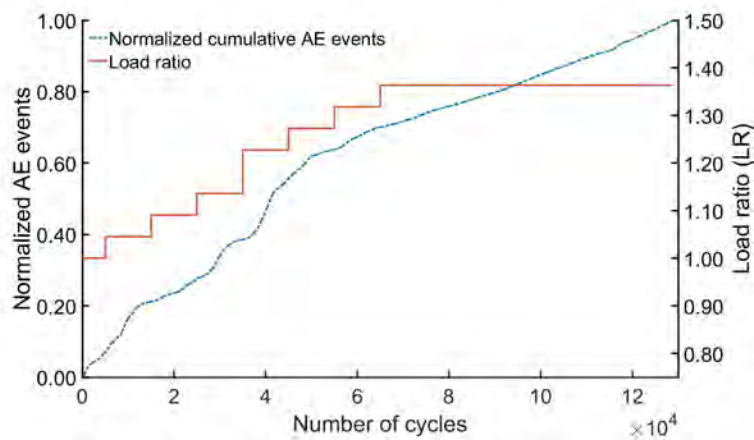


Figure 4.28: Normalized AE events during the fatigue test for C.3.1.

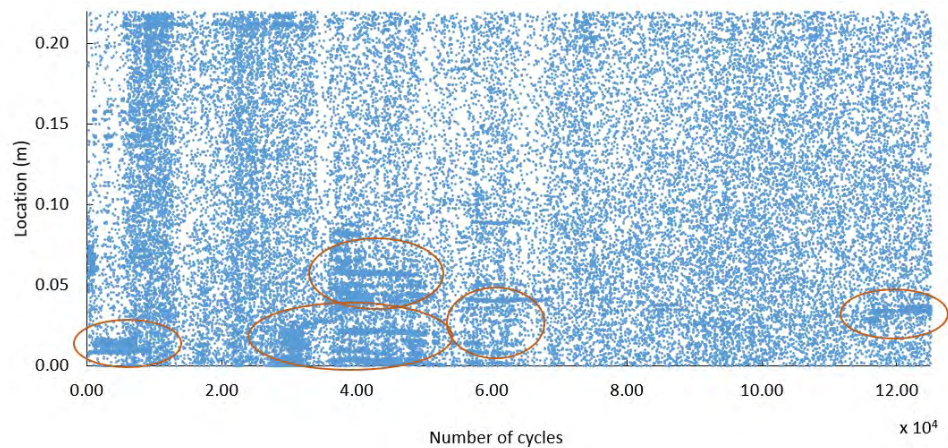


Figure 4.29: Spatial distribution of AE events during the fatigue test for C.3.1.

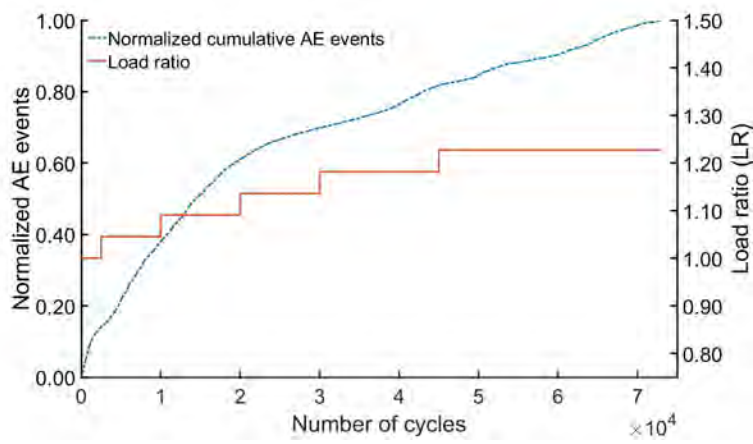


Figure 4.30: As figure 4.28 but for the C.3.2.

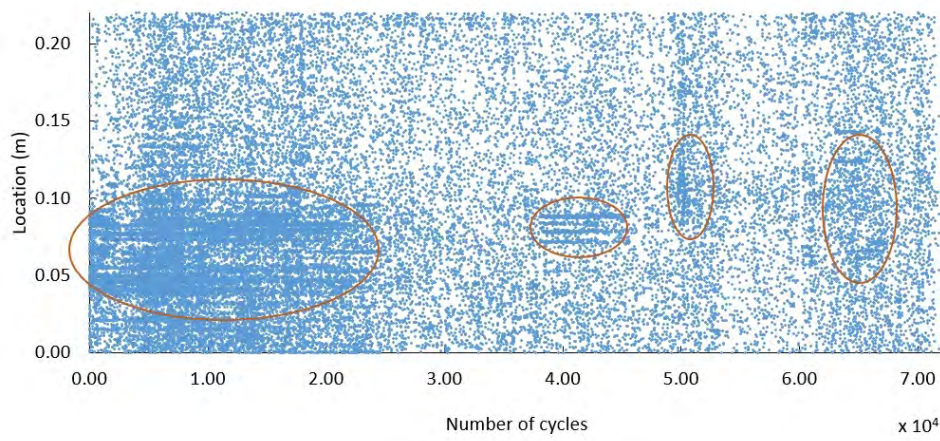


Figure 4.31: As figure 4.29 but for the C.3.2.

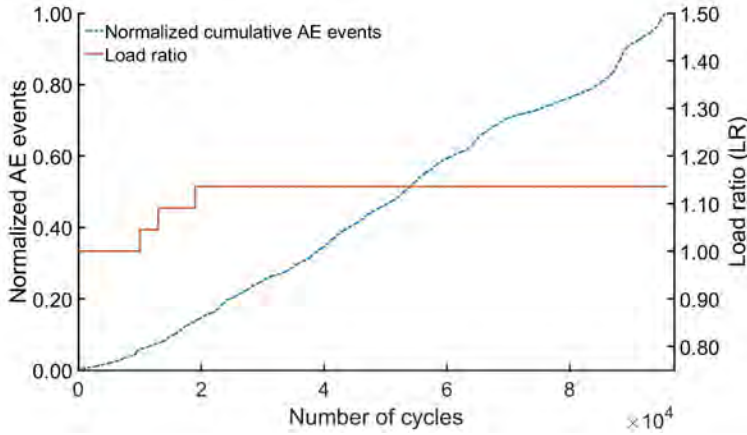


Figure 4.32: As figure 4.28 but for C.3.3.

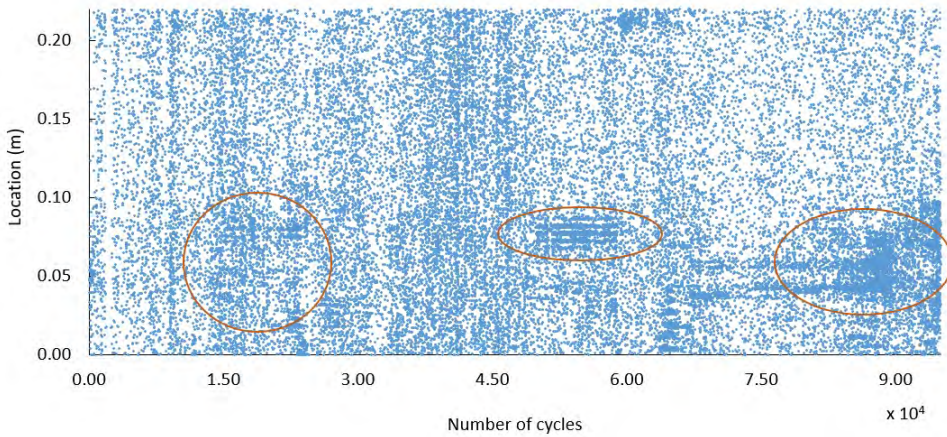


Figure 4.33: As figure 4.29 but for the C.3.3.

SUMMARY OF THE ANALYSIS OF THE AE EVENT DISTRIBUTION

When analysing the spatial density of AE events for the three different test cases, damaged sections of the test specimens could clearly be seen. The highest density of AE events showed the most damaged sections of each test specimen. For the Case 1 impact, damage accumulation is seen to be more or less spatially uniform, however, for Cases 2 and 3, damage accumulation is clearly associated with the initial impact damage zone. Although, the spatial distribution of AE events does not completely match the visible damage seen in Section 4.5.1, it does identify those areas most affected by damage during the fatigue tension tests.

4.6. CONCLUSION

In this study, the effect of three levels of energy impact on the fatigue damage accumulation process for a thick adhesive joint representative of a spar cap to the shear-web adhesive joint of a wind turbine blade has been investigated. An acoustic emission technique has been used to detect early damage and monitor the further accumulation of fatigue damage during a number of fatigue tests.

For the test specimens exposed to Case 1 impact with an average energy of 16.3 J, the fatigue damage accumulation process was not really influenced by the size and location of the impact damage. For test specimens exposed to Case 2 and Case 3 impacts with average energies of 23.7 J and 32.1 J respectively, the fatigue damage accumulation process was clearly influenced by the size and location of the impact damage. For these test specimens, higher crack density, greater de-lamination and de-bonding of adhesive from the laminate can be seen at the impact zone during the fatigue damage accumulation process. In addition, for the test specimens subjected to the Case 3 impact, the delamination of the impact zone grows more extensively and faster through the test specimens than for the other impact cases.

The acoustic emission technique could detect damage in the impact zone during the early phases of the fatigue test for the test specimens subjected to Case 2 and Case 3 impacts. For the test specimen subjected to Case 1 impact, the acoustic emission technique did not detect damage in the impact zone in the early phase of the fatigue test. By contrast, other sections of the test specimens were seen to experience more damage during the tests.

The acoustic emission technique could show the accumulation of fatigue damage during the fatigue test in certain sections of the test specimens. For the test specimens subjected to Case 2 and Case 3 impacts, the acoustic emission technique also showed that the fatigue damage accumulation occurred in the vicinity of the impact zone during the full fatigue test.

5

INFRARED THERMOGRAPHY ANALYSIS

This chapter presents a passive infrared thermography analysis to characterize fatigue damage in a test specimen representative of a spar cap-shear web adhesively-bonded connection in a wind turbine blade. Temperature is measured during a fatigue tension test using an infrared camera and the measurements are used to estimate changes to the damping properties of the joint. The changes are correlated to the level of damage.

Part of this chapter has been published in the paper:

S. Khoshmanesh, S.J. Watson, D. Zarouchas, The effect of the fatigue damage accumulation process on the damping and stiffness properties of adhesively bonded composite structures, Compos Struct, 287, 2022.

5.1. INTRODUCTION

Infrared thermography is a health monitoring technique that can be used to characterize fatigue damage in a structure by measuring its surface temperature.

An object at a temperature above absolute zero (-273°C) emits electromagnetic radiation in the infrared (IR) portion of the spectrum, i.e. from 1 to $1000\text{ }\mu\text{m}$.

Infrared thermography (IRT) is a non-contact, non-intrusive technique, which is used to infer the temperature of a body from the infrared radiation emitted using a radiometer to convert the radiated energy to an electronic signal and ultimately into a visible image [146].

Infrared thermography can be used in an active or passive mode in order to detect damage in a structure. In an active mode, external pulsed heat sources are used to warm up the structure. In a passive mode, no external heat source is used and measurements are made temperature changes resulting from internal heat sources, e.g. during a fatigue test. Active or passive methods can be used to detect damage in a structure, however, temperature changes observed using the passive method can be directly related to changes in the damping properties of the structure which may result from internal damage.

In Figure 5.1, a schematic of the infrared thermography technique in an active and passive mode is shown. In the active mode, two or more high-power lamps are used as the heating source. Heat of a specific peak power, frequency, period, time duration, and waveform can be produced by these high-power lamps. This is only used in the passive mode. The excitation power, time, frequency, and waveform are adjusted by a control unit to produce the desired level of heating on the surface of the test specimen. A high-performance infrared camera is used consisting of an advanced quantum well-infrared photo-detector with an adjustable frame rate to provide high-resolution images. A PC is used with appropriate software to adjust the operational parameters of the control unit and to record and process sequences of images from the infrared camera at the desired frame rate.

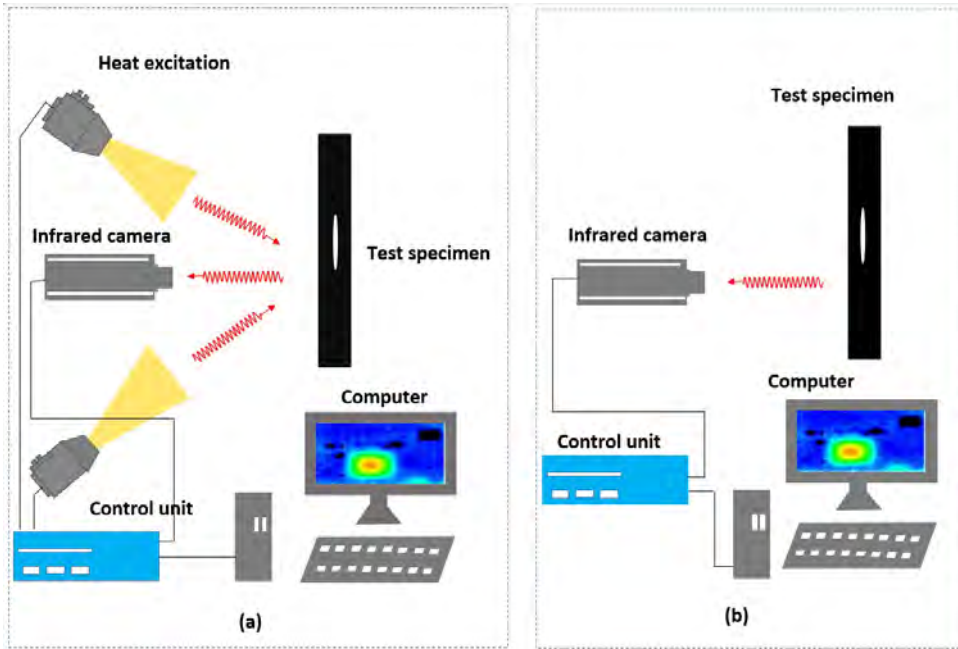


Figure 5.1: Schematic illustration of (a) active and (b) passive infrared thermography techniques.

5.1.1. CHAPTER OVERVIEW

This chapter presents an analysis of fatigue damage in a shear web adhesively-bonded connection using passive infrared thermography and covers the following topics:

- An historical overview and latest developments in damage detection using infrared thermography.
- A methodology to characterize impact fatigue damage in test specimens representative of a shear web adhesively-bonded connection.
- A description of the experimental setup.
- Results, discussion, and conclusion.

5.2. LITERATURE REVIEW

5.2.1. HISTORICAL OVERVIEW

TECHNOLOGY DEVELOPMENT

The existence of infrared (IR) radiation was unknown until 1800 when Herschel conducted an experiment to measure the energy distribution in sunlight. He

built a crude monochromator and used a thermometer as a detector to measure the temperature of different wavelengths of light. [147]. After this discovery and the establishment of important laws such as Stefan-Boltzmann's Law (1884) and Planck's law (1901), the development of IR measurement techniques began [148].

Modern infrared detectors can be classified into two main types: thermal detectors and photon detectors (also called quantum detectors) [149]. In a thermal detector, incident radiation is absorbed by the detector. The radiation warms up and changes certain physical properties of the detector, leading to the generation of electrical output. As the detector surface is black, it can absorb most of the spectrum of the incident radiation and its sensitivity is not generally dependent on the wavelength [149].

Thermoelectric, pyroelectric, and bolometer detectors are commonly used. In the case of a thermoelectric detector, the absorbed heat is transferred to thermocouples which are connected in series. This is the oldest type of detector. For a pyroelectric detector, the absorbed heat is transferred to crystalline materials that generate a temporary voltage when they are heated or cooled. For bolometers, the absorbed heat is transferred to a strip of metal attached to the absorber surface. Heating or cooling changes the resistance of this strip and this change is used to measure the temperature. To make each detector sensitive to incident radiation, the detector surface is attached to a thermal reservoir through a conductive link. The sensitivity of the detector then depends on the conductivity of this link [150].

In photon detectors, radiation is absorbed within the material which excites electrons, and increases their energy level, leading to the generation of an electrical signal. Quantum detectors have a higher sensitivity and a slower response time than thermal detectors and require significant cooling.

Based on the materials used, detectors can be tailored to absorb only a part of the incident radiation. Such materials include lead selenide (PbSe), lead telluride (PbTe), indium antimonide (InSb), or mercury cadmium telluride (HgCdTe) [151].

The history of the development of materials for IR detection are shown in figure 5.2

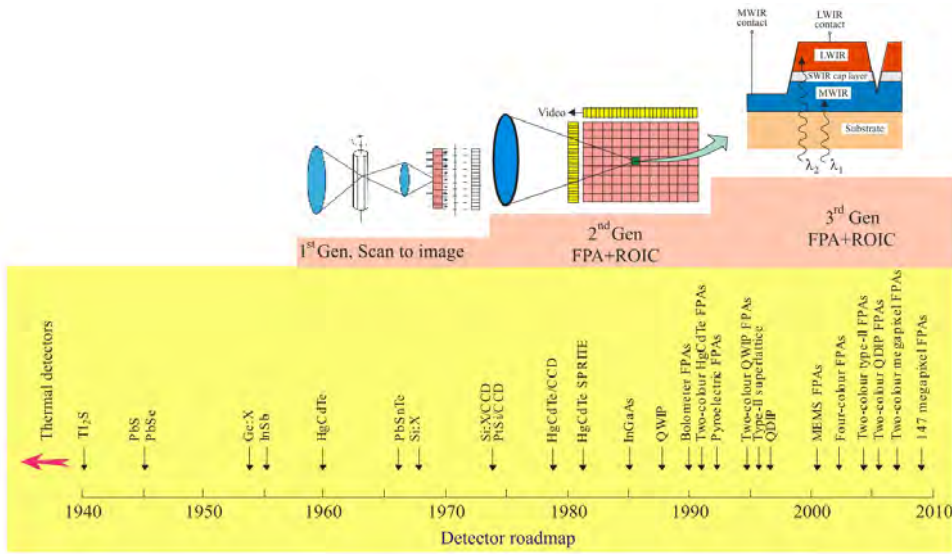


Figure 5.2: History of the development of infrared detectors and systems. Three generation systems can be considered: 1st Gen (scanning systems), 2nd Gen (staring systems, electronically scanned) and 3rd Gen (multicolour functionality and other on-chip functions) [149]

After the discovery of the transistor in 1947 and the emergence of the first cryogenic cooled IR detectors, IR thermography evolved [152]. The discovery of HgCdTe, a chemical compound of cadmium telluride (CdTe) and mercury telluride (HgTe) alloy by Lawson and coworkers in 1959, allowed IR technology to be developed for broader applications. The compound, HgCdTe, by adjusting the amount of cadmium (Cd), can be tuned to absorb the desired infrared wavelength of incident radiation, from the short-wave infrared to the very long-wave infrared regions [153]. This technological development in detectors led to the availability of the first (1965) commercial IR cameras featuring a single detector coupled to an optical-mechanical scanning mechanism to acquire the scene images.

As arrays of detectors enhanced sensitivity, the first bidimensional arrays were produced in the 1970-1980s. Cooled Focal Plane Arrays (FPAs) with more pixels appeared in the 1990s on the market (today, the largest arrays are 2048 × 2048) [152]. In the same period, uncooled FPA cameras with microbolometer detectors giving acceptable performance appeared on the market. In comparison with cooled FPAs, uncooled FPA IR cameras had a lower cost as they had no need for a cryogenic cooling unit. However, they had the drawback of a slower response. Nevertheless, these thermal detectors were useful, i.e., for scanning 2D electronic arrays [147].

Table 5.1: History of IR development, [152]

Date	IR event
1800	In England, William Herschel discovers IR rays
1833	Development of a thermopile consisting of 10 in-line Sb-Bi thermal pairs by L. Nobili and M. Melloni
1835	Formulation of the hypothesis that light and electromagnetic radiation are of the same nature by A. M. Ampere
1859	Relationship between absorption and emission by G. Kirchoff
1864	Theory of electromagnetic radiation by J.C. Maxwell
1873	Discovery of photoconductive effect in selenium by W. Smith
1880	Study of absorption characteristics of the atmosphere through a Pt bolometer resistance by S.P. Langley
1883	Study of transmission characteristics of IR-transparent materials by M. Melloni
1884	Thermodynamic derivation of the Stefan law by L. Boltzmann
1887	Observation of photoelectric effect in the ultraviolet by H. Hertz
1890	J. Elster and H. Geitel constructed a photoemissive detector consisting of an alkali-metal cathode
1894–1900	Derivation of the wavelength relation of blackbody radiation by J.W. Rayleigh and W. Wien
1900	Discovery of quantum properties of light by M. Planck
1903	Temperature measurements of stars and planets using IR radiometry and spectrometry by W.W. Coblentz
1917	T.W. Case developed the first IR photoconductor from substance composed of thallium and sulphur
1930	IR direction finders based on PbS quantum detectors in the wavelength range 1.5–3.0 μm for military applications (Gudden, Gorlich and Kutscher) increased range in World War II to 30 km for ships and 7 km for tanks (3–5 μm)
1934	First IR image converter
1955	Mass production start of IR seeker heads for IR guided rockets begins in the USA (PbS and PbTe detectors, later InSb detectors for Sidewinder rockets)
1957	Discovery of HgCdTe ternary alloy as IR detector material by W.D. Lawson, S. Nelson, and A.S. Young
1961	Discovery of extrinsic Ge:Hg and its application (linear array) in the first LWIR FLIR systems
1977	Discovery of the broken-gap type-II InAs/GaSb superlattices by G.A. Sai-Halasz, R. Tsu and L. Esaki
1980	Development and production of second generation systems [cameras fitted with hybrid HgCdTe (InSb)/ Si(readout) FPA s]. First demonstration of two-colour back-to-back SWIR GaInAsP detector by J.C. Campbell, A.G. Dental, T.P. Lee, and C.A. Burrus
1985	Development and mass production of cameras fitted with Schottky diode FPA s (platinum silicide)
1990	Development and production of quantum well IR photoconductor (QWIP) hybrid 2nd generation systems
1995	Production begins of IR cameras with uncooled FPAs (microbolometer-based and pyroelectric FPA s)
2000	Development and production of third-generation IR systems
2000–2010	Multicolour functionality and other on-chip functions (Mems FPA s, Two-colour type-II FPA s, two-colour QDIP FPA s, two-color megapixel FPA s, 147-megapixel FPA s)
2013	On February 14, researchers developed a neural implant that gives rats the ability to sense IR light which for the first time provides living creatures with new abilities instead of simply replacing or augmenting existing abilities

Further development in uncooled IR arrays based on thermal detectors, which have the capability to work at room temperature, gave rise to a revolution in thermal imaging. IR photon detector technology also experienced rapid development in the last decades of the twentieth century. Two types of IR detector in particular underwent significant development, namely: indium antimonide (InSb) and mercury cadmium telluride (HgCdTe-based). They are now commercially available, and their development has continued over the last few years [154]. In addition, more recent efforts have improved the sensitivity of room-temperature devices [155, 156]. The history of IR development is shown in the Table 5.1.

APPLICATIONS

Early application of IR technology dates back to the nineteenth century through the work of researchers such as Vernotte around 1937. He was a pioneer in making measurements using single-sided materials with thermophysical properties, and defined the notion of effusivity (thermal responsivity of a material) [157]. This term is now used in thermal non-destructive testing (TNDT).

In 1959, Hardy et al. measured the effusivity of skin on the forehead of a patient by using single-sided pulsed infrared radiometric measurements [158]. Cowan in 1961, described a method for measuring the thermal diffusivity of metal at high temperature by using modulated-heating radiometry [159]. Rudkin et al. in 1962 measured thermal diffusivity of metal at high temperature by double-sided, rear-face active IR pulsed radiometry [160]. These three researchers had a significant impact on the development of IR technology.

In 1960 With the appearance of radiometric IR images from AGA, Sweden (later AGEMA Infrared Systems and now FLIR Systems, USA), IR thermography was used for inspection of electrical installations, radio-electronic components, and buildings.

Around 1970, thermal non-destructive testing (TNDT) started to become established. This led to the formation of an IR committee by the American Society for TNDT and the publishing of transactions dedicated to this topic. These efforts of the American Society for TNDT turned the inspection of aerospace materials into the most important application of active TNDT, [161].

The ability of IR thermography to detect defects in structures inspired many researchers to use this technique for health monitoring. Clark et al. in 2003 identified areas of delamination in a concrete bridge structure and investigated the internal structure of a masonry bridge using IR thermography [162]. Maierhofer et al., in 2002, used transient thermography for structural investigation of concrete and composites close to the surface [163]. They later used IR impulse thermography for detection of near-surface voids in concrete structures [164].

5.2.2. INFRARED THERMOGRAPHY ANALYSIS APPLIED TO COMPOSITE MATERIALS

The work of Milne et al. in 1983 can be considered as pioneering research in the detection of defects in composite materials using thermal pulsed video thermog-

raphy [165].

Bai et al. (2000) conducted experiments to analyze defects of various sizes and depths below a test surface in a carbon fiber reinforced composite specimen using lock-in thermography, [166]. In lock-in thermography, a pulsed heat source is used to warm up a structure and the pulse frequency is synchronized to the camera's acquisition rate. Based on the results, the sensitivity of lock-in thermography to defect detection was found to be dependent on the pulse frequency, the intensity of the heat source, the resolution of the lock-in system, and the distance between the IR camera and the object. Bai et al. (2001) evaluated the use of lock-in thermography for the detection of defects in composite plates in a natural ambient environment. [167] which also confirmed its effectiveness. Ibarra-Castanedo et al. (2004) investigated various methods of data analysis required for defect detection using active infrared thermography [168]. Avdelidis et al. investigated the application of transient TNDT to the monitoring of aircraft composites [169].

Meola et al. (2004) used active infrared thermography to analyze substrate and adhesive defects in bonded structures. They used pulsed and lock-in thermography to assess the defects in the bonded structures, including adhesively-bonded aluminum joints with or without surface treatment and glass-reinforced epoxy composites and carbon-reinforced epoxy composites with or without plasma treatment [170]. They concluded that pulsed and lock-in thermography are both capable of visualizing inhomogeneities in bulk materials, as well as debonding, delamination, flaws, and embedded foreign objects in the bonded structures.

Ibarra-Castanedo et al. (2007) discussed three data processing techniques for the detection of defects in aerospace composite structures using pulsed infrared thermography [171]. Montanini et al. (2010) used lock-in and pulsed phase infrared thermography to determine quantitatively subsurface defects in a reference specimen made of plexiglas [172]. In pulsed phase thermography a pulse with a mix frequencies is used. Lahiri et al. (2012) used lock-in infrared thermography to quantify defects in specimens of glass fiber reinforced polymer [173].

Harizi et al. in 2014 assessed mechanical damage to fiber-reinforced polymer composites during static tensile loading using passive infrared thermography. They used the increase in local temperature and sudden change in thermo-elastic coefficient to assess mechanical damage [174]. Zheng et al. (2015) used pulsed thermography to detect damage in carbon fiber-reinforced polymer material by thermographic signal reconstruction and utilization of a penalized least squares method [175]. Chrysafi et al. (2017) examined the efficiency of various mathematical methods in active infrared thermographic data processing with respect to the thermal excitation method and the type of artificial defect in CFRP specimens [176].

Zalameda et al. in 2019 and 2021, studied damage detection in composite single stringer hat stiffened panels under quasi-static and fatigue loading using active IR thermography [177, 178] using sudden changes in temperature of thermal maps to analyze the damage.

Most of the work to date in relation to TNDT is based on active external heating

either from artificial sources or sunlight. This is a significant limiting factor for continuous health monitoring of a structure. Passive thermography does not rely on any external heat source, and therefore, could be used to continuously monitor the state of health of a structure which is being fatigued in some way so that internal heating occurs, e.g. the blade of a wind turbine in operation.

The damping mechanism and how to calculate damping in a composite material is different from metal. The dominant damping mechanism in a composite material is related to the visco-elastic behaviour of the matrix and/or the fibres. In previous work, passive thermography has been used to calculate damping in steel structures. Audenino et al. (2003) investigated the correlation between thermography and internal damping in metals, and proposed a theoretical relationship between temperature increase and specific damping [179]. Cura et al. (2012) measured heat dissipation in steel during high cycle fatigue tests using infrared thermography to correlate the fatigue life with heat dissipation [180].

This study uses passive infrared thermography to characterize the effect of initial impact damage on the fatigue damage propagation to a test specimen representative of spar cap to shear web adhesively-bonded connection of a wind turbine blade. The work relies on the estimation of material damping using infrared thermography to characterize the damage.

Effect of different types of damages on damping in this adhesively-bonded connection is discussed.

5.3. METHODOLOGY

This methodology explains how to determine the material damping in a test specimen representative of a spar cap-shear web adhesively bonded connection subjected to fatigue tension testing. To investigate fatigue damage propagation following impact damage in an adhesively-bonded connection, test specimens are exposed to three levels of impact (low, medium, and high energy levels) as explained in section 4.4.2. The test specimens are subjected to fatigue tension tests with a stress ratio, R (ratio of minimum load amplitude to maximum load amplitude) equal to 0.1 and a fatigue cycling frequency of 3 Hz. The temperature of the test specimens is continuously measured during the fatigue life by using an infrared camera.

When a material is subjected to a cyclic fatigue load, energy is dissipated inside the material in the form of heat due to structural damping. This increases the temperature of the material, which can be measured using a thermographic camera sensitive to infrared light. The increase in temperature can be related to the dissipation of energy in order to estimate changes in material damping. In viscoelastic materials, the dissipation of energy per unit volume due to damping during one loading cycle can be written as [181]:

$$W_d = \pi \tan(\delta) \left(\frac{\sigma^2}{E} \right) \quad (5.1)$$

where W_d and $\tan(\delta)$ are the dissipation of energy and loss factor respectively, E

is the elastic modulus of the material and σ is the stress amplitude defined by:

$$\sigma = \frac{\sigma_{max} - \sigma_{min}}{2} \quad (5.2)$$

where σ_{max} and σ_{min} are the maximum and minimum stress, respectively, during the fatigue tension test.

To relate the dissipation of energy to the temperature T of the test specimen, the heat loss/gain within the test specimen should be known. The heat generated due to damping in the test specimen is equal to the heat absorbed in the test specimen plus heat removed from the surface of the test specimen by natural convection. Because the thickness and width of the test specimen are much smaller than the length of the test specimen, for an infinitesimal control volume of the test specimen, as shown in the figure 5.3, the heat equation can be written as:

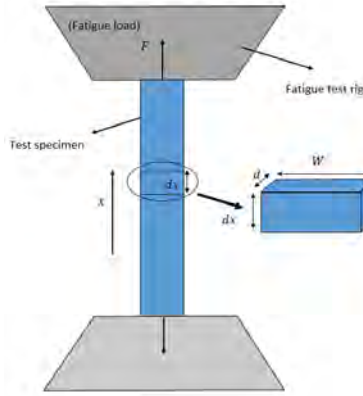


Figure 5.3: Schematic illustration of the test specimen in the fatigue test rig and the infinitesimal control volume used in the heat equation.

$$\rho C \frac{\partial T}{\partial t} + 2h \frac{(w+d)}{wd} (T - T_{am}) + K \frac{\partial^2 T}{\partial x^2} = \pi f \tan(\delta) \left(\frac{\sigma^2}{E} \right) \quad (5.3)$$

where t is time, ρ is the material density, C is the specific heat capacity of the material, K is material conductivity, f is the frequency of the fatigue test, w is the width of the test specimen, d is its thickness, T_{am} is the ambient temperature and h is the natural convection heat transfer coefficient. The heat transfer coefficient h is calculated using the Nusselt number, Nu :

$$h = \frac{Nu l}{K_{air}} \quad (5.4)$$

where l is the length of the test specimen and K_{air} is the conductivity of air. The Nusselt number is dependent on the Rayleigh and Prandtl numbers (Ra and Pr ,

respectively) and for engineering applications, the following relationship can be used based on vertical plates[182]:

$$Nu = (0.825 + \frac{0.387Ra^{\frac{1}{6}}}{[1 + (0.492/Pr)^{\frac{9}{16}}]^{\frac{8}{27}}})^2 \quad (5.5)$$

where the Rayleigh number is given by:

$$Ra = \frac{g\beta(T_s - T_{am})l^3}{\nu a}, \quad T_s = \frac{T_i + T_f}{2} \quad (5.6)$$

where g is gravitational acceleration, and β , ν and a are the thermal expansion coefficient, kinematic viscosity and thermal diffusivity of air, respectively. T_s is the surface temperature of the test specimen based on an average during the fatigue test where T_i and T_f are the initial and final surface temperatures, respectively. The Prandtl number is defined as:

$$Pr = \frac{\nu}{a} \quad (5.7)$$

5.4. EXPERIMENTAL SET UP

Four sets of test specimens (each set included three test specimens) representative of no impact, low, medium, and high energy level impact were subjected to a tension fatigue test using a 100 kN hydraulic fatigue rig under load control, as shown in Figure 5.4. Figure 5.4 shows the passive infrared thermography test set-up.

To calculate the material damping properties of the specimens using thermography, a FLIR A655sc type infrared camera was used. The camera is equipped with an uncooled Vanadium Oxide (VoX) microbolometer detector that produces thermal images of 640 x 480 pixels. The device is capable of detecting temperature differences as small as 50mK. The temperature of each test specimen is continuously measured during its fatigue life, and the increase in temperature is associated with the heat generated inside the test specimen to estimate the loss factor as described in section 5.3.

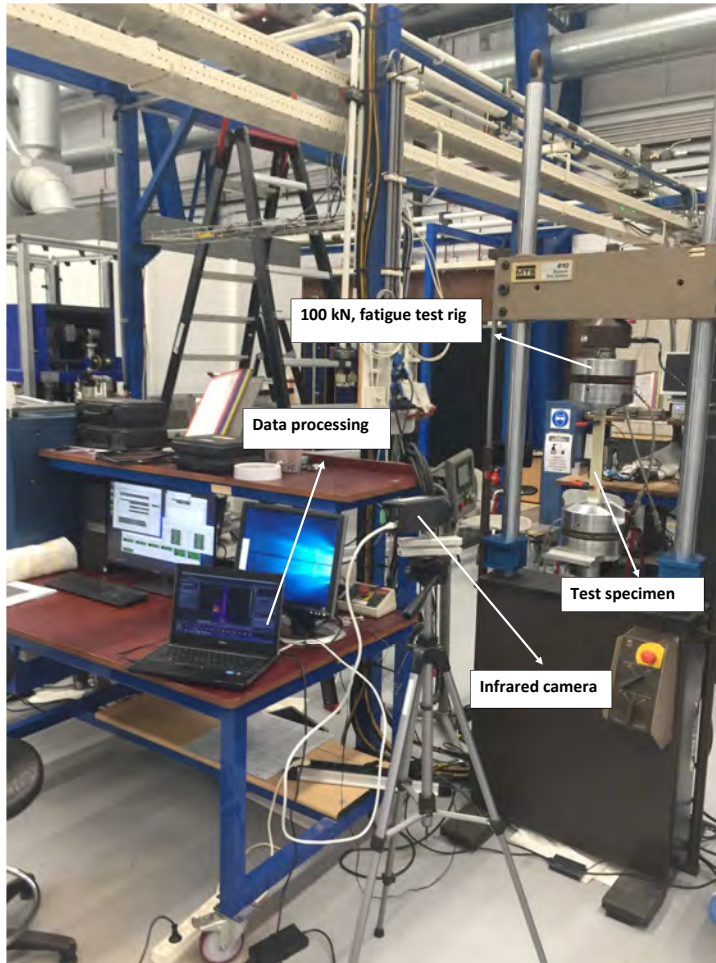


Figure 5.4: Passive infrared thermography test set up.

5.5. RESULTS AND DISCUSSION

This section presents and discusses the results of the fatigue damage thermography analysis of the test specimens subjected to no impact, low, medium, and high energy level impact. To analyze the effect of impact on damage propagation, the loss factor in the impact zone of the test specimens is calculated. To do this, test specimens with a length of 22 cm, as shown in Figure 5.5, are divided into 11 elements. The impact zone consists of three elements (elements 2,3 and 4). Using equation 5.3 and the measured average surface temperature of these elements, the loss factors of the elements in the impact zones are calculated. For the case of non-impact, as the damage is distributed evenly within the test spec-

imens, the overall loss factor of these specimens is used to characterize damage. This is calculated by using Equation 5.3 and the average surface temperature of the test specimens.

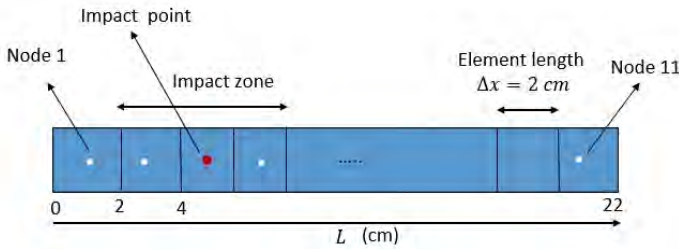


Figure 5.5: Schematic illustration of a test specimen divided into a number of elements used for thermography analysis.

5.5.1. NO IMPACT

During the fatigue test, the surface temperature of the test specimens is measured continuously by the infrared camera. Figure 5.6 shows temperature maps measured using the infrared camera and pictures taken in visible light of one of the test specimens at different stages during the fatigue test.

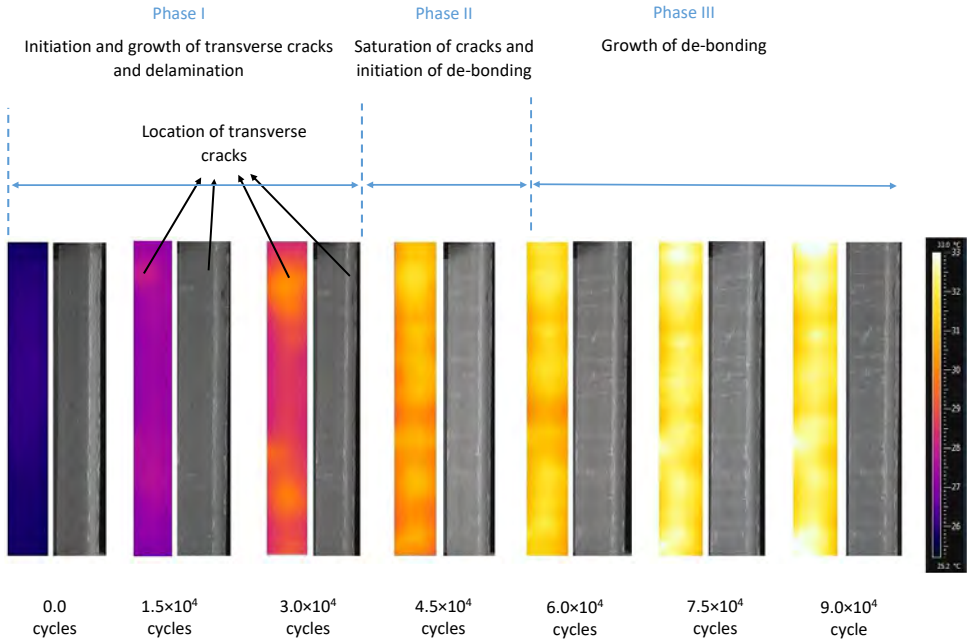


Figure 5.6: Temperature of one of the test specimens at different stages of the fatigue test. Pictures taken in visible light are shown alongside for comparison.

The different stages of damage and their locations can be seen. The temperature increases during the fatigue test, and after 1.5×10^4 load cycles, the first sign of cracks can be seen by looking at local extremes of temperature (hot spots) shown by arrows in Figure 5.6. The cracks in the adhesive are transverse cracks, and they grow until they reach the interface between laminate and adhesive. This causes the de-bonding of laminate from adhesive. These de-bonded areas (seen as white lines in Figure 5.6) are the dominant sources of increased damping and, subsequently, the temperature (seen as hot spots in Figure 5.6). As the fatigue test progresses, the number and temperature of the hot spots increases. This trend continues until 4.5×10^4 load cycles when the number of hot spots is almost equally distributed throughout the length of the specimen. This implies that the crack saturation (Phase II) has been reached. As the number of load cycles increases, crack lengths increase, and the de-bonding of the laminate from the adhesive grows further. This increases the temperature in the specimens.

To better illustrate the increase in the number of cracks until saturation occurs, the temperature profile across a line through the middle of a test specimen is plotted in Figure 5.7. Local extremes in temperature indicate the locations of

cracks which clearly grow in number and severity as the test progresses and the number of cracks reaches saturation. Again, the results presented are for one of the specimens, but the same trend is seen for all.

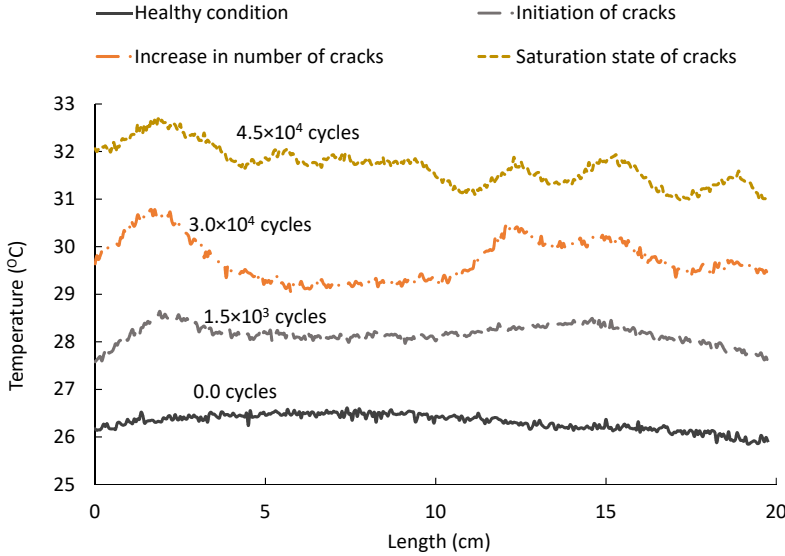


Figure 5.7: Temperature profile across the mid-line of a test specimen at different stages of the fatigue test.

To calculate the damping, firstly, the reference damping corresponding to the healthy test specimen is calculated. This can be done by fitting the loss factor to the average surface temperature of the test specimen up until 2×10^4 load cycles during which little damage has occurred. The results of one test specimen have been shown in Figure 5.8. During the first 2×10^4 load cycles, the specimen reaches an approximate steady state temperature of 28.3°C , where the heat generated in the test specimen is in balance with the heat removed from the surface of the test specimen by natural convection. The loss factor which gives the best fit to this measured temperature is about $\delta = 0.0013$.

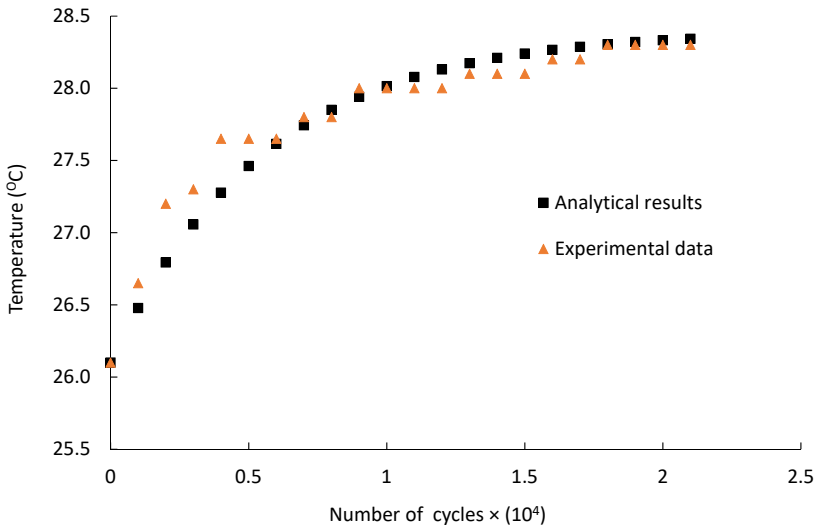


Figure 5.8: Experimentally and theoretically fitted temperature values based on thermographic measurements for an assumed healthy test specimen where $\delta = 0.0013$ and excitation frequency of $f = 3$ Hz.

Figure 5.9 shows for the three test specimens the change in average temperature during the fatigue test. Using the temperature values in Figure 5.9, the overall loss factor during the different phases of damage can be determined. These values are shown in Figure 5.10.

At the beginning of the test, around 1×10^4 load cycles, the overall damping in the test specimens does not change. This implies no damage in the test specimens. At around $2-3 \times 10^4$ load cycles, an increase in the overall damping can be seen, which corresponds to the initiation of early cracks and de-bonding (Phase I). Further increase in the fatigue load cycles propagates the cracks within the test specimens and increases the overall damping. This trend continues until the test specimens are saturated with cracks (Phase II). In this phase, the test specimens experience major damage, as, in addition to an increase in the number of cracks, the length of transverse cracks increases, and they de-bond the adhesive from the laminate. The de-bonded areas are the main source of the increase in overall damping. After saturation of cracks, as the fatigue test continues, the crack length and subsequently de-bonded areas increase at a slower rate than in Phase II. This increases the damping but again at a rate lower than Phase II. In this phase, the rate of increase in overall damping reduces, and the damping profile tends to flatten off, as seen in Figure 5.10.

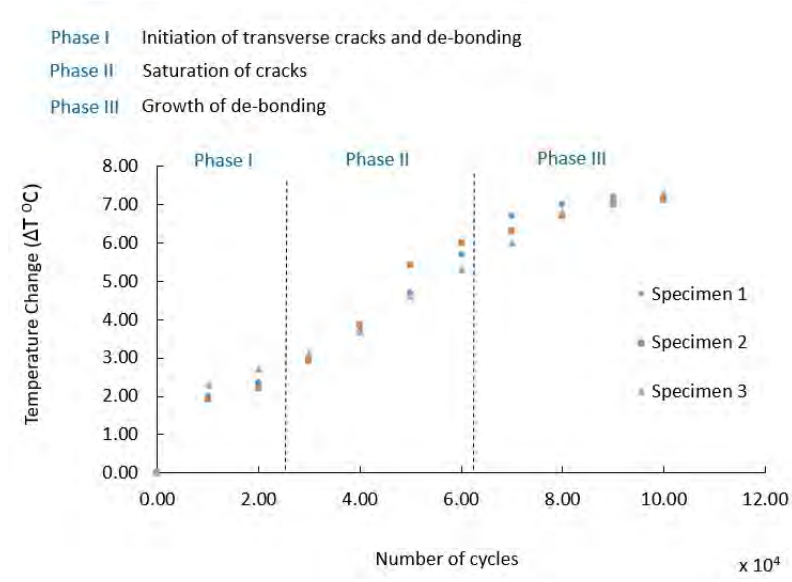


Figure 5.9: Change in average surface temperature of the test specimen during its fatigue life.

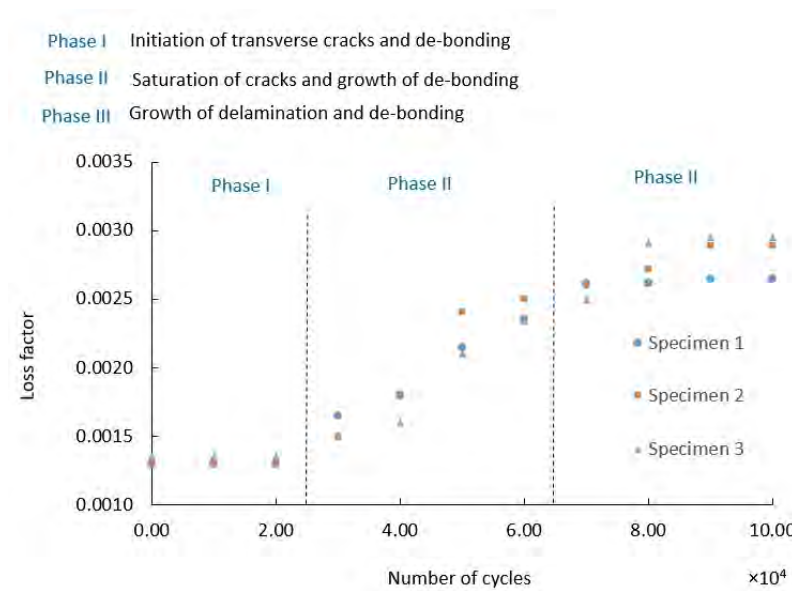


Figure 5.10: The loss factor during the fatigue tests for the three test specimens inferred from thermographic measurements.

5.5.2. LOW LEVEL OF ENERGY IMPACT

Figure 5.11 shows temperature maps measured using the infrared camera and pictures taken in visible light of one of the test specimens subjected to a low level of energy impact at different stages during the fatigue test. The location of impact is shown by an arrow. As seen from this figure, the initiation, and propagation of hot spots as representative of damage and its propagation, are the same as the non-impact specimens. This shows the low-level energy impact does not influence the propagation of damage.

Figure 5.12, 5.14, and 5.16 show the change in the average temperature of three elements in the impact zone of the test specimens during the fatigue test. Using the temperature values in these figures, the loss factor for the three elements at the impact zone of these specimens, as shown in Figures 5.13, 5.15 and 5.17 can be determined.

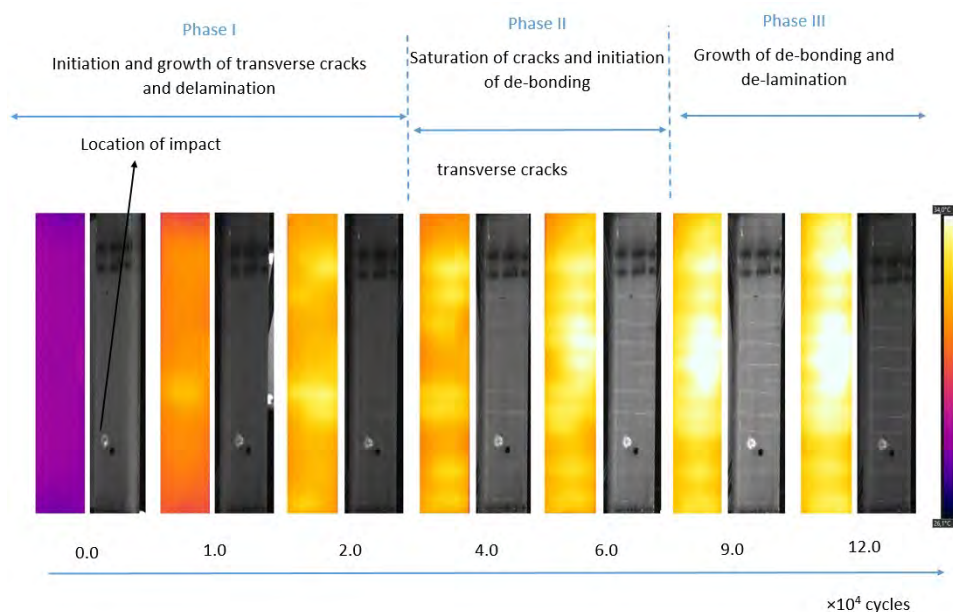


Figure 5.11: Temperature of one of the test specimens subjected to low-level of energy impact at different stages of the fatigue test. Pictures taken in visible light are shown alongside for comparison.

The loss factor in three test specimens follows the same pattern. At the beginning of the test, until 1×10^4 load cycles, the loss factor in the impact zone (element 2, element 3, and element 4) of three test specimens does not change. At around $2 - 3 \times 10^4$ load cycles, an increase in the loss factor in the impact zones can be seen that shows the initiation of early cracks and de-bonding in the impact zones (Phase I). During Phase II of damage, similar to what was seen in the non-impact specimens, as cracks and de-bonded areas grow, the loss factor

in the impact zones keeps increasing. This increase in loss factor continues until specimens saturate with cracks (Phase II damage). During Phase III of damage, the increase in the loss factor rate reduces, and the loss factor plot tends to flat-ten off. This is due to the fact that the de-bonded areas, which are the primary source of damping, have already grown in Phase II of damage. During Phase III of damage, the de-bonded areas grow very slowly. This can be seen from Figure 5.11. The loss factor profile of test specimens subjected to the low level of energy impact are very similar to the loss factor profile of non-impact specimens. This shows that the low level of energy impact does not influence the fatigue damage propagation in these adhesive joints.

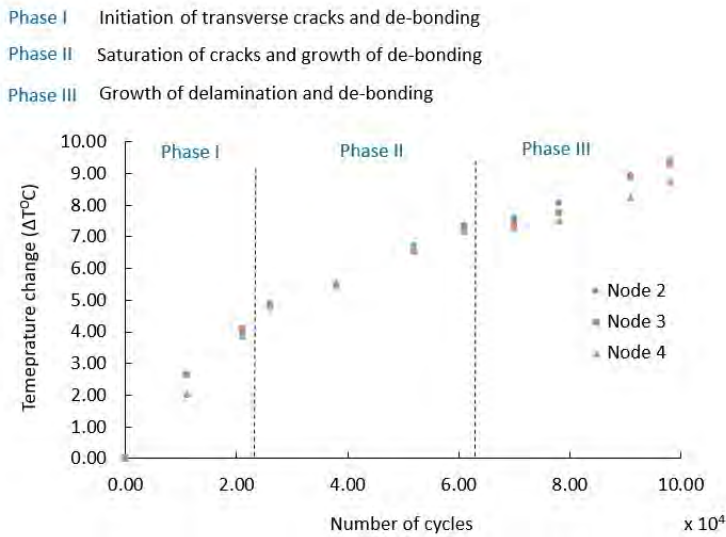


Figure 5.12: Average surface temperature of impact zone (element 2, element 3, and element 4) for the low level of energy impact and test specimen 1.

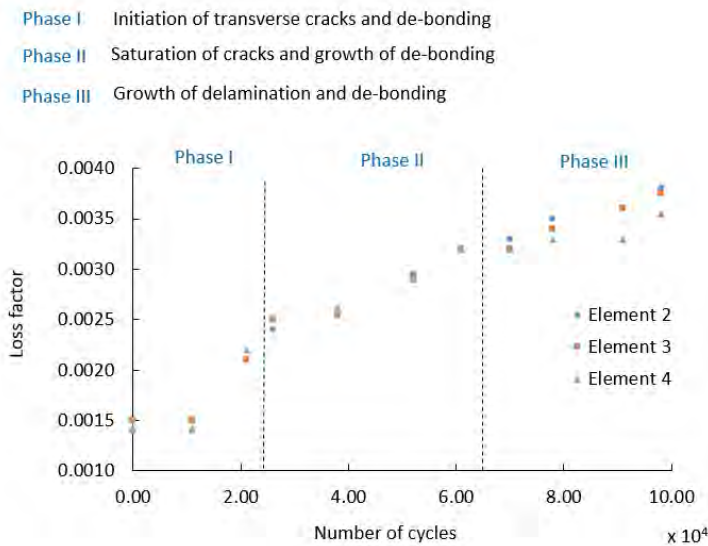


Figure 5.13: The loss factor of the impact zone (element 2, element 3, and element 4) during the fatigue tests for the low level of energy impact and test specimen 1.

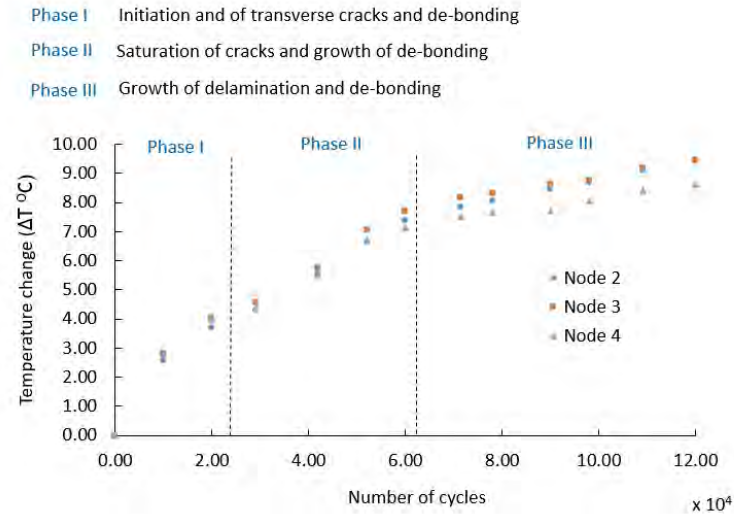


Figure 5.14: Average surface temperature of impact zone (element 2, element 3, and element 4) for the low level of energy impact and test specimen 2.

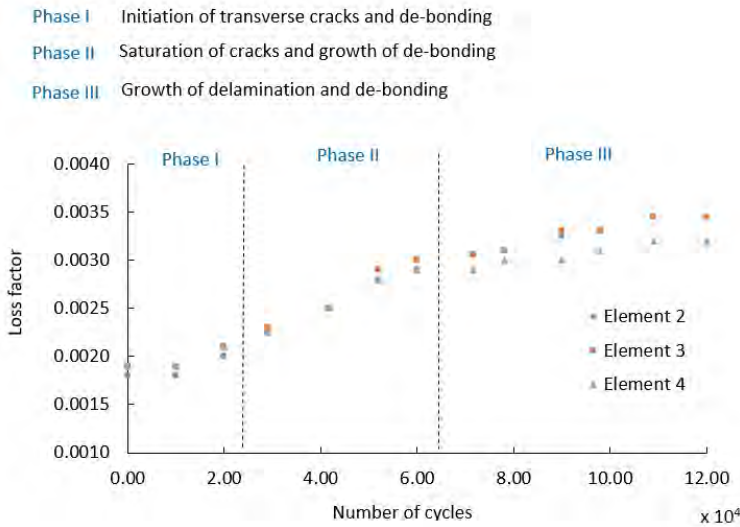


Figure 5.15: The loss factor of the impact zone (element 2, element 3, and element 4) during the fatigue tests for the low level of energy impact and test specimen 2.

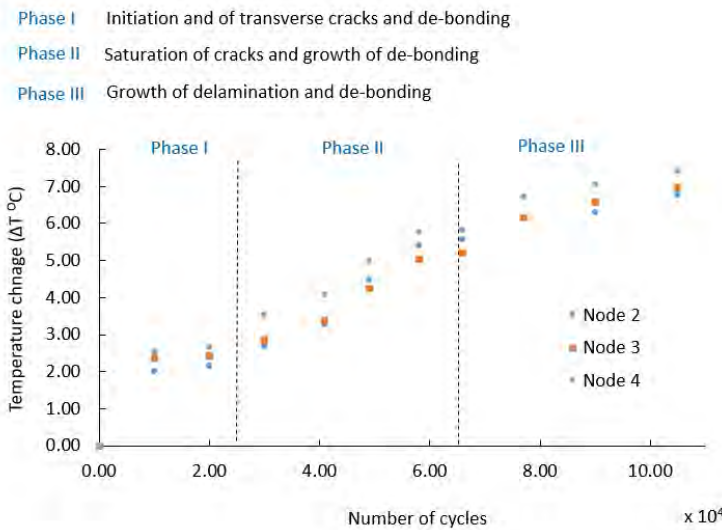


Figure 5.16: Average surface temperature of impact zone (element 2, element 3, and element 4) for the low level of energy impact and test specimen 3.

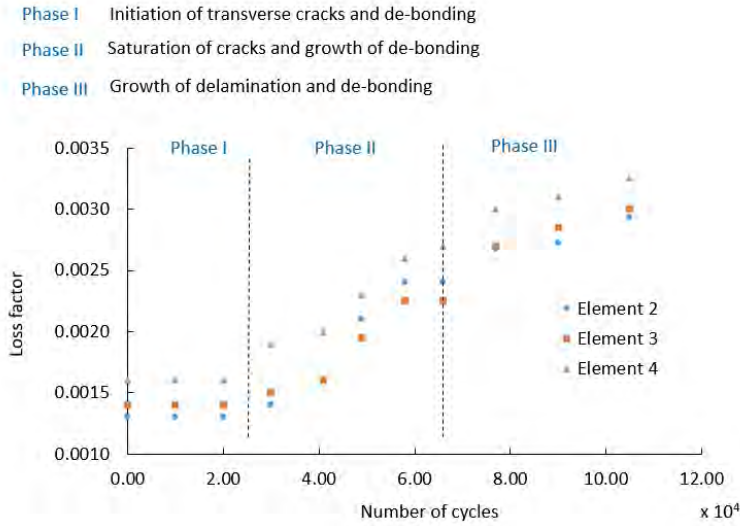


Figure 5.17: The loss factor of the impact zone (element 2, element 3, and element 4) during the fatigue tests for the low level of energy impact and test specimen 3.

5.5.3. MEDIUM LEVEL OF ENERGY IMPACT

Figure 5.18 shows temperature maps measured using the infrared camera and pictures taken in visible light of one of the test specimens subjected to a medium level of energy impact at different stages during the fatigue test. The location of impact is shown by an arrow. As seen from this figure, the first sign of hot spots as representative of damage appears in the impact zone. This is the initiation phase of damage (Phase I). As the fatigue test continues, the number of cracks in the test specimen increases and reaches the saturation level (Phase II). In comparison with a low level of energy impact, the crack density in the impact zone is higher, and the delamination area created by the impact grows during this phase. The extended area of hot spots at the impact zone shows this. During Phase III of damage, in addition to the growth of crack and de-bonding, the delamination area in the impact zone also grows.

Figure 5.19, 5.21 show the change in the average temperature of three elements in the impact zone of the test specimens during the fatigue test. Using the temperature values in these figures, the loss factor for these elements at the impact zone of test specimens, as shown in Figures 5.20, 5.22, can be determined.

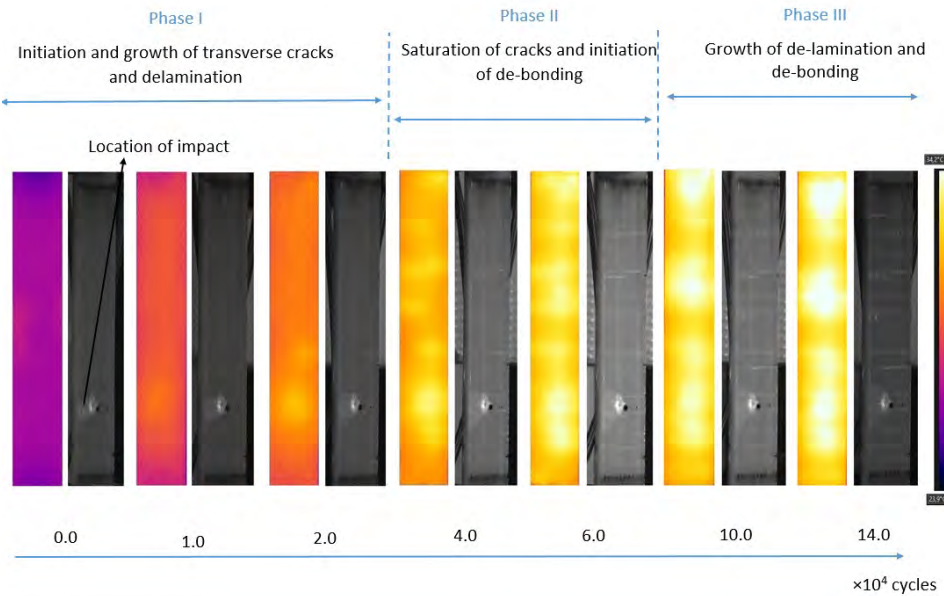


Figure 5.18: Temperature of one of the test specimens subjected to medium level of energy at different stages of the fatigue test. Pictures taken in visible light are shown alongside for comparison.

The loss factor profile of the impact zone of the test specimens in Phases I and II of damage shows a similar trend as the loss factor of test specimens subjected to the low level of energy impact. The loss factor in the impact zones of test specimens keeps increasing during Phase III of damage at a lower rate than during Phase II. The main difference between the loss factor profile for these specimens and the specimens subjected to low-level energy impact is that the loss factor increases at a higher rate during Phase III of these test specimens. This is due to delamination damage induced by impact and its growth during Phase III.

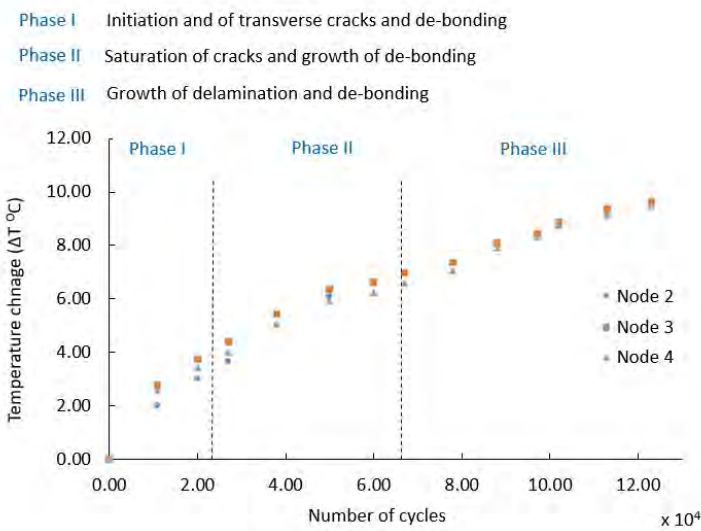


Figure 5.19: Average surface temperature of impact zone (element 2, element 3, and element 4) for the medium level of energy impact and test specimen 1.

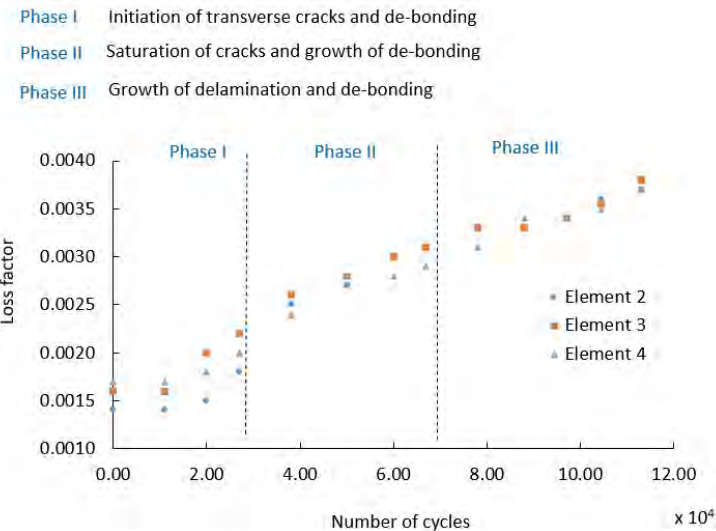


Figure 5.20: The loss factor of the impact zone (element 2, element 3, and element 4) during the fatigue tests for the medium level of energy impact and test specimen 1.

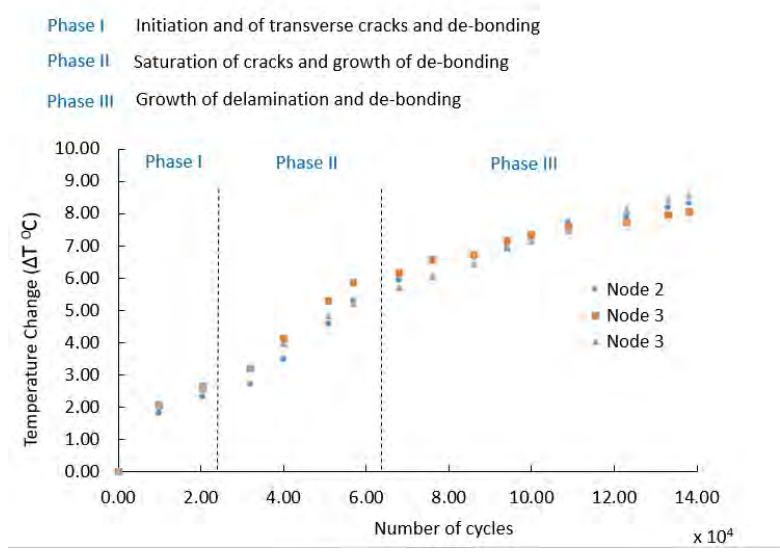


Figure 5.21: Average surface temperature of impact zone (element 2, element 3, and element 4) for the medium level of energy impact and test specimen 2.

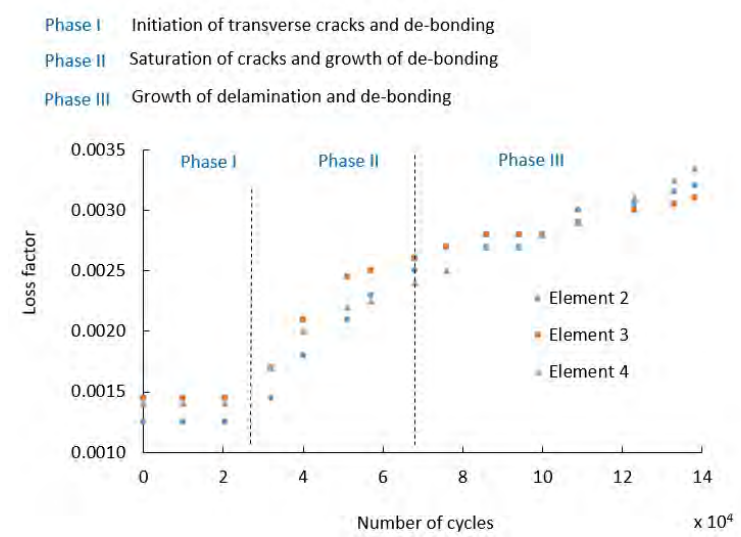


Figure 5.22: The loss factor of the impact zone (element 2, element 3, and element 4) during the fatigue tests for the medium level of energy impact and test specimen 2.

5.5.4. HIGH LEVEL OF ENERGY IMPACT

Figure 5.23 shows temperature maps measured using the infrared camera and pictures taken in visible light of one of the test specimens subjected to a high level of energy impact at different stages during the fatigue test. The location of impact is shown by an arrow. As seen from this figure, similar to the specimens subjected to a medium level of energy impact, the first sign of hot spots as representative of damage appears in the impact zone. This is the initiation phase of damage (Phase I). The damage propagation is the same as specimens subjected to a medium level of energy impact, except that the delamination area created by the impact grows at a higher rate.

Figure 5.24, 5.26, and 5.28 show the change in the average temperature of three elements in the impact zone of the test specimens during the fatigue test. Using the temperature values in these figures, the loss factor for the three elements at the impact zone of the test specimens, as shown in Figures 5.25, 5.27 and 5.29 can be determined.

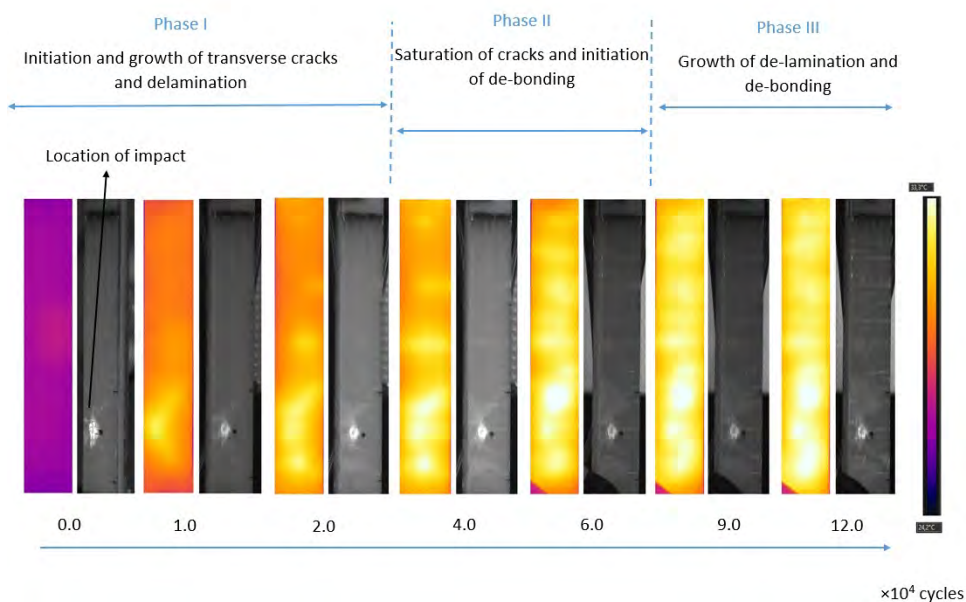


Figure 5.23: Temperature of one of the test specimens subjected to the high level of energy at different stages of the fatigue test. Pictures taken in visible light are shown alongside for comparison.

These loss factor profiles in Phases I and II of damage are similar to the loss factor of test specimens subjected to low and medium levels of energy impact. In Phase III damage, the loss factor of the impact zone of test specimen 1 and test specimen 3 increases at almost the same rate as Phase II damage. The loss factor in the impact zones of test specimen 2 increases at a higher rate

than during Phase II damage. The growth of delamination induced by the impact in the test specimens subjected to a high level of energy impact during Phase III damage is more than the test specimens subjected to the medium level of energy impact, figures 5.18 and 5.23. This is the reason that the loss factor of these specimens during Phase III damage increases at a higher rate relative to specimens subjected to a medium level of energy impact.

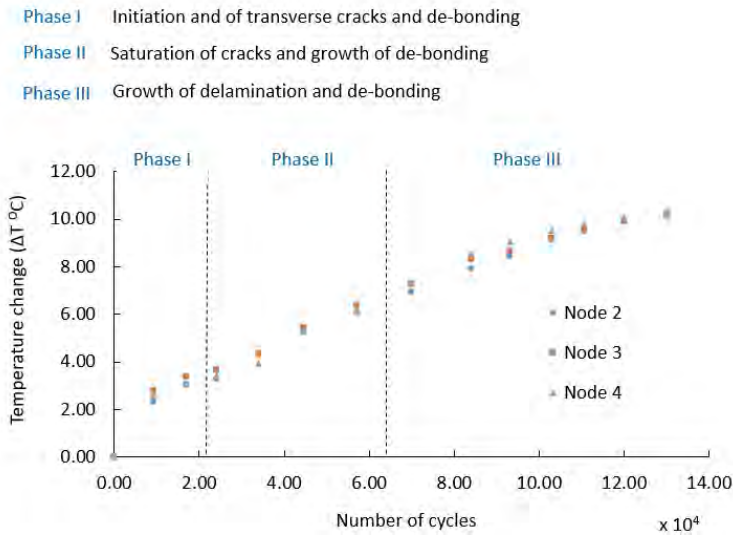


Figure 5.24: Average surface temperature of impact zone (element 2, element 3, and element 4) for the high level of energy impact and test specimen 1.

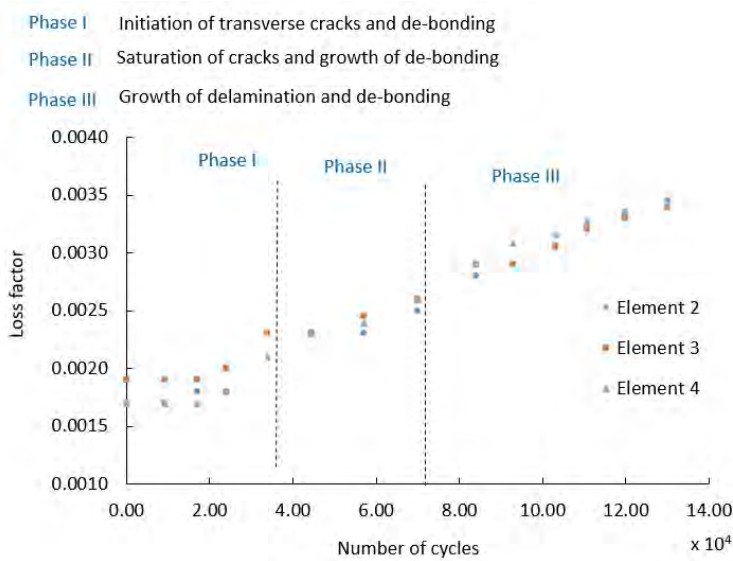


Figure 5.25: The loss factor of the impact zone (element 2, element 3, and element 4) during the fatigue tests for the high level of energy impact and test specimen 1.

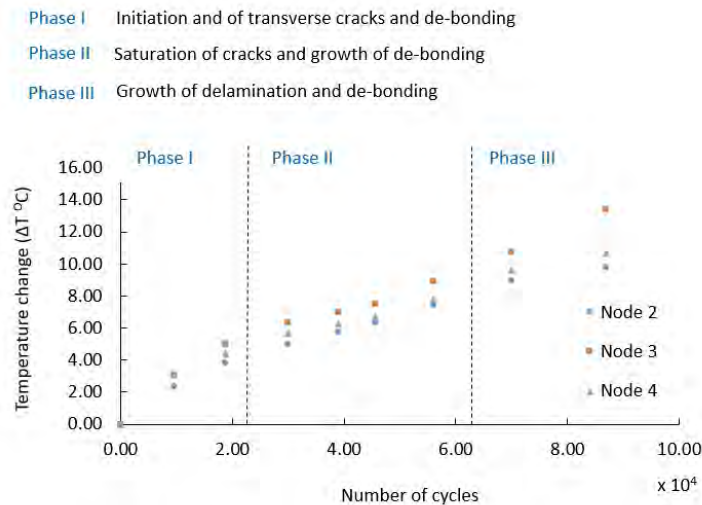


Figure 5.26: Average surface temperature of impact zone (element 2, element 3, and element 4) for the high level of energy impact and test specimen 2.

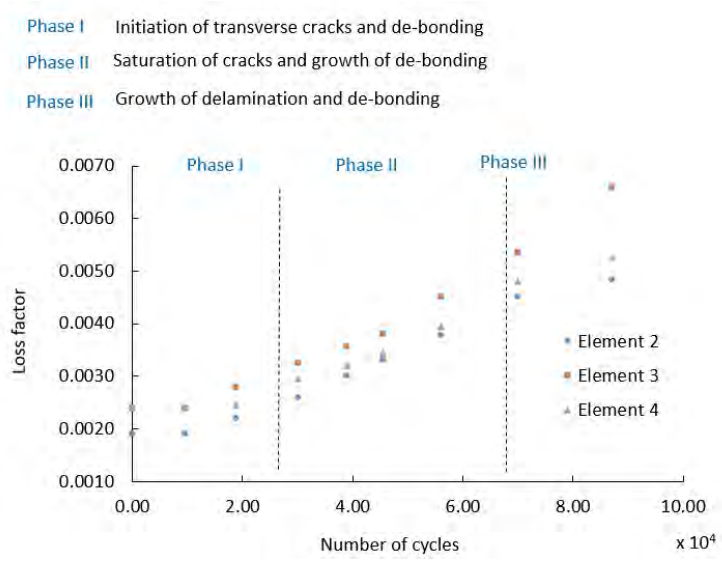


Figure 5.27: The loss factor of the impact zone (element 2, element 3, and element 4) during the fatigue tests for the high level of energy impact and test specimen 2.

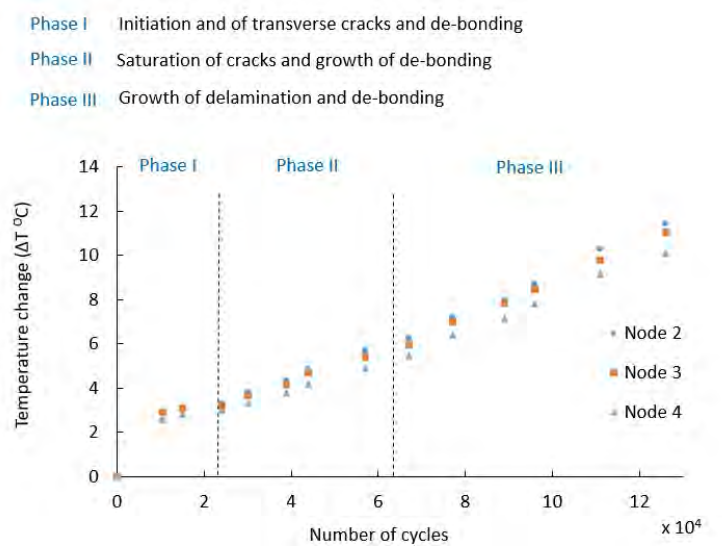


Figure 5.28: Average surface temperature of impact zone (element 2, element 3, and element 4) for the high level of energy impact and test specimen 3.

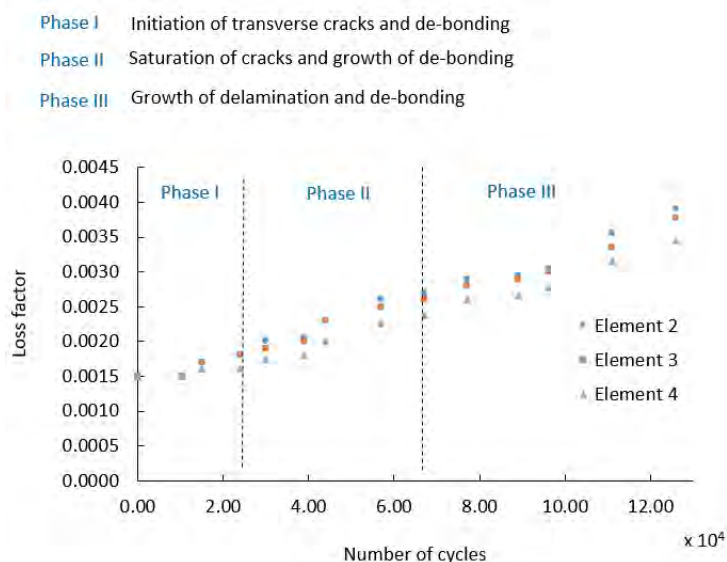


Figure 5.29: The loss factor of the impact zone (element 2, element 3, and element 4) during the fatigue tests for the high level of energy impact and test specimen 3.

5.6. CONCLUSION

In this study, a passive thermography technique has been used to characterize the effect of initial impact on fatigue damage propagation in test specimens representative of a spar cap-shear web thick adhesively-bonded connection of a wind turbine blade. The temperature measured by an infrared camera was used to estimate damping during different phases of damage. The fatigue damage following impact was characterized in specimens subjected to no impact, low, medium, and high levels of energy impact. Different levels of damage could be identified by examining the loss factor profile. When the loss factor started rising, it indicated that transverse cracks occurred in the adhesive joints. After the occurrence of early damage, the loss factor increased at the same rate indicating damage was progressing in the test specimens. The reducing rate of growth of the loss factor showed that damage progression was slowing down. This happened in the test specimens subjected to no impact and a low level of energy impact.

An increasing rate of growth of the loss factor during Phase III damage showed that delamination was growing in the laminate part of the adhesive joints. This occurred in the test specimens subjected to a medium and high level of energy impact. Delamination and consequently loss factor grew at a faster rate in the test specimens subjected to a high level of energy impact than in the test specimens subjected to a medium level of energy impact.

6

CONCLUSION

This thesis has investigated the propagation and characterization of non-impacted and impact fatigue damage in test specimens representative of a spar cap-shear web adhesively bonded connection in a wind turbine blade. Vibration, acoustic, and thermographic techniques were used to characterize damage. Firstly, different types of sensors and possible practical solutions for developing practical vibration, acoustic, and thermographic monitoring systems in wind turbine blades were described. Then experimental campaigns were carried out to establish the feasibility of using some of these sensors. A laser vibrometer, piezoelectric sensors, and an infrared camera were used for making the vibration, acoustic, and thermographic measurements, respectively. In this chapter, the main findings and the contribution of the thesis to the state-of-the-art in structural health monitoring of wind turbine blades are discussed. An outlook, suggestions, and recommendations for future research are also presented.

6.1. MAIN THESIS FINDINGS

Loads on wind turbine blades are dynamic and cause fatigue of the blades. Manufacturing flaws and impact are two major sources that instigate fatigue damage in wind turbine blades. Impact usually happens during the transportation or installation of the blades, especially in offshore wind turbines. The spar cap-shear web adhesively bonded connection of the wind turbine blade which carries the majority of the load, is one of the most vulnerable parts of the blade structure. It is crucial to understand fatigue damage propagation in this joint and find an effective health monitoring technique to characterize it.

Vibration, acoustic, and thermographic techniques were used to characterize damage to test specimens representative of the spar cap-shear web adhesively bonded connection. A laser vibrometer, piezoelectric sensors, and an infrared camera were used to make the vibration, acoustic, and thermographic measurements, respectively. Although, these well-developed sensors are well-suited for laboratory studies, they may not be applicable to an operational wind turbine blade. Finding practical solutions to develop feasible structural health monitoring systems for wind turbine blades requires further work.

The objective of this study was as follows;

- To investigate the effect of fatigue on the propagation of damage within the spar cap-shear web adhesively bonded connection of a wind turbine blade.
- To characterize fatigue damage in this joint using vibration, acoustic, and infrared thermographic techniques.

In the following subsections, the key findings are addressed.

6.1.1. DAMAGE PROPAGATION

Damage propagation in non-impact test specimens and test specimens subjected to an impact was studied.

NON-IMPACTED TEST SPECIMENS

Three phases of damage were observed during the fatigue test. In the initiation phase of damage (Phase I), transverse cracks occurred in the adhesive. During this phase, in the vicinity of these cracks, de-bonding of the adhesive from the laminate occurred. These cracks became widespread throughout the test specimen until the test specimen was saturated with cracks (saturation phase, Phase II). During this phase, crack length and the size of the de-bonded areas increased. In the final phase, de-bonding grew further causing the cracks to become linked together leading to final failure of the test specimen (Phase III).

IMPACTED TEST SPECIMENS

The effects of low, medium and high levels of energy impact on the fatigue damage propagation in the test specimens were investigated. In the test specimens

subjected to impact, as for the non-impact test specimen, three levels of damage were observed, but depending on the level of initial impact damage, damage propagation differed. In the test specimens subjected to a low level of energy impact, the damage propagation was the same as the damage propagation in the non-impacted test specimen.

In the test specimens subjected to a medium level of energy impact, early transverse cracks occurred in the impact zone. As the fatigue tests continued, cracks appeared in the other parts of the test specimens, but their density was higher in the impact zone. The de-laminated area induced by the impact grew continuously during the fatigue test. The growth of the de-bonded areas around the impact zone was greater in comparison to the other parts of the test specimen. Finally, the growth of the de-bonded areas in the impact zone led to failure of the test specimens.

In the test specimens subjected to the high level of energy impact, as for the test specimens subjected to the medium level of energy impact, early transverse cracks occurred at the impact zone, and the crack density there was higher than the other parts of the test specimen. The main difference here was that induced delamination by the impact grew at a faster pace than the test specimen subjected to the medium level of energy impact.

6.1.2. DAMAGE CHARACTERIZATION

DAMAGE CHARACTERIZATION USING VIBRATION AND THERMOGRAPHIC ANALYSIS FOR THE NON-IMPACTED TEST SPECIMENS

During the vibration and thermographic analysis, the displacement and temperature, respectively of the test specimens were measured, and the measurements were used to estimate damping and characterize damage.

In the initiation phase of fatigue damage, the overall loss factor increased by 10%-15% in the test specimen. During Phase II and Phase III of damage, the overall loss factor increased 80%-100% and 140%-150%, respectively.

The damping estimated by thermographic analysis was used to characterize damage. Three phases of damage can be distinguished by looking at the time history of the overall loss factor for the test specimens. At the start of the fatigue tests, the overall loss factor is constant, and as the first sign of cracks is seen in the test specimens, the loss factor starts rising (Phase I, initiation phase of damage). The overall loss factor increases at about a constant rate as cracks grow in length and number. This continues until test specimens are saturated with cracks (Phase II damage). After this stage, the rate of rising of the overall loss factor decreases, and it tends to flatten off. Both vibration and thermographic analysis can be used to estimate damping, but damping estimated by thermography is more consistent with damage propagation seen from high-resolution photos.

DAMAGE PROPAGATION DETERMINED USING THERMOGRAPHIC ANALYSIS FOR THE IMPACTED TEST SPECIMENS

The effect of impact on the fatigue damage was studied by subjecting the test specimens to low, medium, and high levels of energy impact. During the fatigue tests, the loss factor in the impact zone was calculated using thermographic analysis. The time history of the loss factor for the impact zone was used to characterize damage.

For the test specimens subjected to a low level of energy impact, this localized loss factor shows the same trend as the overall loss factor for the non-impacted test specimens indicating that a low level energy impact did not affect the fatigue damage propagation process.

For the test specimens subjected to a medium and high level of energy, the localized loss factor showed a different trend compared to those subjected to a low level of energy impact. This difference can be seen in Phase III of damage as delamination grows. In the test specimens subjected to a medium level of energy impact, the loss factor during Phase III of damage increased at a higher rate in comparison with the test specimens subjected to a low level of energy impact. This is due to the delamination growth in the test specimens subjected to a medium level of energy impact.

In the test specimens subjected to a high energy level impact, the loss factor during Phase III of damage increased at a higher rate in comparison with the test specimen subjected to a medium level of energy impact. This is due to the faster rate of delamination growth in the test specimens subjected to the high level of energy impact. In the test specimen subjected to a high level of energy, the loss factor during Phase III of damage increased at the same or at an even higher rate than Phase II of damage. But in the test specimens subjected to a medium energy impact, the loss factor during the Phase III of damage increased at a lower rate than during Phase II of damage.

DAMAGE LOCALIZATION THROUGH VIBRATION ANALYSIS

A simulation study was performed to investigate the possibility of localizing damage using vibration analysis. In this study, local damage was simulated in a test specimen modeled using a well-known structural code. Mass, stiffness, and the damping matrix extracted using this software were used in a Matlab code to find the phase of the components of the mode shapes.

The results showed that local damage affects the phase of the components of the mode shapes. The location of the damage is where the spatial derivative of the phase of the components of the mode shapes is minimum. This suggests that vibration analysis can, in principle, be used to localize damage. However, the change in the phase of the components of the mode shapes is relatively small, and it depends on the location of the damage. Overall for the high damage intensity level (level 9), this change is less than 1.5 °C. This small variation could not easily be used to identify damage using current modal analysis tools.

DAMAGE LOCALIZATION USING ACOUSTIC ANALYSIS FOR THE IMPACTED TEST SPECIMENS

For the test specimens subjected to the medium and high level of energy impact, the normalized number of AE events in the impact zone was higher in comparison with other areas of the specimens. In the test specimens subjected to a low level energy impact, the normalized cumulative number of AE events outside the impacted areas is higher than in the impact zone as the other parts of the test specimens experienced more severe damage during the fatigue test. This suggested that the acoustic emission technique could identify the impact zone in test specimens subjected to medium and high levels of energy impact.

DAMAGE PROPAGATION DETERMINED USING ACOUSTIC ANALYSIS FOR THE IMPACTED TEST SPECIMENS

The normalized cumulative number and spatial distribution of AE events were used to characterize impact damage. AE events were clustered into five types representing matrix-adhesive cracking, fiber-matrix de-bonding, delamination, laminate-adhesive de-bonding, and fiber breakage. A rapid increase in the rate of the number of normalized cumulative clustered AE events and an increase in the density of the spatial distribution of AE events were used to characterize damage.

Damage propagation was determined by looking simultaneously at the number of normalized cumulative clustered AE events for each section of the test specimens and a map of the spatial distribution of AE events. These two parameters showed the areas affected by damage in the test specimens during the fatigue load cycle history. The severity of damage could be seen by comparing the spatial density of AE events in the damaged area compared with other areas. Using these two parameters, the acoustic emission technique was seen to effectively identify the damaged areas and their propagation during the fatigue tests.

6.2. OUTLOOK AND FUTURE RESEARCH

6.2.1. ESTIMATION OF DAMPING IN AN OPERATIONAL WIND TURBINE BLADE

Damping could be an effective property to characterize damage in a wind turbine blade. Damping can be measured either by vibration or thermographic techniques. Estimating damping by vibration analysis in an operating wind turbine is challenging. Excitation of a large wind turbine blade to measure its response is difficult, however, operational modal analysis could be used. Operational modal analysis would require the measurement of particular data (blade displacement or acceleration) to determine modal parameters such as damping. Operational modal analysis is subject to more uncertainty than experimental modal analysis [183–187]. In operational modal analysis, the input force is considered to be Gaussian white noise. However, in the case of a wind turbine, due to the rotation of the blades and associated rotational sampling, harmonic components (multiple of blade rotational speed) appear in the forces exciting the blades. This makes operation modal analysis more complex [188].

Estimation of damping by passive infrared thermography could be a better option. Although an infrared camera or temperature sensors could be installed inside a blade to make appropriate temperature measurements, mathematical thermal modeling of the complex blade structure is challenging and needs more research.

6.2.2. QUANTIFICATION OF DAMAGE USING ACOUSTIC EMISSION DATA

An increase in the rate and the spatial density of AE events could be used to characterize damage. Although these parameters could be used to locate incipient damage and its propagation, it is not easy to quantify damage and estimate the remaining useful life (RUL) of damaged components. More advanced data processing algorithms using Artificial intelligence (AI) could be helpful in providing better estimates of RUL.

6.2.3. RECOMMENDATION

This research demonstrates that damping is an effective physical property for assessing the severity and progression of damage in adhesively bonded connections of wind turbine blades. Passive thermography analysis is highly recommended as a health monitoring technique for calculating damping in this context.

Acoustic emission can be used to localize damage and monitor its progression in adhesively bonded connections of wind turbine blades by analyzing the local density of AE events. Therefore, it is recommended for this purpose. However, further research is needed to quantify the severity of damage using acoustic emission techniques.

Vibration analysis can also determine damping, but thermography analysis is preferable for calculating damping as it provides more reliable results

6.3. FINAL REMARKS

Although SHM has developed enormously during recent years, more research and development, especially in sensor technology and data processing are required to make them practically available for wind turbine monitoring. More development is required to increase the accuracy of easily installed sensors such as MEMS and fiber optics. More advanced data processing algorithms are needed, especially for analyzing acoustic emission data. In addition, focusing on one specific method to satisfy all the requirements of the SHM system does not seem realistic. Each technique has its strengths, so fusing together different techniques may produce better results.

BIBLIOGRAPHY

- [1] C. Boller, F.-K. Chang, and Y. Fujino, eds. *Encyclopedia of Structural Health Monitoring*. Wiley, Jan. 2009. doi: [10.1002/9780470061626](https://doi.org/10.1002/9780470061626). url: <https://doi.org/10.1002/9780470061626>.
- [2] S. Keil. *Technology and Practical Use of Strain Gages With Particular Consideration of Stress Analysis Using Strain Gages*. Wilhelm Ernst & Sohn, Aug. 2017. doi: [10.1002/9783433606667](https://doi.org/10.1002/9783433606667). url: <https://doi.org/10.1002/9783433606667>.
- [3] Z. Ren, A. S. Verma, Y. Li, J. J. Teuwen, and Z. Jiang. "Offshore wind turbine operations and maintenance: A state-of-the-art review". In: *Renewable and Sustainable Energy Reviews* 144 (July 2021), p. 110886. doi: [10.1016/j.rser.2021.110886](https://doi.org/10.1016/j.rser.2021.110886). url: <https://doi.org/10.1016/j.rser.2021.110886>.
- [4] D. Sorensen and J. Sorensen. *Wind Energy Systems: Optimising Design and Construction for Safe and Reliable Operation*. Woodhead Publishing, 2016.
- [5] P. B. Tyler Stehly and P. Duffy. *2019 Cost of Wind Energy Review*. Technical Report NREL/TP-5000-81209. 2019.
- [6] C. Dao, B. Kazemtabrizi, and C. Crabtree. "Wind turbine reliability data review and impacts on levelised cost of energy". In: *Wind Energy* 22.12 (Dec. 2019), pp. 1848–1871. doi: [10.1002/we.2404](https://doi.org/10.1002/we.2404). url: <https://doi.org/10.1002/we.2404>.
- [7] M. Wang, J. Lynch, and H. Sohn. *Sensor Technologies for Civil Infrastructures*. Woodhead Publishing Series in Electronic and Optical Materials. Woodhead Publishing, 2014. isbn: 978-1-78242-242-6.
- [8] D. Zarouchas, A. A. Maris, F. Sayer, D. Van Hemlrijck, and A. M. Van Wingerde. "Investigations on the mechanical behavior of a wind rotor blade subcomponent." In: *Composites Part B: Engineering* 43 (2012), pp. 647–654. url: <https://doi.org/10.1016/j.compositesb.2011.10.009>.
- [9] F. Sayer, A. Antoniou, and A. Van Wingerde. "Investigation of structural bond lines in wind turbine blades by sub-component tests." In: *International Journal of Adhesion and Adhesives* 37 (2012), pp. 129–135. url: <https://doi.org/10.1016/j.ijadhadh.2012.01.021>.
- [10] W. Yang, P. J. Tavner, C. J. Crabtree, Y. Feng, and Y. Qiu. "Wind turbine condition monitoring: technical and commercial challenges". In: *Wind Energy* 17.5 (Aug. 2012), pp. 673–693. doi: [10.1002/we.1508](https://doi.org/10.1002/we.1508). url: <https://doi.org/10.1002/we.1508>.

- [11] B. Hu, P. Stumpf, and W. van der Deijl. *Offshore wind access*. TNO report, Report no:R10633, Third edition. 2019.
- [12] A. Shanker Verma, P. N. Vedvik, and Z. Gao. “A comprehensive numerical investigation of the impact behaviour of an offshore wind turbine blade due to impact loads during installation.” In: *Ocean Engineering* 172 (2019), pp. 127–145. url: <https://doi.org/10.1016/j.oceaneng.2018.11.021>.
- [13] D. Tcherniak and L. L. Molgaard. “Active vibration-based structural health monitoring system for wind turbine blade: Demonstration on an operating Vestas V27 wind turbine”. In: *Structural Health Monitoring: An International Journal* 16.5 (Aug. 2017), pp. 536–550. doi: [10.1177/1475921717722725](https://doi.org/10.1177/1475921717722725). url: <https://doi.org/10.1177/1475921717722725>.
- [14] C. Aszkler. “CHAPTER 5 - Acceleration, Shock and Vibration Sensors”. In: *Sensor Technology Handbook*. Ed. by J. S. Wilson. Burlington: Newnes, 2005, pp. 137–159. isbn: 978-0-7506-7729-5. doi: <https://doi.org/10.1016/B978-075067729-5/50045-8>. url: <https://www.sciencedirect.com/science/article/pii/B9780750677295500458>.
- [15] J. J. Villacorta, L. del-Val, R. D. Martinez, J.-A. Balmori, A. Magdaleno, G. Lopez, A. Izquierdo, A. Lorenzana, and L.-A. Basterra. “Design and Validation of a Scalable, Reconfigurable and Low-Cost Structural Health Monitoring System”. In: *Sensors* 21.2 (Jan. 2021), p. 648. doi: [10.3390/s21020648](https://doi.org/10.3390/s21020648). url: <https://doi.org/10.3390/s21020648>.
- [16] C. Bedon, E. Bergamo, M. Izzi, and S. Noè. “Prototyping and Validation of MEMS Accelerometers for Structural Health Monitoring—The Case Study of the Pietratagliata Cable-Stayed Bridge”. In: *Journal of Sensor and Actuator Networks* 7.3 (July 2018), p. 30. doi: [10.3390/jsan7030030](https://doi.org/10.3390/jsan7030030). url: <https://doi.org/10.3390/jsan7030030>.
- [17] F. D. Nuzzo, D. Brunelli, T. Polonelli, and L. Benini. “Structural Health Monitoring System With Narrowband IoT and MEMS Sensors”. In: *IEEE Sensors Journal* 21.14 (July 2021), pp. 16371–16380. doi: [10.1109/jsen.2021.3075093](https://doi.org/10.1109/jsen.2021.3075093). url: <https://doi.org/10.1109/jsen.2021.3075093>.
- [18] A. Girolami, D. Brunelli, and L. Benini. “Low-cost and distributed health monitoring system for critical buildings”. In: *2017 IEEE Workshop on Environmental, Energy, and Structural Monitoring Systems (EESMS)*. IEEE, July 2017. doi: [10.1109/eesms.2017.8052686](https://doi.org/10.1109/eesms.2017.8052686). url: <https://doi.org/10.1109/eesms.2017.8052686>.
- [19] N. M. Ali, G. Ting, L. Shiung, L. Theng, L. Ching, M. Sulaiman, H. Shah, M. Ghazaly, and S. Razali. “Issues and Challenges of Sensor Technologies in Microelectromechanical System (MEMS) in Smartphones for Motion Tracking Applications”. In: *Journal of Telecommunication, Electronic and Computer Engineering* 10 (2018), pp. 135–140.

- [20] T. Loss and A. Bergmann. "Vibration-Based Fingerprint Algorithm for Structural Health Monitoring of Wind Turbine Blades". In: *Applied Sciences* 11.9 (May 2021), p. 4294. doi: [10.3390/app11094294](https://doi.org/10.3390/app11094294). url: <https://doi.org/10.3390/app11094294>.
- [21] J. O. Willberry, M. Papaalias, and G. F. Fernando. "Structural Health Monitoring Using Fibre Optic Acoustic Emission Sensors". In: *Sensors* 20.21 (Nov. 2020), p. 6369. doi: [10.3390/s20216369](https://doi.org/10.3390/s20216369). url: <https://doi.org/10.3390/s20216369>.
- [22] K. Loupos and A. Amditis. "Structural Health Monitoring Fiber Optic Sensors". In: *Smart Sensors, Measurement and Instrumentation*. Springer International Publishing, Nov. 2016, pp. 185–206. doi: [10.1007/978-3-319-42625-9_9](https://doi.org/10.1007/978-3-319-42625-9_9). url: https://doi.org/10.1007/978-3-319-42625-9_9.
- [23] K. T. V. Grattan and Y. N. Ning. "Classification of optical fiber sensors". In: *Optical Fiber Sensor Technology*. Springer US, 1998, pp. 1–35. doi: [10.1007/978-1-4615-5787-6_1](https://doi.org/10.1007/978-1-4615-5787-6_1). url: https://doi.org/10.1007/978-1-4615-5787-6_1.
- [24] L. Glavind, I. S. Olesen, B. F. Skipper, and M. Kristensen. "Fiber-optical grating sensors for wind turbine blades: a review". In: *Optical Engineering* 52.3 (Mar. 2013), p. 030901. doi: [10.1117/1.oe.52.3.030901](https://doi.org/10.1117/1.oe.52.3.030901). url: <https://doi.org/10.1117/1.oe.52.3.030901>.
- [25] P. Zhu, X. Feng, Z. Liu, M. Huang, H. Xie, and M. A. Soto. "Reliable packaging of optical fiber Bragg grating sensors for carbon fiber composite wind turbine blades". In: *Composites Science and Technology* 213 (Sept. 2021), p. 108933. doi: [10.1016/j.compscitech.2021.108933](https://doi.org/10.1016/j.compscitech.2021.108933). url: <https://doi.org/10.1016/j.compscitech.2021.108933>.
- [26] G. Cazzulani, S. Cinquemani, L. Benedetti, and M. Belloli. "Load estimation and vibration monitoring of scale model wind turbine blades through optical fiber sensors". In: *Engineering Research Express* 3.2 (June 2021), p. 025036. doi: [10.1088/2631-8695/ac060e](https://doi.org/10.1088/2631-8695/ac060e). url: <https://doi.org/10.1088/2631-8695/ac060e>.
- [27] D. Anastasopoulos, M. D. Smedt, L. Vandewalle, G. D. Roeck, and E. P. Reynders. "Damage identification using modal strains identified from operational fiber-optic Bragg grating data". In: *Structural Health Monitoring* 17.6 (Dec. 2017), pp. 1441–1459. doi: [10.1177/1475921717744480](https://doi.org/10.1177/1475921717744480). url: <https://doi.org/10.1177/1475921717744480>.
- [28] A. Cusano, P. Capoluongo, S. Campopiano, A. Cutolo, M. Giordano, F. Felli, A. Paolozzi, and M. Caponero. "Experimental modal analysis of an aircraft model wing by embedded fiber Bragg grating sensors". In: *IEEE Sensors Journal* 6.1 (Feb. 2006), pp. 67–77. doi: [10.1109/jsen.2005.854152](https://doi.org/10.1109/jsen.2005.854152). url: <https://doi.org/10.1109/jsen.2005.854152>.

- [29] *Wind Turbine Blade Condition Monitoring With Bladesave*. <https://www.twi-global.com/media-and-events/press-releases/2020/wind-turbine-blade-condition-monitoring-with-bladesave>. Accessed: 2022-20-4.
- [30] Y.-K. An, M. Kim, and H. Sohn. "4 - Piezoelectric transducers for assessing and monitoring civil infrastructures". In: *Sensor Technologies for Civil Infrastructures*. Ed. by M. Wang, J. Lynch, and H. Sohn. Vol. 55. Woodhead Publishing Series in Electronic and Optical Materials. Woodhead Publishing, 2014, pp. 86–120. isbn: 978-0-85709-432-2. doi: <https://doi.org/10.1533/9780857099136.86>. url: <https://www.sciencedirect.com/science/article/pii/B9780857094322500048>.
- [31] D. Ozevin. "MEMS Acoustic Emission Sensors". In: *Applied Sciences* 10.24 (Dec. 2020), p. 8966. doi: [10.3390/app10248966](https://doi.org/10.3390/app10248966). url: <https://doi.org/10.3390/app10248966>.
- [32] H. Saboonchi, D. Ozevin, and M. Kabir. "MEMS sensor fusion: Acoustic emission and strain". In: *Sensors and Actuators A: Physical* 247 (Aug. 2016), pp. 566–578. doi: [10.1016/j.sna.2016.05.014](https://doi.org/10.1016/j.sna.2016.05.014). url: <https://doi.org/10.1016/j.sna.2016.05.014>.
- [33] M. Kabir, H. Kazari, and D. Ozevin. "Piezoelectric MEMS acoustic emission sensors". In: *Sensors and Actuators A: Physical* 279 (Aug. 2018), pp. 53–64. doi: [10.1016/j.sna.2018.05.044](https://doi.org/10.1016/j.sna.2018.05.044). url: <https://doi.org/10.1016/j.sna.2018.05.044>.
- [34] T. Fu, Y. Liu, Q. Li, and J. Leng. "Fiber optic acoustic emission sensor and its applications in the structural health monitoring of CFRP materials". In: *Optics and Lasers in Engineering* 47.10 (Oct. 2009), pp. 1056–1062. doi: [10.1016/j.optlaseng.2009.03.011](https://doi.org/10.1016/j.optlaseng.2009.03.011). url: <https://doi.org/10.1016/j.optlaseng.2009.03.011>.
- [35] T. Fu, Y. Liu, K.-t. Lau, and J. Leng. "Impact source identification in a carbon fiber reinforced polymer plate by using embedded fiber optic acoustic emission sensors". In: *Composites Part B: Engineering* 66 (Nov. 2014), pp. 420–429. doi: [10.1016/j.compositesb.2014.06.004](https://doi.org/10.1016/j.compositesb.2014.06.004). url: <https://doi.org/10.1016/j.compositesb.2014.06.004>.
- [36] Y.-J. Rao. "In-fibre Bragg grating sensors". In: *Measurement Science and Technology* 8.4 (Apr. 1997), pp. 355–375. doi: [10.1088/0957-0233/8/4/002](https://doi.org/10.1088/0957-0233/8/4/002). url: <https://doi.org/10.1088/0957-0233/8/4/002>.
- [37] S. Jinachandran and G. Rajan. "Fibre Bragg Grating Based Acoustic Emission Measurement System for Structural Health Monitoring Applications". In: *Materials* 14.4 (Feb. 2021), p. 897. doi: [10.3390/ma14040897](https://doi.org/10.3390/ma14040897). url: <https://doi.org/10.3390/ma14040897>.
- [38] C. Zhang and L. J. Bond. "Performance evaluation of the Fiber Bragg Grating (FBG) sensing device and comparison with piezoelectric sensors for AE detection". In: *AIP Conference Proceedings*. Author(s), 2017. doi: [10.1063/1.4974622](https://doi.org/10.1063/1.4974622). url: <https://doi.org/10.1063/1.4974622>.

- [39] I. M. Perez, H. Cui, and E. Udd. "Acoustic emission detection using fiber Bragg gratings". In: *SPIE Proceedings*. SPIE, Aug. 2001. doi: [10.1117/12.435542](https://doi.org/10.1117/12.435542). url: <https://doi.org/10.1117/12.435542>.
- [40] M. Takuma, S. Hisada, K. Saitoh, Y. Takahashi, Y. Kobayashi, A. Kadono, A. Murata, S. Iwata, and T. Sasaki. "Acoustic Emission Measurement by Fiber Bragg Grating Glued to Cylindrical Sensor Holder". In: *Advances in Materials Science and Engineering 2014* (2014), pp. 1–12. doi: [10.1155/2014/274071](https://doi.org/10.1155/2014/274071). url: <https://doi.org/10.1155/2014/274071>.
- [41] C. Lan, W. Zhou, and Y. Xie. "Detection of Ultrasonic Stress Waves in Structures Using 3D Shaped Optic Fiber Based on a Mach-Zehnder Interferometer". In: *Sensors* 18.4 (Apr. 2018), p. 1218. doi: [10.3390/s18041218](https://doi.org/10.3390/s18041218). url: <https://doi.org/10.3390/s18041218>.
- [42] Y. Wang, H. Yuan, X. Liu, Q. Bai, H. Zhang, Y. Gao, and B. Jin. "A Comprehensive Study of Optical Fiber Acoustic Sensing". In: *IEEE Access* 7 (2019), pp. 85821–85837. doi: [10.1109/access.2019.2924736](https://doi.org/10.1109/access.2019.2924736). url: <https://doi.org/10.1109/access.2019.2924736>.
- [43] Y. Kong, W. Ding, Z. W. Li, Y. J. Zhang, F. Ansari, and S. Yi. "Double Mach-Zehnder acoustic emission interferometer for detection of damage in structures". In: *Optics Communications* 459 (Mar. 2020), p. 125076. doi: [10.1016/j.optcom.2019.125076](https://doi.org/10.1016/j.optcom.2019.125076). url: <https://doi.org/10.1016/j.optcom.2019.125076>.
- [44] K.-S. Kim, Y. Mizuno, and K. Nakamura. "Fiber-optic ultrasonic hydrophone using short Fabry-Perot cavity with multilayer reflectors deposited on small stub". In: *Ultrasonics* 54.4 (Apr. 2014), pp. 1047–1051. doi: [10.1016/j.ultras.2013.12.009](https://doi.org/10.1016/j.ultras.2013.12.009). url: <https://doi.org/10.1016/j.ultras.2013.12.009>.
- [45] Y. Xu. "Delamination detection at web/flange junction of I-section composite beam with fiber optical interferometer sensor". In: *Composites Part B: Engineering* 58 (Mar. 2014), pp. 140–146. doi: [10.1016/j.compositesb.2013.10.070](https://doi.org/10.1016/j.compositesb.2013.10.070). url: <https://doi.org/10.1016/j.compositesb.2013.10.070>.
- [46] S. Liang, C. Zhang, W. Lin, L. Li, C. Li, X. Feng, and B. Lin. "Fiber-optic intrinsic distributed acoustic emission sensor for large structure health monitoring". In: *Optics Letters* 34.12 (June 2009), p. 1858. doi: [10.1364/ol.34.001858](https://doi.org/10.1364/ol.34.001858). url: <https://doi.org/10.1364/ol.34.001858>.
- [47] L. Schenato. "A Review of Distributed Fibre Optic Sensors for Geo-Hydrological Applications". In: *Applied Sciences* 7.9 (Sept. 2017), p. 896. doi: [10.3390/app7090896](https://doi.org/10.3390/app7090896). url: <https://doi.org/10.3390/app7090896>.
- [48] X. Bao and Y. Wang. "Recent Advancements in Rayleigh Scattering-Based Distributed Fiber Sensors". In: *Advanced Devices and Instrumentation 2021* (Mar. 2021), pp. 1–17. doi: [10.34133/2021/8696571](https://doi.org/10.34133/2021/8696571). url: <https://doi.org/10.34133/2021/8696571>.

- [49] C. M. Monsberger and W. Lienhart. "Distributed Fiber Optic Shape Sensing of Concrete Structures". In: *Sensors* 21.18 (Sept. 2021), p. 6098. doi: [10.3390/s21186098](https://doi.org/10.3390/s21186098). url: <https://doi.org/10.3390/s21186098>.
- [50] *FLIR A 310 f model, Fixed type FLIR Infrared Camera*. <https://www.flir.com/products>. 2022.
- [51] *Shear web assembly of wind turbine blade*. <http://www.ais4ndt.com/wind-turbine-blades>. 2022.
- [52] S. Drusová, W. Bakx, P. J. Doornenbal, R. M. Wagterveld, V. F. Bense, and H. L. Offerhaus. "Comparison of three types of fiber optic sensors for temperature monitoring in a groundwater flow simulator". In: *Sensors and Actuators A: Physical* 331 (2021), p. 112682. doi: <https://doi.org/10.1016/j.sna.2021.112682>. url: <https://www.sciencedirect.com/science/article/pii/S0924424721001448>.
- [53] M. Mikolajek, R. Martinek, J. Koziorek, S. Hejduk, J. Vitasek, A. Vanderka, R. Poboril, V. Vasinek, and R. Hercik. "Temperature Measurement Using Optical Fiber Methods: Overview and Evaluation". In: *Journal of Sensors* 2020 (Oct. 2020). Ed. by Q. Wu, pp. 1–25. doi: [10.1155/2020/8831332](https://doi.org/10.1155/2020/8831332). url: <https://doi.org/10.1155/2020/8831332>.
- [54] M. Ramakrishnan, G. Rajan, Y. Semenova, and G. Farrell. "Overview of Fiber Optic Sensor Technologies for Strain/Temperature Sensing Applications in Composite Materials". In: *Sensors* 16.1 (Jan. 2016), p. 99. doi: [10.3390/s16010099](https://doi.org/10.3390/s16010099). url: <https://doi.org/10.3390/s16010099>.
- [55] M. Szczerska. "Temperature Sensors Based on Polymer Fiber Optic Interferometer". In: *Chemosensors* 10.6 (June 2022), p. 228. doi: [10.3390/chemosensors10060228](https://doi.org/10.3390/chemosensors10060228).
- [56] P. Avitabile. *Modal Testing: A Practitioner's Guide*. Wiley and Sons Ltd, 2017. isbn: ISBN: 978-1-119-22289-7.
- [57] H. Sohn, C. R. Farrar, F. M. Hemez, D. D. Shunk, D. W. Stinemates, B. R. Nadler, and J. J. Czarnecki. "A review of structural health monitoring literature: 1996–2001". In: *Los Alamos National Laboratory, USA* 1 (2003).
- [58] W. S. Doebbling, R. C. Farar, B. M. Prime, and W. D. Shevitz. "Damage Identification and Health Monitoring of Structural and Mechanical Systems from Changes in Their Vibration Characteristics: A Literature Review". In: *Los Alamos National Laboratory report No:LA-13070-MS*. (1996).
- [59] J. K. Vandiver. "Detection of Structural Failure on Fixed Platforms By Measurement of Dynamic Response". In: *Offshore Technology Conference*. Offshore Technology Conference, 1975. doi: [10.4043/2267-ms](https://doi.org/10.4043/2267-ms). url: <https://doi.org/10.4043/2267-ms>.
- [60] J. K. Vandiver. "Detection of Structural Failure on Fixed Platforms By Measurement of Dynamic Response". In: *Journal of Petroleum Technology* 29.03 (Mar. 1977), pp. 305–310. doi: [10.2118/5679-pa](https://doi.org/10.2118/5679-pa). url: <https://doi.org/10.2118/5679-pa>.

- [61] R. D. Begg, A. C. Mackenzie, C. J. Dodds, and O. D. Loland. "Structural Integrity Monitoring Using Digital Processing Of Vibration Signals". In: *Offshore Technology Conference*. Offshore Technology Conference, 1976. doi: [10.4043/2549-ms](https://doi.org/10.4043/2549-ms). url: <https://doi.org/10.4043/2549-ms>.
- [62] O. Loland and C. J. Dodds. "Experiences in Developing Monitoring Systems and Operating Integrity In the North Sea". In: *Offshore Technology Conference*. Offshore Technology Conference, 1976. doi: [10.4043/2551-ms](https://doi.org/10.4043/2551-ms). url: <https://doi.org/10.4043/2551-ms>.
- [63] M. E. Wojnarowski, S. G. Stiansen, and N. E. Reddy. "Structural Integrity Evaluation Of A Fixed Platform Using Vibration Criteria". In: *All Days*. OTC, May 1977. doi: [10.4043/2909-ms](https://doi.org/10.4043/2909-ms). url: <https://doi.org/10.4043/2909-ms>.
- [64] R. Coppolino and S. Rubin. "Detectability Of Structural Failures In Offshore Platforms By Ambient Vibration Monitoring". In: *Offshore Technology Conference*. Offshore Technology Conference, 1980. doi: [10.4043/3865-ms](https://doi.org/10.4043/3865-ms). url: <https://doi.org/10.4043/3865-ms>.
- [65] D. M. Duggan, E. R. Wallace, and S. R. Caldwell. "Measured and Predicted Vibrational Behavior of Gulf of Mexico Platforms". In: *Offshore Technology Conference*. Offshore Technology Conference, 1980. doi: [10.4043/3864-ms](https://doi.org/10.4043/3864-ms). url: <https://doi.org/10.4043/3864-ms>.
- [66] R. M. Kenley and C. J. Dodds. "West Sole WE Platform: Detection Of Damage By Structural Response Measurements". In: *Offshore Technology Conference*. Offshore Technology Conference, 1980. doi: [10.4043/3866-ms](https://doi.org/10.4043/3866-ms). url: <https://doi.org/10.4043/3866-ms>.
- [67] H. Crohas and P. Lepert. "Damage-detection monitoring method for offshore platforms is field-tested". In: *Oil Gas* 8.80 (1982). url: <https://www.osti.gov/biblio/6592179>.
- [68] R. Nataraja. "Structural Integrity Monitoring in Real Seas". In: *All Days*. OTC, May 1983. doi: [10.4043/4538-ms](https://doi.org/10.4043/4538-ms). url: <https://doi.org/10.4043/4538-ms>.
- [69] T. R. Whittome and C. J. Dodds. "9 Monitoring offshore structures by vibration techniques". In: *DESIGN IN OFFSHORE STRUCTURES*. Thomas Telford Publishing, Jan. 1983, pp. 93–100. doi: [10.1680/dios.01954.0013](https://doi.org/10.1680/dios.01954.0013). url: <https://doi.org/10.1680/dios.01954.0013>.
- [70] P. Gudmundson. "The dynamic behaviour of slender structures with cross-sectional cracks". In: *Journal of the Mechanics and Physics of Solids* 31.4 (Jan. 1983), pp. 329–345. doi: [10.1016/0022-5096\(83\)90003-0](https://doi.org/10.1016/0022-5096(83)90003-0). url: [https://doi.org/10.1016/0022-5096\(83\)90003-0](https://doi.org/10.1016/0022-5096(83)90003-0).
- [71] F. Ismail, A. Ibrahim, and H. Martin. "Identification of fatigue cracks from vibration testing". In: *Journal of Sound and Vibration* 140.2 (July 1990), pp. 305–317. doi: [10.1016/0022-460x\(90\)90530-d](https://doi.org/10.1016/0022-460x(90)90530-d). url: [https://doi.org/10.1016/0022-460x\(90\)90530-d](https://doi.org/10.1016/0022-460x(90)90530-d).

- [72] M. Chowdhury and M. Ramirez. "A Comparison of the Modal Responses for Defective Versus Nondefective Concrete Test Beams". In: *10th International Modal Analysis Conference*. Vol. 1. Jan. 1992, pp. 508–515.
- [73] C. Fox. "The location of defects in structures - A comparison of the use of natural frequency and mode shape data". In: *10th International Modal Analysis Conference*. Vol. 1. Jan. 1992, pp. 522–528.
- [74] M. Srinivasan and C. A. Kot. "Effects of Damage on the Modal Parameters of a Cylindrical Shell". In: *10th International Modal Analysis Conference*. Vol. 1. Jan. 1992, pp. 529–535.
- [75] A. Pandey, M. Biswas, and M. Samman. "Damage detection from changes in curvature mode shapes". In: *Journal of Sound and Vibration* 145.2 (Mar. 1991), pp. 321–332. doi: [10.1016/0022-460x\(91\)90595-b](https://doi.org/10.1016/0022-460x(91)90595-b). url: [https://doi.org/10.1016/0022-460x\(91\)90595-b](https://doi.org/10.1016/0022-460x(91)90595-b).
- [76] J. Chance, G. R. Tomlinson, and K. Worden. "A simplified approach to the numerical and experimental modeling of the dynamics of a cracked beam". In: *Proceedings of 12th International Modal Analysis Conference*. 1994, pp. 778–785.
- [77] N. Stubbs, J. T. Kim, and C. R. Farrar. "Field Verification of a Nondestructive Damage Localization and Severity Estimation Algorithm". In: *Proceedings of the 13th International Modal Analysis Conference*. Vol. 2460. Society of Photo-Optical Instrumentation Engineers (SPIE) Conference Series. Jan. 1995, p. 210.
- [78] D. I. Nwosu, A. S. J. Swamidas, and J. Y. Guigne. "Dynamic Response of Tubular T-Joints Under the Influence of Propagating Cracks". In: *Journal of Offshore Mechanics and Arctic Engineering* 118.1 (Feb. 1996), pp. 71–78. doi: [10.1115/1.2828804](https://doi.org/10.1115/1.2828804). url: <https://doi.org/10.1115/1.2828804>.
- [79] M. W. West. "Illustration of the use of modal assurance criterion to detect structural changes in an Orbiter test specimen". In: *In Proc. Air Force Conference on Aircraft Structural Integrity*. 1986.
- [80] M. Yuen. "A numerical study of the eigenparameters of a damaged cantilever". In: *Journal of Sound and Vibration* 103.3 (Dec. 1985), pp. 301–310. doi: [10.1016/0022-460x\(85\)90423-7](https://doi.org/10.1016/0022-460x(85)90423-7). url: [https://doi.org/10.1016/0022-460x\(85\)90423-7](https://doi.org/10.1016/0022-460x(85)90423-7).
- [81] P. Rizos, N. Aspragathos, and A. Dimarogonas. "Identification of crack location and magnitude in a cantilever beam from the vibration modes". In: *Journal of Sound and Vibration* 138.3 (May 1990), pp. 381–388. doi: [10.1016/0022-460x\(90\)90593-o](https://doi.org/10.1016/0022-460x(90)90593-o). url: [https://doi.org/10.1016/0022-460x\(90\)90593-o](https://doi.org/10.1016/0022-460x(90)90593-o).

- [82] R. A. Osegueda and P. D. DSouza. "Damage Evaluation Of An Offshore Structure Model Using Vibration Measurements". In: vol. All Days. International Ocean and Polar Engineering Conference. ISOPE-I-92-390. June 1992. eprint: <https://onepetro.org/ISOPEIOPEC/proceedings-pdf/ISOPE92/All-ISOPE92/ISOPE-I-92-390/1986107/isope-i-92-390.pdf>.
- [83] T. Kam and T. Lee. "Detection of cracks in structures using modal test data". In: *Engineering Fracture Mechanics* 42.2 (May 1992), pp. 381–387. doi: [10.1016/0013-7944\(92\)90227-6](https://doi.org/10.1016/0013-7944(92)90227-6). url: [https://doi.org/10.1016/0013-7944\(92\)90227-6](https://doi.org/10.1016/0013-7944(92)90227-6).
- [84] R. L. Mayes. "An Experimental Algorithm for Detecting Damage Applied to the I-40 Bridge Over the Rio Grande". In: *SPIE Proceedings*. Ed. by L. K. Matthews. SPIE, Apr. 1995. doi: [10.1117/12.207729](https://doi.org/10.1117/12.207729). url: <https://doi.org/10.1117/12.207729>.
- [85] J. M. Ko, C. W. Wong, and H. F. Lam. "Damage Detection in Steel Framed Structures by Vibration Measurement Approach". In: *Proceedings of the 12th International Modal Analysis*. Vol. 2251. Society of Photo-Optical Instrumentation Engineers (SPIE) Conference Series. Jan. 1994, p. 280.
- [86] H. F. Lam, J. M. Ko, and C. W. Wong. *Detection of Damage Location Based on Sensitivity Analysis*. Bellingham, WA, 1995.
- [87] O. Al-Khudairi, H. Hadavinia, C. Little, G. Gillmore, P. Greaves, and K. Dyer. "Full-Scale Fatigue Testing of a Wind Turbine Blade in Flapwise Direction and Examining the Effect of Crack Propagation on the Blade Performance". In: *Materials* 10.10 (Oct. 2017), p. 1152. doi: [10.3390/ma10101152](https://doi.org/10.3390/ma10101152). url: <https://doi.org/10.3390/ma10101152>.
- [88] C. Modena, D. Sonda, and D. Zonta. "Damage Localization in Reinforced Concrete Structures by Using Damping Measurements". In: *Key Engineering Materials* 167-168 (June 1999), pp. 132–141. doi: [10.4028/www.scientific.net/kem.167-168.132](https://doi.org/10.4028/www.scientific.net/kem.167-168.132). url: <https://doi.org/10.4028/www.scientific.net/kem.167-168.132>.
- [89] D. ZONTA and C. MODENA. "OBSERVATIONS ON THE APPEARANCE OF DISPERSIVE PHENOMENA IN DAMAGED STRUCTURES". In: *Journal of Sound and Vibration* 241.5 (Apr. 2001), pp. 925–933. doi: [10.1006/jsvi.2000.3320](https://doi.org/10.1006/jsvi.2000.3320). url: <https://doi.org/10.1006/jsvi.2000.3320>.
- [90] G. Kawiecki. "Modal damping measurement for damage detection". In: *Smart Materials and Structures* 10.3 (June 2001), pp. 466–471. doi: [10.1088/0964-1726/10/3/307](https://doi.org/10.1088/0964-1726/10/3/307). url: <https://doi.org/10.1088/0964-1726/10/3/307>.
- [91] S. Keye, M. Rose, and D. Sachau. "Localizing delamination damages in aircraft panels from modal damping parameters". In: *in Proc. 19th international modal analysis conf(IMAC XIX)*. 2001, pp. 412–417.

- [92] C. Kyriazoglou, B. L. Page, and F. Guild. "Vibration damping for crack detection in composite laminates". In: *Composites Part A: Applied Science and Manufacturing* 35.7-8 (July 2004), pp. 945–953. doi: [10.1016/j.compositesa.2004.01.003](https://doi.org/10.1016/j.compositesa.2004.01.003).
- [93] Z. Zhang. "Relation of damping and fatigue damage of unidirectional fibre composites". In: *International Journal of Fatigue* 24.7 (July 2002), pp. 713–718. doi: [10.1016/s0142-1123\(01\)00206-7](https://doi.org/10.1016/s0142-1123(01)00206-7). url: [https://doi.org/10.1016/s0142-1123\(01\)00206-7](https://doi.org/10.1016/s0142-1123(01)00206-7).
- [94] Z. Kiral, B. M. İçten, and B. G. Kiral. "Effect of impact failure on the damping characteristics of beam-like composite structures". In: *Composites Part B: Engineering* 43.8 (Dec. 2012), pp. 3053–3060. doi: [10.1016/j.compositesb.2012.05.005](https://doi.org/10.1016/j.compositesb.2012.05.005). url: <https://doi.org/10.1016/j.compositesb.2012.05.005>.
- [95] V. Birman and L. W. Byrd. "Effect of Matrix Cracks on Damping in Unidirectional and Cross-Ply Ceramic Matrix Composites". In: *Journal of Composite Materials* 36.15 (Aug. 2002), pp. 1859–1877.
- [96] M. Cao, G. Sha, Y. Gao, and W. Ostachowicz. "Structural damage identification using damping: a compendium of uses and features". In: *Smart Materials and Structures*. 26 (2017), p. 043001.
- [97] P. K. Kopparthi, K. K. Y. Aerra, B. R. Pathakokila, and S. Gamini. "Bending and viscoelastic behaviour of delaminated woven E-glass/epoxy composite". In: *Australian Journal of Mechanical Engineering* (Aug. 2020), pp. 1–10. doi: [10.1080/14484846.2020.1794506](https://doi.org/10.1080/14484846.2020.1794506). url: <https://doi.org/10.1080/14484846.2020.1794506>.
- [98] Y. Shen, J. Tan, L. Fernandes, Z. Qu, and Y. Li. "Dynamic Mechanical Analysis on Delaminated Flax Fiber Reinforced Composites". In: *Materials* 12.16 (Aug. 2019), p. 2559. doi: [10.3390/ma12162559](https://doi.org/10.3390/ma12162559). url: <https://doi.org/10.3390/ma12162559>.
- [99] D. Montalvão, A. Ribeiro, and J. Duarte-Silva. "A method for the localization of damage in a CFRP plate using damping". In: *Mechanical Systems and Signal Processing* 23.6 (Aug. 2009), pp. 1846–1854. doi: [10.1016/j.ymssp.2008.08.011](https://doi.org/10.1016/j.ymssp.2008.08.011). url: <https://doi.org/10.1016/j.ymssp.2008.08.011>.
- [100] B. F. Sørensen, J. W. Holmes, P. Brøndsted, and K. Branner. "Blade materials, testing methods and structural design". In: *Wind Power Generation and Wind Turbine Design*. WIT Press, June 2010, pp. 417–465. doi: [10.2495/978-1-84564-205-1/13](https://doi.org/10.2495/978-1-84564-205-1/13). url: <https://doi.org/10.2495/978-1-84564-205-1/13>.
- [101] L. Mishnaevsky, K. Branner, H. Petersen, J. Beauson, M. McGugan, and B. Sørensen. "Materials for Wind Turbine Blades: An Overview". In: *Materials* 10.11 (Nov. 2017), p. 1285. doi: [10.3390/ma10111285](https://doi.org/10.3390/ma10111285). url: <https://doi.org/10.3390/ma10111285>.

- [102] A. Treviso, B. V. Genechten, D. Mundo, and M. Tournour. "Damping in composite materials: Properties and models". In: *Composites Part B: Engineering* 78 (Sept. 2015), pp. 144–152. doi: [10.1016/j.compositesb.2015.03.081](https://doi.org/10.1016/j.compositesb.2015.03.081). url: <https://doi.org/10.1016/j.compositesb.2015.03.081>.
- [103] R. F. Gibson. "Damping characteristics of composite materials and structures". In: *Journal of Materials Engineering and Performance* 1.1 (Feb. 1992), pp. 11–20. doi: [10.1007/bf02650027](https://doi.org/10.1007/bf02650027). url: <https://doi.org/10.1007/bf02650027>.
- [104] R. Lakes. *Viscoelastic Materials*. Cambridge University Press., 2009. doi: [10.1017/CBO9780511626722](https://doi.org/10.1017/CBO9780511626722).
- [105] D. J. McTavish and P. C. Hughes. "Modeling of Linear Viscoelastic Space Structures". In: *Journal of Vibration and Acoustics* 115.1 (1993), pp. 103–110. doi: [10.1115/1.2930302](https://doi.org/10.1115/1.2930302). url: <https://doi.org/10.1115/1.2930302>.
- [106] E. J. Barbero. *Finite Element Analysis of Composite Materials Using Ansys*. CRC Press, Dec. 2013. doi: [10.1201/b16295](https://doi.org/10.1201/b16295). url: <https://doi.org/10.1201/b16295>.
- [107] F. Sayer, A. Antoniou, and A. van Wingerde. "Investigation of structural bond lines in wind turbine blades by sub-component tests". In: *International Journal of Adhesion and Adhesives* 37 (Sept. 2012), pp. 129–135. doi: [10.1016/j.ijadhadh.2012.01.021](https://doi.org/10.1016/j.ijadhadh.2012.01.021). url: <https://doi.org/10.1016/j.ijadhadh.2012.01.021>.
- [108] D. J. Ewins. *Modal Testing: Theory, Practice and Application, 2nd Edition*. WILEY, 2009. isbn: ISBN: 978-0-863-80218-8.
- [109] R. Brincker and C. Ventura. *Modal Testing: Theory, Practice and Application, 2nd Edition*. WILEY, 2015. isbn: ISBN: 978-1-119-96315-8.
- [110] J. Woodhouse. "LINEAR DAMPING MODELS FOR STRUCTURAL VIBRATION". In: *Journal of Sound and Vibration* 215.3 (1998), pp. 547–569. doi: [10.1006/jsvi.1998.1709](https://doi.org/10.1006/jsvi.1998.1709). url: <https://doi.org/10.1006/jsvi.1998.1709>.
- [111] S. Adhikari. *Structural Dynamic Analysis with Generalized Damping Models*. John Wiley and Sons, Inc., Nov. 2013. doi: [10.1002/9781118572023](https://doi.org/10.1002/9781118572023). url: <https://doi.org/10.1002/9781118572023>.
- [112] M. Saeedifar and D. Zarouchas. "Damage characterization of laminated composites using acoustic emission: A review". In: *Composites Part B: Engineering* 195 (Aug. 2020), p. 108039. doi: [10.1016/j.compositesb.2020.108039](https://doi.org/10.1016/j.compositesb.2020.108039). url: <https://doi.org/10.1016/j.compositesb.2020.108039>.
- [113] G. A. Beattie. "Acoustic Emission Non-Destructive Testing of Structures using Source Location Techniques." In: *SANDIA Report SAND2013-7779* (2015).

- [114] U. C. Grosse and F. Ohtsu. *Acoustic Emission Testing*. Springer-Verlag Berlin Heidelberg, 2008. isbn: ISBN 978-3-540-69895-1.
- [115] F. Kishinoue. "An experiment on the progression of fracture (A preliminary report). Jisin 6:24-31(1934) translated and published by Ono K". In: *Journal of Acoustic Emission*. 9.3 (1990), pp. 177–180.
- [116] T. F. Drouillard. "Acoustic emission: The first half century." In: *Conference: 12. international acoustic emission symposium, Sapporo (Japan), 21 Oct 1994* RFP-4875; CONF-9410182-1 ON: DE94017176 (1994).
- [117] C. Scruby and H. Wadley. "An assessment of acoustic emission for nuclear pressure vessel monitoring". In: *Progress in Nuclear Energy* 11.3 (Jan. 1983), pp. 275–297. doi: [10.1016/0149-1970\(83\)90014-8](https://doi.org/10.1016/0149-1970(83)90014-8). url: [https://doi.org/10.1016/0149-1970\(83\)90014-8](https://doi.org/10.1016/0149-1970(83)90014-8).
- [118] P. Bently. "A review of acoustic emission for pressurised water reactor applications". In: *NDT International* 14.6 (Dec. 1981), pp. 329–335. doi: [10.1016/0308-9126\(81\)90112-7](https://doi.org/10.1016/0308-9126(81)90112-7). url: [https://doi.org/10.1016/0308-9126\(81\)90112-7](https://doi.org/10.1016/0308-9126(81)90112-7).
- [119] H. Y. Chou, A. P. Mouritz, M. K. Bannister, and A. R. Bunsell. "Acoustic emission analysis of composite pressure vessels under constant and cyclic pressure." In: *Composites Part A: Applied Science and Manufacturing* 70 (2015), pp. 111–120. url: <https://doi.org/10.1016/j.compositesa.2014.11.027>.
- [120] F. Lissek, A. Haeger, V. Knoblauch, S. Hloch, F. Pude, and M. Kaufeld. "Acoustic emission for interlaminar toughness testing of CFRP: Evaluation of the crack growth due to burst analysis." In: *Composites Part B: Engineering* 136 (2018), pp. 55–62. url: <https://doi.org/10.1016/j.compositesb.2017.10.012>.
- [121] M. Nikbakht, Yousefi, J., H. Hosseini-Toudeshky, and G. Minak. "Delamination evaluation of composite laminates with different interface fiber orientations using acoustic emission features and micro visualization." In: *Composites Part B: Engineering* 113 (2017), pp. 185–196. url: <https://doi.org/10.1016/j.compositesb.2016.11.047>.
- [122] C. Barile. "Innovative mechanical characterization of CFRP by using acoustic emission technique." In: *Engineering Fracture Mechanics* 210 (2019), pp. 414–421. url: <https://doi.org/10.1016/j.engfracmech.2018.02.024>.
- [123] E. H. Saidane, D. Scida, M.-J. Pac, and R. Ayda. "Mode-I interlaminar fracture toughness of flax, glass and hybrid flax-glass fibre woven composites: Failure mechanism evaluation using acoustic emission analysis." In: *Polymer Testing* 75 (2019), pp. 246–253. url: <https://doi.org/10.1016/j.polymertesting.2019.02.022>.

- [124] E. I. Tabrizi, A. Kefal, S. J. Monfared Zanjani, C. Cagdas Akalin, and M. Yildiz. "Experimental and numerical investigation on fracture behavior of glass/carbon fiber hybrid composites using acoustic emission method and refined zigzag theory." In: *Composite Structures* 223 (2019). url: <https://doi.org/10.1016/j.compstruct.2019.110971..>
- [125] Q. H. Ali, E. I. Tabrizi, M. R. Awais Khan, A. Tufani, and M. Yildiz. "Microscopic analysis of failure in woven carbon fabric laminates coupled with digital image correlation and acoustic emission, Composite Structures." In: *Composite Structures* 230 (2019). url: <https://doi.org/10.1016/j.compstruct.2019.111515..>
- [126] B. M. Ameer, A. El Mahi, J.-C. Rebiere, I. Gimenez, M. Beyaoui, M. Abdennadher, and M. Haddar. "Investigation and identification of damage mechanisms of unidirectional carbon/flax hybrid composites using acoustic emission." In: *Engineering Fracture Mechanics* 216 (2019). url: <https://doi.org/10.1016/j.engfracmech.2019.106511..>
- [127] M. Haggui, A. El Mahi, Z. Jendli, A. Akrou, and M. Haddar. "Static and fatigue characterization of flax fiber reinforced thermoplastic composites by acoustic emission." In: *Applied Acoustics* 147 (2019), pp. 100–110. url: <https://doi.org/10.1016/j.apacoust.2018.03.011..>
- [128] R. Khademi, S. Abdi, A. Ghorbani, A. Ghiami, and S. Erden. "Damage characterization of carbon/epoxy composites using acoustic emission signals wavelet analysis." In: *Composite Interfaces* 27.1 (2020), pp. 111–124. url: <https://doi.org/10.1080/09276440.2019.1601939>.
- [129] M. Saeedifar, N. M. Saleh, S. Teixeira De Freitas, and D. Zarouchas. "Damage characterization of adhesively-bonded Bi-material joints using acoustic emission." In: *Composites Part B: Engineering* 176 (2019). url: <https://doi.org/10.1016/j.compositesb.2019.107356..>
- [130] M. Saeedifar, J. Mansvelder, R. Mohammadi, and D. Zarouchas. "Using passive and active acoustic methods for impact damage assessment of composite structures." In: *composite structures* 226 (2019). url: <https://doi.org/10.1016/j.compstruct.2019.111252..>
- [131] J. A. Pascoe, D. Zarouchas, R. C. Alderliesten, and R. Benedictus. "Using acoustic emission to understand fatigue crack growth within a single load cycle." In: *Engineering Fracture Mechanics* 194 (2018), pp. 281–300. url: <https://doi.org/10.1016/j.engfracmech.2018.03.012..>
- [132] W. Roundi, A. El Mahi, A. El Gharad, and J.-L. Rebiere. "Acoustic emission monitoring of damage progression in Glass/Epoxy composites during static and fatigue tensile tests." In: *Applied Acoustics* 132 (2018), pp. 124–134. url: <https://doi.org/10.1016/j.apacoust.2017.11.017..>

- [133] M. Saeedifar, M. Ahmadi Najafabadai, D. Zarouchas, H. Hosseini Toudeshky, and M. Jalalvand. "Clustering of interlaminar and intralaminar damages in laminated composites under indentation loading using Acoustic Emission." In: *Composites Part B: Engineering* 144 (2018), pp. 206–219. url: <https://doi.org/10.1016/j.compositesb.2018.02.028..>
- [134] M. Saeedifar, A. Najafabadai, D. M. Zarouchas, H. Hosseini Toudeshky, and M. Jalalvand. "Barely visible impact damage assessment in laminated composites using acoustic emission." In: *Composites Part B: Engineering* 152 (2018), pp. 180–192. url: <https://doi.org/10.1016/j.compositesb.2018.07.016..>
- [135] A. Malpot, F. Touchard, and S. Bergamo. "An investigation of the influence of moisture on fatigue damage mechanisms in a woven glass-fibre-reinforced PA66 composite using acoustic emission and infrared thermography." In: *Composites Part B: Engineering* 130 (2017), pp. 11–20. url: <https://doi.org/10.1016/j.compositesb.2017.07.017..>
- [136] W. Zhou, P. Zhang, and Y. Zhang. "Acoustic Emission Based on Cluster and Sentry Function to Monitor Tensile Progressive Damage of Carbon Fiber Woven Composites." In: *Applied Sciences* 8.11 (2018). url: <https://www.mdpi.com/2076-3417/8/11/2265..>
- [137] J. Tang, S. Soua, C. Mares, and T. Gan. "A Pattern Recognition Approach to Acoustic Emission Data Originating from Fatigue of Wind Turbine Blades." In: *Sensors* 17.11 (2017). url: <https://www.mdpi.com/1424-8220/17/11/2507..>
- [138] B. F. Sørensen, E. Joergensen, C. P. Debel, H. M. Jensen, T. K. Jacobsen, K. Halling, *et al.* "Improved design of large wind turbine blade of fibre composites based on studies of scale effects (Phase 1). Summary report". In: (2004).
- [139] M. Sundaresan, M. Schulz, and A. Ghoshal. "Structural Health Monitoring Static Test of a Wind Turbine Blade: August 1999". In: *Nat Renewable Energy Lab, NREL/SR* 85 (Jan. 2002). doi: [10.2172/15000129](https://doi.org/10.2172/15000129).
- [140] L. Mishnaevsky. "Root Causes and Mechanisms of Failure of Wind Turbine Blades: Overview". In: *Materials* 15.9 (Apr. 2022), p. 2959. issn: 1996-1944. doi: [10.3390/ma15092959](https://doi.org/10.3390/ma15092959). url: <http://dx.doi.org/10.3390/ma15092959>.
- [141] M. A. Shohag, E. Hammel, D. Olawale, and O. Okoli. "Damage mitigation techniques in wind turbine blades: A review". In: *Wind Engineering* 41 (May 2017). doi: [10.1177/0309524X17706862](https://doi.org/10.1177/0309524X17706862).
- [142] C. C. Ciang, J.-R. Lee, and H.-J. Bang. "Structural health monitoring for a wind turbine system: a review of damage detection methods". In: *Measurement Science and Technology* 19.12 (Oct. 2008), p. 122001. issn: 1361-6501. doi: [10.1088/0957-0233/19/12/122001](https://doi.org/10.1088/0957-0233/19/12/122001). url: <http://dx.doi.org/10.1088/0957-0233/19/12/122001>.

- [143] S. Khoshmanesh, S. Watson, and D. Zarouchas. "The effect of the fatigue damage accumulation process on the damping and stiffness properties of adhesively bonded composite structures." In: *Composite Structures* (2022).
- [144] G. Romhany, T. Czigany, and J. Karger-Kocsis. "Failure Assessment and Evaluation of Damage Development and Crack Growth in Polymer Composites Via Localization of Acoustic Emission Events: A Review." In: *Polymer Reviews* 57.3 (2017), pp. 397–439. url: <https://doi.org/10.1080/15583724.2017.1309663..>
- [145] S. Khoshmanesh, S. Watson, and D. Zarouchas. "The effect of the fatigue damage accumulation process on the damping and stiffness properties of adhesively bonded composite structures". In: *Composite Structures* 287 (May 2022), p. 115328. doi: [10.1016/j.compstruct.2022.115328](https://doi.org/10.1016/j.compstruct.2022.115328). url: <https://doi.org/10.1016/j.compstruct.2022.115328>.
- [146] C. Meola and G. M. Carlomagno. "Recent advances in the use of infrared thermography". In: *Measurement Science and Technology* 15.9 (July 2004), R27–R58. doi: [10.1088/0957-0233/15/9/r01](https://doi.org/10.1088/0957-0233/15/9/r01). url: <https://doi.org/10.1088/0957-0233/15/9/r01>.
- [147] A. Rogalski. "Infrared detectors: status and trends". In: *Progress in Quantum Electronics* 27.2-3 (Jan. 2003), pp. 59–210. doi: [10.1016/s0079-6727\(02\)00024-1](https://doi.org/10.1016/s0079-6727(02)00024-1). url: [https://doi.org/10.1016/s0079-6727\(02\)00024-1](https://doi.org/10.1016/s0079-6727(02)00024-1).
- [148] C. Corsi. "Infrared: A Key Technology for Security Systems". In: *Advances in Optical Technologies* 2012 (Dec. 2012), pp. 1–15. doi: [10.1155/2012/838752](https://doi.org/10.1155/2012/838752). url: <https://doi.org/10.1155/2012/838752>.
- [149] G. C. Righini, A. Tajani, and A. Cutolo. *An Introduction to Optoelectronic Sensors*. WORLD SCIENTIFIC, Jan. 2009. doi: [10.1142/6987](https://doi.org/10.1142/6987). url: <https://doi.org/10.1142/6987>.
- [150] C. V. Hoof and P. D. Moor. "PolySiGe uncooled microbolometers for thermal IR detection". In: *Handbook of Infra-red Detection Technologies*. Elsevier, 2002, pp. 449–479. doi: [10.1016/b978-185617388-9/50012-5](https://doi.org/10.1016/b978-185617388-9/50012-5). url: <https://doi.org/10.1016/b978-185617388-9/50012-5>.
- [151] *Thermo-Fluidic Measurement Techniques*. Elsevier, 2016. doi: [10.1016/c2015-0-01881-0](https://doi.org/10.1016/c2015-0-01881-0). url: <https://doi.org/10.1016/c2015-0-01881-0>.
- [152] F. Khodayar, S. Sojasi, and X. Maldague. "Infrared thermography and NDT: 2050 horizon". In: *Quantitative InfraRed Thermography Journal* 13.2 (July 2016), pp. 210–231. doi: [10.1080/17686733.2016.1200265](https://doi.org/10.1080/17686733.2016.1200265). url: <https://doi.org/10.1080/17686733.2016.1200265>.

- [153] W. Lawson, S. Nielsen, E. Putley, and A. Young. "Preparation and properties of HgTe and mixed crystals of HgTe-CdTe". In: *Journal of Physics and Chemistry of Solids* 9.3-4 (Mar. 1959), pp. 325–329. doi: [10.1016/0022-3697\(59\)90110-6](https://doi.org/10.1016/0022-3697(59)90110-6). url: [https://doi.org/10.1016/0022-3697\(59\)90110-6](https://doi.org/10.1016/0022-3697(59)90110-6).
- [154] C. Downs and T. Vandervelde. "Progress in Infrared Photodetectors Since 2000". In: *Sensors* 13.4 (Apr. 2013), pp. 5054–5098. doi: [10.3390/s130405054](https://doi.org/10.3390/s130405054). url: <https://doi.org/10.3390/s130405054>.
- [155] A. Karim and J. Y. Andersson. "Infrared detectors: Advances, challenges and new technologies". In: *IOP Conference Series: Materials Science and Engineering* 51 (Dec. 2013), p. 012001. doi: [10.1088/1757-899x/51/1/012001](https://doi.org/10.1088/1757-899x/51/1/012001). url: <https://doi.org/10.1088/1757-899x/51/1/012001>.
- [156] C. Corsi. "Infrared: A Key Technology for Security Systems". In: *Lecture Notes in Electrical Engineering*. Springer New York, June 2013, pp. 37–42. doi: [10.1007/978-1-4614-3860-1_6](https://doi.org/10.1007/978-1-4614-3860-1_6). url: https://doi.org/10.1007/978-1-4614-3860-1_6.
- [157] V. P. "La mesure du coefficient d'arrachement thermique des isolants par la méthode du touchau (Measurement of the thermal pull-off coefficient of insulating materials using the touchau method)". In: *Chaleur et industrie* 208 (1937), pp. 331–337.
- [158] E. Hendler, R. Crosbie, and J. D. Hardy. "Measurement of heating the skin during exposure to infrared radiation". In: *Journal of Applied Physiology* 12.2 (Mar. 1958), pp. 177–185. doi: [10.1152/jappl.1958.12.2.177](https://doi.org/10.1152/jappl.1958.12.2.177). url: <https://doi.org/10.1152/jappl.1958.12.2.177>.
- [159] R. D. Cowan. "Proposed Method of Measuring Thermal Diffusivity at High Temperatures". In: *Journal of Applied Physics* 32.7 (July 1961), pp. 1363–1370. doi: [10.1063/1.1736235](https://doi.org/10.1063/1.1736235). url: <https://doi.org/10.1063/1.1736235>.
- [160] R. L. Rudkin, R. J. Jenkins, and W. J. Parker. "Thermal Diffusivity Measurements on Metals at High Temperatures". In: *Review of Scientific Instruments* 33.1 (Jan. 1962), pp. 21–24. doi: [10.1063/1.1717653](https://doi.org/10.1063/1.1717653). url: <https://doi.org/10.1063/1.1717653>.
- [161] V. P. Vavilov and D. D. Burleigh. "Review of pulsed thermal NDT: Physical principles, theory and data processing". In: *NDT and E International* 73 (July 2015), pp. 28–52. doi: [10.1016/j.ndteint.2015.03.003](https://doi.org/10.1016/j.ndteint.2015.03.003). url: <https://doi.org/10.1016/j.ndteint.2015.03.003>.
- [162] M. Clark, D. McCann, and M. Forde. "Application of infrared thermography to the non-destructive testing of concrete and masonry bridges". In: *NDT and E International* 36.4 (June 2003), pp. 265–275. doi: [10.1016/s0963-8695\(02\)00060-9](https://doi.org/10.1016/s0963-8695(02)00060-9). url: [https://doi.org/10.1016/s0963-8695\(02\)00060-9](https://doi.org/10.1016/s0963-8695(02)00060-9).

- [163] C. Maierhofer, A. Brink, M. R. ollig, and H. Wiggenger. "Transient thermography for structural investigation of concrete and composites in the near surface region". In: *Infrared Physics and Technology* 43.3-5 (June 2002), pp. 271-278. doi: [10.1016/s1350-4495\(02\)00151-2](https://doi.org/10.1016/s1350-4495(02)00151-2). url: [https://doi.org/10.1016/s1350-4495\(02\)00151-2](https://doi.org/10.1016/s1350-4495(02)00151-2).
- [164] C. Maierhofer, R. Arndt, and M. R. ollig. "Influence of concrete properties on the detection of voids with impulse-thermography". In: *Infrared Physics and Technology* 49.3 (Jan. 2007), pp. 213-217. doi: [10.1016/j.infrared.2006.06.007](https://doi.org/10.1016/j.infrared.2006.06.007). url: <https://doi.org/10.1016/j.infrared.2006.06.007>.
- [165] J. M. Milne and W. N. Reynolds. "The Non-Destructive Evaluation Of Composites And Other Materials By Thermal Pulse Video Thermography". In: *SPIE Proceedings*. Ed. by A. G. Kantsios. SPIE, Mar. 1985. doi: [10.1117/12.946141](https://doi.org/10.1117/12.946141). url: <https://doi.org/10.1117/12.946141>.
- [166] W. Bai and B. S. Wong. "Nondestructive evaluation of aircraft structure using lock-in thermography". In: *Nondestructive Evaluation of Aging Aircraft, Airports, and Aerospace Hardware IV*. Ed. by A. K. Mal. SPIE, May 2000. doi: [10.1117/12.385033](https://doi.org/10.1117/12.385033). url: <https://doi.org/10.1117/12.385033>.
- [167] W. Bai and B. S. Wong. "Evaluation of defects in composite plates under convective environments using lock-in thermography". In: *Measurement Science and Technology* 12.2 (Jan. 2001), pp. 142-150. doi: [10.1088/0957-0233/12/2/303](https://doi.org/10.1088/0957-0233/12/2/303). url: <https://doi.org/10.1088/0957-0233/12/2/303>.
- [168] C. Ibarra-Castanedo, D. Gonzalez, M. Klein, M. Pilla, S. Vallerand, and X. Maldague. "Infrared image processing and data analysis". In: *Infrared Physics and Technology* 46.1-2 (Dec. 2004), pp. 75-83. doi: [10.1016/j.infrared.2004.03.011](https://doi.org/10.1016/j.infrared.2004.03.011). url: <https://doi.org/10.1016/j.infrared.2004.03.011>.
- [169] N. Avdelidis, D. Almond, A. Dobbinson, B. Hawtin, C. Ibarra-Castanedo, and X. Maldague. "Aircraft composites assessment by means of transient thermal NDT". In: *Progress in Aerospace Sciences* 40.3 (Apr. 2004), pp. 143-162. doi: [10.1016/j.paerosci.2004.03.001](https://doi.org/10.1016/j.paerosci.2004.03.001). url: <https://doi.org/10.1016/j.paerosci.2004.03.001>.
- [170] C. Meola, G. M. Carlomagno, and G. Giorleo. "Using infrared thermography to analyze substrate and adhesive effects in bonded structures". In: *Journal of Adhesion Science and Technology* 18.6 (Jan. 2004), pp. 617-634. doi: [10.1163/156856104839301](https://doi.org/10.1163/156856104839301). url: <https://doi.org/10.1163/156856104839301>.
- [171] C. Ibarra-Castanedo, M. Genest, P. Servais, X. P. V. Maldague, and A. Bendada. "Qualitative and quantitative assessment of aerospace structures by pulsed thermography". In: *Nondestructive Testing and Evaluation* 22.2-

- 3 (June 2007), pp. 199–215. doi: [10.1080/10589750701448548](https://doi.org/10.1080/10589750701448548). url: <https://doi.org/10.1080/10589750701448548>.
- [172] R. Montanini. “Quantitative determination of subsurface defects in a reference specimen made of Plexiglas by means of lock-in and pulse phase infrared thermography”. In: *Infrared Physics and Technology* 53.5 (Sept. 2010), pp. 363–371. doi: [10.1016/j.infrared.2010.07.002](https://doi.org/10.1016/j.infrared.2010.07.002). url: <https://doi.org/10.1016/j.infrared.2010.07.002>.
- [173] B. Lahiri, S. Bagavathiappan, P. Reshmi, J. Philip, T. Jayakumar, and B. Raj. “Quantification of defects in composites and rubber materials using active thermography”. In: *Infrared Physics and Technology* 55.2-3 (Mar. 2012), pp. 191–199. doi: [10.1016/j.infrared.2012.01.001](https://doi.org/10.1016/j.infrared.2012.01.001). url: <https://doi.org/10.1016/j.infrared.2012.01.001>.
- [174] W. Harizi, S. Chaki, G. Bourse, and M. Ourak. “Mechanical damage assessment of Glass Fiber-Reinforced Polymer composites using passive infrared thermography”. In: *Composites Part B: Engineering* 59 (Mar. 2014), pp. 74–79. doi: [10.1016/j.compositesb.2013.11.021](https://doi.org/10.1016/j.compositesb.2013.11.021). url: <https://doi.org/10.1016/j.compositesb.2013.11.021>.
- [175] K. Zheng, Y.-S. Chang, and Y. Yao. “Defect detection in CFRP structures using pulsed thermographic data enhanced by penalized least squares methods”. In: *Composites Part B: Engineering* 79 (Sept. 2015), pp. 351–358. doi: [10.1016/j.compositesb.2015.04.049](https://doi.org/10.1016/j.compositesb.2015.04.049). url: <https://doi.org/10.1016/j.compositesb.2015.04.049>.
- [176] A. Chrysafi, N. Athanasopoulos, and N. Siakavellas. “Damage detection on composite materials with active thermography and digital image processing”. In: *International Journal of Thermal Sciences* 116 (June 2017), pp. 242–253. doi: [10.1016/j.ijthermalsci.2017.02.017](https://doi.org/10.1016/j.ijthermalsci.2017.02.017). url: <https://doi.org/10.1016/j.ijthermalsci.2017.02.017>.
- [177] J. N. Zalameda, W. C. Jackson, and C. A. Rose. “Estimation of delamination crack depth using passive thermography”. In: *Thermosense: Thermal Infrared Applications XLI*. Ed. by J. de Vries and B. Oswald-Tranta. SPIE, May 2019. doi: [10.1117/12.2520390](https://doi.org/10.1117/12.2520390). url: <https://doi.org/10.1117/12.2520390>.
- [178] J. N. Zalameda and W. P. Winfree. “Passive Thermography Measurement of Damage Depth During Composites Load Testing”. In: *Frontiers in Mechanical Engineering* 7 (Apr. 2021). doi: [10.3389/fmech.2021.651149](https://doi.org/10.3389/fmech.2021.651149). url: <https://doi.org/10.3389/fmech.2021.651149>.
- [179] A. Audenino. “Correlation between thermography and internal damping in metals”. In: *International Journal of Fatigue* 25.4 (Apr. 2003), pp. 343–351. doi: [10.1016/s0142-1123\(02\)00137-8](https://doi.org/10.1016/s0142-1123(02)00137-8). url: [https://doi.org/10.1016/s0142-1123\(02\)00137-8](https://doi.org/10.1016/s0142-1123(02)00137-8).

- [180] F. CURA, A. E. GALLINATTI, and R. SESANA. "Dissipative aspects in thermographic methods". In: *Fatigue and Fracture of Engineering Materials and Structures* 35.12 (June 2012), pp. 1133–1147. doi: [10.1111/j.1460-2695.2012.01701.x](https://doi.org/10.1111/j.1460-2695.2012.01701.x). url: <https://doi.org/10.1111/j.1460-2695.2012.01701.x>.
- [181] R. Lakes. *Viscoelastic Materials*. Cambridge University Press, 2009. doi: [10.1017/cbo9780511626722](https://doi.org/10.1017/cbo9780511626722). url: <https://doi.org/10.1017/cbo9780511626722>.
- [182] F. P. Incropera and D. P. DeWitt. *Fundamentals of Heat and Mass Transfer*. 4th Edition. New York City, New York: John Wiley and Sons, Inc., 1996.
- [183] S.-K. Au, J. M. Brownjohn, and J. E. Mottershead. "Quantifying and managing uncertainty in operational modal analysis". In: *Mechanical Systems and Signal Processing* 102 (Mar. 2018), pp. 139–157. doi: [10.1016/j.ymssp.2017.09.017](https://doi.org/10.1016/j.ymssp.2017.09.017). url: <https://doi.org/10.1016/j.ymssp.2017.09.017>.
- [184] V. H. Vu and M. Thomas. "Uncertainties on modal parameters by operational modal analysis". In: *Mechanics and Industry* 15.2 (2014), pp. 153–158. doi: [10.1051/meca/2014018](https://doi.org/10.1051/meca/2014018). url: <https://doi.org/10.1051/meca/2014018>.
- [185] E. Reynders, K. Maes, G. Lombaert, and G. D. Roeck. "Uncertainty quantification in operational modal analysis with stochastic subspace identification: Validation and applications". In: *Mechanical Systems and Signal Processing* 66-67 (Jan. 2016), pp. 13–30. doi: [10.1016/j.ymssp.2015.04.018](https://doi.org/10.1016/j.ymssp.2015.04.018). url: <https://doi.org/10.1016/j.ymssp.2015.04.018>.
- [186] R. Pintelon, P. Guillaume, and J. Schoukens. "Uncertainty calculation in (operational) modal analysis". In: *Mechanical Systems and Signal Processing* 21.6 (Aug. 2007), pp. 2359–2373. doi: [10.1016/j.ymssp.2006.11.007](https://doi.org/10.1016/j.ymssp.2006.11.007). url: <https://doi.org/10.1016/j.ymssp.2006.11.007>.
- [187] Y.-C. Zhu and S.-K. Au. "Bayesian data driven model for uncertain modal properties identified from operational modal analysis". In: *Mechanical Systems and Signal Processing* 136 (Feb. 2020), p. 106511. doi: [10.1016/j.ymssp.2019.106511](https://doi.org/10.1016/j.ymssp.2019.106511). url: <https://doi.org/10.1016/j.ymssp.2019.106511>.
- [188] F. B. Zahid, Z. C. Ong, and S. Y. Khoo. "A review of operational modal analysis techniques for in-service modal identification". In: *Journal of the Brazilian Society of Mechanical Sciences and Engineering* 42.8 (July 2020). doi: [10.1007/s40430-020-02470-8](https://doi.org/10.1007/s40430-020-02470-8). url: <https://doi.org/10.1007/s40430-020-02470-8>.

CURRICULUM VITÆ

Seyedsharif KHOSHMANESH

11-07-1976 Born in Khormoj, Iran

EDUCATION

1992-1994 High school diploma, Mathematics and physics

1996-2000 Bachelor of science,
Mechanical engineering, Shiraz University, Shiraz, Iran.

2000-2002 Master of Science, mechanical engineering,
Sharif University of technology, Tehran, Iran.

2017-2023 PhD researcher,
Wind energy section, Aerospace faculty,
Delft University of Technology, Delft, Netherlands.

LIST OF PUBLICATIONS

Journal papers

- S.Khoshmanesh, S.J.Watson, D.Zarouchas, The effect of the fatigue damage accumulation process on the damping and stiffness properties of adhesively bonded composite structures, *Composite Structures*, 2022, 287, <https://doi.org/10.1016/j.compstruct.2022.115328>
- S. Khoshmanesh, S.J. Watson, D. Zarouchas, New indicator for damage localization in a thick adhesive joint of a composite material used in a wind turbine blade, *Engineering Structures*, Volume 283, 2023, <https://doi.org/10.1016/j.engstruct.2023.115870>.
- S. Khoshmanesh, S.J. Watson, D. Zarouchas, Early detection of impact fatigue damage in an adhesively-bonded connection using acoustic emission, submitted to *Engineering Structures*, ENGSTRUCT-D-23-06220R2, Oct 2023.

Reviewed conference papers

- S.Khoshmanesh, S.J.Watson, D.Zarouchas, Characterisation of fatigue damage in a thick adhesive joint based on changes in material damping, 2020, *Journal of Physics: Conference Series*, Volume 1618, Control and Monitoring.